UNIVERSIDAD NACIONAL DEL LITORAL
Facultad de Ingeniería y Ciencias Hídricas
Instituto de Desarrollo Tecnológico para la Industria Química

COMPUTER SIMULATION OF STEEL THERMOMECHANICAL PROCESSES AT HIGH TEMPERATURES

Ing. Andrés Amilcar Anca.

Tesis remitida al Comité Académico del Doctorado
como parte de los requisitos para la obtención
del grado de
DOCTOR EN INGENIERIA
Mención Mecánica Computacional
de la
UNIVERSIDAD NACIONAL DEL LITORAL

2008

Comisión de Posgrado, Facultad de Ingeniería y Ciencias Hídricas, Ciudad Universitaria, Paraje El Pozo, S3000, Santa Fe, Argentina.

Abstract

This thesis deals with the simulation of fusion welding and other metallurgical processes sach as heat treatment by the Finite Elements Method. The models were implemented in OOFELIE [Ope04, CKG94], which includes moving heat sources, steel metallurgy, temperature dependence of thermo-physical properties, elasto-plasticity, non-steady state heat transfer, and mechanical analysis. It is assumed that the thermal problem is not coupled with the mechanical. The thermal analysis is performed separately and prior to the mechanical analysis. The mechanical problem is based on thermal history. The three-dimensional residual stress state of welded joints are compared with previously published results in the literature.

Resumen

Esta tesis trata sobre la simulación de los procesos de soldadura por fusión y otros procesos metalúrgicos como tratamientos térmicos utilizando el Método de los Elementos Finitos (MEF). Los modelos fueron implementados en OOFELIE [Ope04, CKG94] el que incluye fuentes de calor móviles, aporte de material, metalurgia de aceros, dependencia con la temperatura de las propiedades termo-físicas, elasto-plasticidad de metales, transferencia de calor no estacionaria, y análisis mecánico. Se asume que el problema térmico no está acoplado con el mecánico. El análisis térmico se realiza separadamente y previo al mecánico. El problema mecánico está basado en la historia térmica. El estado tridimensional de tensiones residuales de una unión soldada a tope es comparado contra resultados previamente publicados en la literatura.

Contents

List of Figures

List of Tables

Chapter 1

Introduction

1.1 Objective of this Thesis

The overall objective is to simulate the stress state in metal production processes that involve phase change phenomena and/or microstructural changes, in order to achieve a better understanding of the involved phenomena and optimize various aspects related to them. The particular objectives of this thesis are related to the numerical simulation of the thermomechanical and microstructural response in fusion welding processes. A specific computational code was developed in order to deal with this type of problems. The models implemented in this code may be used for example in simulation of welding, heat treatment and continuous casting of steel. The implemented models describe the physics of the problem on a macroscopic scale. The purpose is to obtain a code that provides results of acceptable accuracy in industrial applications using the finite element method. The correct validation of the code is one of the key task we have pursued in the thesis. Examples of application will be considered, and stresses and microstructure will be obtained for welded plates.

1.2 Motivation

The use of the Finite Element Method (FEM) in product development is now well established, however, its use in manufacturing processes is not very common and is part of the field of new applications in computational mechanics. The most important reason for this development is the industrial needing to improve productivity and quality of products and to have better understanding of the influence of different process parameters.

The modeled phenomena play an important role at various stages of the production of steel parts, for example, welding, heat treatment, casting, among others.

The importance of these applications lies in determining the evolution of stresses and deformations to predict, for example, susceptibility to cracking and thus prevent failures during manufacturing or even service. Furthermore, this simulation tool can be used to optimize some aspects of manufacturing processes.

The following aspects of the welding method can be analyzed, or optimized, by numerical simulation:

- Distortion due to an incorrect choice of the welding sequence.

- Optimization of clamping devices. The choice of how to hold the pieces to join has a marked influence on the residual stress and end-distortion of pieces.
- The minimum period of time that a piece should remain in the holding device, to minimize distortions.
- Welding parameters can be adjusted and tested a priori.
- Estimates of both microstructure and resulting hardness can be obtained to determine the more appropriate post-thermal treatment .
- Simulation programs could be subsequently coupled with production equipment.

1.3 Fusion Welding

Welding techniques are one of the most important and most often used methods for joining pieces in industry. Any information about the shape, size and residual stress of a welded piece is of particular interest to improve quality.

Fusion welding is a process of union, in which two metal parts are heated locally over the melting point, obtaining in this way a located coalescence of both parts. Different types of welds can be distinguished by the type of heat source that is used to achieve the joint of metals. Some examples of external heat sources are electric arc, laser and electron beam. During the welding process it is possible to add a filler material.

The analysis of welding processes involves several branches of Physics, and requires the coupling of different models that addresed to describe the behavior of a phenomenological system. Many of these models have been implemented numerically and are being used in an efficient way to solve the problems on an individual basis.

In the arc welding process, the energy required for the metal fusion is produced by Joule effect. The metal is immersed in a magnetic field and an electric discharge generates plasma between the tip of the welding torch and the working piece. This effect produces the energy required to melt the base and filler metal, forming what is known as the liquid pool. The piece surface temperature varies from 1700 K to 2500 K, depending on the material. In the liquid pool, convective effects take place, what improve the heat transport in the base metal. Finally, after removing the heat sources, the metal solidifies.

During the process, temperature changes in the alloy produce solid state transformations. These microstructural transformations cause changes in the material properties during the evolution of the process. Heating and cooling induce localized volumetric changes. The thermal strains that occur in the vicinity of the welding line are elastoplastic and the resulting stresses react causing permanent distortions.

Distortions introduce residual deformation that complicates the assembly of welded structures and reduces their quality. Also, in certain applications, this distortion may bring useless the structure.

The aforementioned highlights the importance of modeling tools in the design stages to analyze residual stresses and deformations. Another important aspect to consider is the development of suitable methods for improving the dimensional accuracy of parts or welded structures.

Currently, the simulation of welding is used in a wide range of industrial applications, aerospace, nuclear and shipyards among others.

Other important aspect of welding simulation is the identification and characterization of the welding parameters, the temporal evolution of the microstructure, temperature and deformation, which are useful for predicting the behavior during the process as well as during service.

1.4 State of the art

The residual stresses and distortions problem in welding was first mentioned in the work of Slavianov in 1892. He pointed out, particularly, how harmless are the stresses generated during the welding processes. This problem persists at the present, being an important subject for many researchers. The simulation of welding processes has significatively progressed in the last three decades, from analyses carried out in experimental laboratories to computational applications that include models to describe coupled complex phenomena.

Since the beginning of the 70s, the FEM is used to simulate the mechanical problem in welding. Some of the well known references upto the 90s are the works of Marcal [Mar74], Karlsson [Kar86, Kar93], Goldak et al., [GOG$^+$92], Smith [Smi92], and Radaj [Rad88].

Finite element codes addressed to study this problem have been described in the the paper of Dexter [Dex91], Chandra [Cha85], Ravichandran [RRGK97], Karlsson [Kar97], etc.

In recent articles on finite element models, it has been common to assume a number of simplifications that can be described as follows:

- Assume the necessary symmetry in the problem, in order to solve 2D models. Thus, it can be found in the work of Song et al. [SPNM03] on welded joints, Branza et al. [BDF$^+$04] on TIG welding for repairing parts, Cho et al. [CZKK04] in laser welding, Hyde et al. [HBSS06] for TIG butt welding, Hou et al. [HKW$^+$06] for spot welding, and Deng and Murakawa [DM06b] for multiple-pass welding. The motivation (not always recognized) of this simplification is the high computational cost of 3D models. Duranton et al. [DDR$^+$04] and Gery et al. [GLM05] reveal shortcomings in the 2D approach in longitudinal welding when the heat flux in the direction of the weld is ignored.

- Related with the mechanical description of the problem, it has been assumed that materials respond as an inviscid elasto-plastic model in the works of [SPNM03, AS05, HKW$^+$06, Moc06, MCGC06], or with isotropic [BDF$^+$04, DDR$^+$04, FPTB06, HBSS06], [DM06a, DM06b, MDPM06], or as elasto-viscoplastic [NRLD06, HR06]. Alberg and Berglund [AB03] compared plastic and viscoplastic models applied to welding simulation, agreeing to use a simple plastic model in the initial stages of the study. However, it cannot be ignored that at high temperatures, the viscous effects have a notable effect on the behavior of metals [FC03].

  Also, in general, welding involves heating-cooling cycles whose effect on the mechanical behavior of the material is represented only if it is taken into account kinematics hardening. Therefore the justification of using simpler models such as the elastoplastic without hardening or only with isotropic hardening (up to now, the most widely used) is a mere reduction of computational cost.

- As for the study of the microstructural changes during welding, the 2D thermo-mechanical model of Deng and Murakawa [DM06b] is capable of reproducing only austenite → martensite transformation in steel, which is produced at very high rates of cooling, obviating the ferritic, pearlitic and bainitic transformations that are observed in the heat affected zones at lower rates. More sophisticated 2D and 3D thermo-mechanical-metallurgical models were proposed by Alberg and Berglund [AB03] and Ferro et al. [FPTB06] respectively, taking into account all the changes mentioned above. Notably, in all cases, the influence of microstructure is considered in the mechanical properties (yield stress, thermal expansion), but it is not considered the influence on the thermal properties such as conductivity, which varies considerably with the microstructural changes (as shown by[MLA^{+}02]).

Very few models applied to simulate welding take into account the dynamics of the molten material. Che et al. [CCT04] focus on determining the seam shape. Wang et al. [WSLT05] and DebRoy [DD06, HNFD06, RED06] model the convection in the liquid pool and its effect on heat transfer. This effect is usually approximated in thermal analysis by increasing the metal conductivity

The 2D models of Fan Kovacevic [FK04] and Lu et al. [LTYY06] include electromagnetic effects, although it is only restricted to the arc-welding molten metal.

In all the previous models, the unique interaction between mechanical and thermal analyses is the temperature influence on the mechanical properties. Thus, for example, the significant distortion that changes the conduction heat flux between the welded piece and its support, is not accounted for.

Chapter 2

Thermal Model

In this section a temperature-based finite element model to simulate unsteady conduction heat transfer problems in a 3D media undergoing mushy phase change is described. It is an extension of a method previously formulated for solving 2D and axisymmetric transient conduction heat transfer problems [FCH99] and steady state conduction-advection phase-change problems [FCH01].

The analyzed domain is discretized using linear tetrahedral finite elements. Galerkin weighting functions are used.

During phase change, a considerable amount of latent heat is released or absorbed, causing a strong non-linearity in the enthalpy function. In order to model correctly such phenomenon, we distinguish the different one-phase subregions encountered when integrating over those finite elements embedded into the solidification front.

Contributions from different phases are integrated separately in order to capture the sharp variations of the material properties between phases. This, so called, discontinuous integration avoids the regularization of the phenomenon, allowing the exact evaluation of the discrete non-linear governing equation, which is solved using a full Newton-Raphson scheme, together with line-search.

We validate the performance of the thermal model by comparison with an exact solution [OU79].

2.1 Problem definition

Under the assumptions of incompressibility, negligible viscosity and dissipation, linear dependence of the heat flux on temperature gradient (Fourier's law), and no melt flow during the solidification process, the energy balance for each subdomain $\mathit{\Omega}_i$ is governed by the classical energy balance equation

$$\rho \frac{\partial \mathcal{H}}{\partial t} - \nabla \cdot (\kappa \nabla T) = q \quad \forall (\boldsymbol{x}, t) \in \mathit{\Omega}_i \tag{2.1}$$

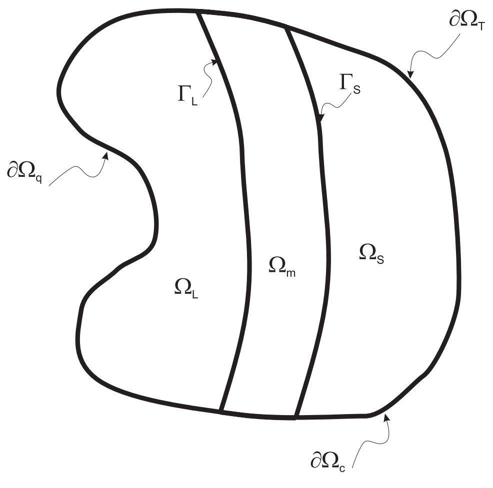

Figure 2.1: Thermal problem definition

where T denotes the temperature, $\mathcal{H}$ the enthalpy (per unit volume), $\kappa = \kappa(T)$ the material thermal conductivity, assumed isotropic and $q = q(\boldsymbol{x}, t)$ is the welding volume heat input (to be defined later in Section (2.6)). Equation (2.1) is supplemented by the following initial condition

$$T = T_0 \quad \forall \boldsymbol{x} \in \Omega_i, \quad t = t_0$$

and the external boundary conditions on $\partial\Omega$:

$$T = \bar{T} \qquad \text{at } \partial\Omega_T \tag{2.2}$$

$$-\kappa \nabla T \cdot \boldsymbol{n} = \bar{q} \qquad \text{at } \partial\Omega_q \tag{2.3}$$

$$-\kappa \nabla T \cdot \boldsymbol{n} = h_{env}(T - T_{env}) \qquad \text{at } \partial\Omega_c \tag{2.4}$$

being $\partial\Omega_T$, $\partial\Omega_q$ and $\partial\Omega_c$ non-overlapping portions of the body boundary $\partial\Omega$, with prescribed temperature, conductive and convective heat flux, respectively. In the above, $\bar{T}$ and $\bar{q}$ refer to imposed temperature and heat flux fields, and T_{env} is the temperature of the environment, whose film coefficient is h_{env}; $\boldsymbol{n}$ denotes the unit outward normal to $\partial\Omega$.

Further, the following continuity conditions must hold at the interface(s) Γ:

$$T = T_\Gamma \tag{2.5}$$

$$\langle \mathcal{H} u(\boldsymbol{\eta}) + \kappa \nabla T \cdot \boldsymbol{\eta} \rangle = 0 \tag{2.6}$$

where T_Γ is a constant value (equal to the melting temperature for isothermal solidification, and either the solidus or liquidus temperature otherwise), $\langle * \rangle$ denotes the jump of the quantity $(*)$ in crossing the interface Γ, which is moving with speed u in the direction given by the unit vector $\boldsymbol{\eta}$. Note that the second equation states the jump energy balance at the interface.

In order to retrieve T as the only primal variable, enthalpy is defined as

$$\mathcal{H}(T) = \int_{T_{ref}}^{T} c\mathrm{d}\tau + \mathcal{L} f_l \tag{2.7}$$

being ρc and $\rho\mathcal{L}$ the unit volume heat capacity and latent heat, respectively, and T_{ref} an arbitrary reference temperature; f_l is a characteristic function of temperature, called volumetric liquid fraction, defined as

$$f_l(T) = \begin{cases} 0 & \text{if } T < T_{sol} \\ 0 \leq f_l^m(T) \leq 1 & \text{if } T_{sol} \leq T \leq T_{liq} \\ 1 & \text{if } T > T_{liq} \end{cases} \tag{2.8}$$

where T_{sol} and T_{liq} denote the solidus and liquidus temperatures, respectively, i.e., the lower and upper bounds of the mushy temperature range.

2.2 Finite element formulation

First, the weak or variational form of the balance equation (2.1) is derived , supplied by the boundary conditions (2.2-2.6), using the weighted residuals method. The proper choice of weighting functions together with the application of Reynolds' transport theorem allows to cancel the terms arising from the interface conditions (2.6). Furthermore, using the definition (2.7), a weak temperature-based form of the governing equation is obtained:

$$\begin{aligned} \int_{\Omega} W \rho c \frac{\partial T}{\partial t}\, \mathrm{d}V + \frac{\partial}{\partial t} \int_{\Omega} W \rho \mathcal{L} f_l \, \mathrm{d}V + \int_{\Omega} \kappa \nabla W \cdot \nabla T \, \mathrm{d}V + \int_{\partial\Omega_q} W \bar{q} \, \mathrm{d}S + \\ + \int_{\partial\Omega_c} W h_{env} (T - T_{env}) \, \mathrm{d}S - \int_{\Omega} W q \, \mathrm{d}V = 0 \end{aligned} \tag{2.9}$$

where W is the weighting function.

In the finite element context, the unknown field T is approximated as a linear combination of interpolation functions $N_i(x, y, z)$, the shape functions, as follows:

$$T(x, y, z) = \sum_{i}^{N} N_i(x, y, z) T_i \tag{2.10}$$

being T_i the temperature at each node i ($i = 1, 2, \cdots, N$) arising from the discretization of the analyzed domain Ω.

We substitute T by its approximation (2.10) into equation (2.9). Then we adopt as weighting function W the interpolation function N ($W \equiv N_i$, Galerkin method). A non linear system of N ordinary differential equations is set, stated in matrix form as

$$\boldsymbol{\Psi} = \boldsymbol{C} \frac{\partial \boldsymbol{T}}{\partial t} + \frac{\partial \boldsymbol{L}}{\partial t} + \boldsymbol{K}\boldsymbol{T} - \boldsymbol{F} = 0 \tag{2.11}$$

where $\boldsymbol{T}$ is the vector of unknown nodal temperatures, $\boldsymbol{C}$ the capacity matrix, $\boldsymbol{L}$ the latent heat vector, $\boldsymbol{K}$ the conductivity (stiffness) matrix and $\boldsymbol{F}$ the force vector.

Each term of the residual vector $\boldsymbol{\Psi}$ is given (in components) by:

$$\begin{aligned} C_{ij} &= \int_{\Omega} \rho c \, N_i N_j \, \mathrm{d}V \\ L_i &= \int_{\Omega} \rho \mathcal{L} f_l N_i \, \mathrm{d}V \\ K_{ij} &= \int_{\Omega} \kappa \nabla N_i \cdot \nabla N_j \, \mathrm{d}V + \int_{\partial\Omega_c} h_{env} \, N_i N_j \, \mathrm{d}S. \end{aligned} \tag{2.12}$$

On the other hand, the load vector $\boldsymbol{F}$ takes the form:

$$F_i = -\int_{\partial\Omega_q} \bar{q} N_i \, \mathrm{d}S + \int_{\partial\Omega_c} h_{env} T_{env} N_i \, \mathrm{d}S - \int_{\partial\Omega} q N_i \, \mathrm{d}V \tag{2.13}$$

2.3 Discontinuous integration in linear tetrahedral elements

Since this work follows the same integration scheme give in [FCH99, FCH01], the discontinuous integration of a linear tetrahedra is now briefly described. In a linear tetrahedral element the interfaces (isotherms) correspond to plane surfaces. Therefore, the different subregions characterized by only one phase show polyhedral geometries. This fact allows us to solve exactly the integrals (2.12) in a relatively easy manner.

The use of linear elements produces an element-wise constant approximation to the temperature gradient, $\nabla N_i T_i$.

The transient conduction problem in the absence of phase change has been widely discussed in the classic finite element literature (see e.g. Zienkiewicz and Taylor [ZT00]). Then ,we shall focus on the latent heat effects, as given in general form by equation (2.12). Let us consider the contribution of a typical linear tetrahedral element e to $\boldsymbol{L}$ that involves phase change:

$$L_i^e = \rho \mathcal{L} \int_{\Omega_l^e} N_i^e \, \mathrm{d}V \; + \rho \mathcal{L} \int_{\Omega_m^e} f_l N_i^e \, \mathrm{d}V. \tag{2.14}$$

The above integrals extend over the element liquid Ω_l^e and mushy Ω_m^e subdomains.

We assume that the latent heat is uniformly released or absorbed during solidification such that f_l is a linear function of T,

$$f_l = \frac{T - T_{sol}}{T_{liq} - T_{sol}}, \tag{2.15}$$

and the elemental latent heat vector takes the form

$$\boldsymbol{L}^e = \boldsymbol{C}_L^e \boldsymbol{T} - \frac{\rho \mathcal{L} T_{sol}}{T_{liq} - T_{sol}} \boldsymbol{N}^e(\boldsymbol{x}_{bar,m}) V_m^e + \rho \mathcal{L} \boldsymbol{N}^e(\boldsymbol{x}_{bar,l}) V_l^e \tag{2.16}$$

where

$$\boldsymbol{C}_L^e = \frac{\rho\mathcal{L}}{T_{liq} - T_{sol}} \int_{\Omega_m^e} \boldsymbol{N}^e \boldsymbol{N}^{e^T} \,\mathrm{d}V \tag{2.17}$$

being V_l^e, V_m^e the volumes of liquid and mushy zones and $\boldsymbol{x}_{bar,l}$, $\boldsymbol{x}_{bar,m}$ the barycenter of the liquid and mushy subregions respectively. We remark that, using tetrahedral finite element, the evaluation of expressions 2.14-2.17 are very simple and straightforward . In fact, computation of the volume V_m^e (and its center) is a trivial task, i.e., for the fully-mushy element and cases *sssm* and *mlll* in Figure 2.2. Also, the cases *smmm*, *mmml*, *sssl*, *slll* and *smml* can be expressed as the difference of tetrahedral volumes. For pentahedral mushy volumes not included in the previous classification, i.e. cases *ssmm* and *mmll*, Ω_m^e is assumed splited into three tetrahedra (see Figure 2.3). Finally, the remainder (hexahedral) mushy configurations (*ssll*, *ssml* and *smll*) are evaluated as differences of tetrahedra and pentahedra.

Remark: It is also posible to accurately approximate any non-linear liquid fraction f_l using a piecewise linear function f_l^*. Let f_l be equal to f_l^* at a series of abscissa $T_0 = T_{sol} < T_1 < \cdots < T_n = T_{liq}$. $\boldsymbol{L}$ can be though as the addition of contributions arising from n partial mushy zones; each one being defined by a temperature range $[T_{i-1}, T_i]$ $(i = 1, 2, \cdots, n)$ within which a portion $\rho\mathcal{L}_i = \rho\mathcal{L}[f_l(T_i) - f_l(T_{i-1})]$ is uniformly released or absorbed.

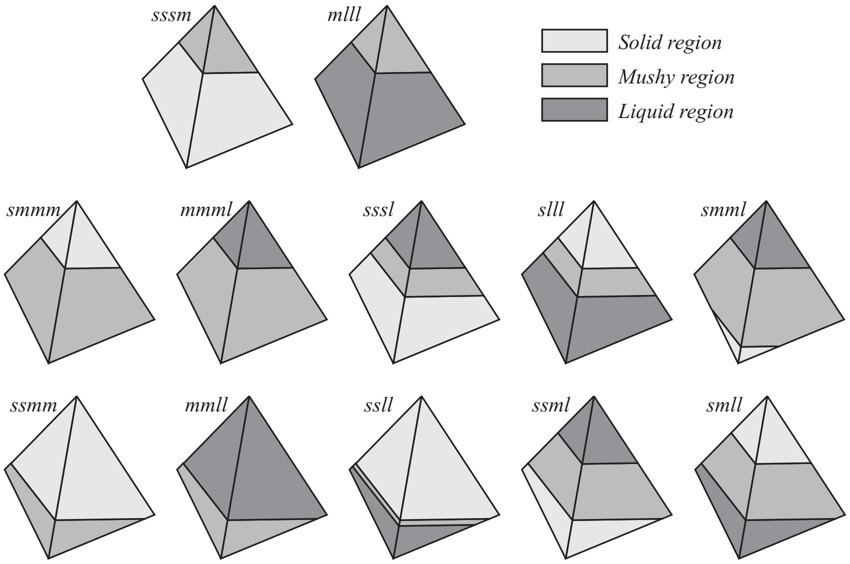

Figure 2.2: Different configurations of linear tetrahedral finite elements affected by mushy phase change.

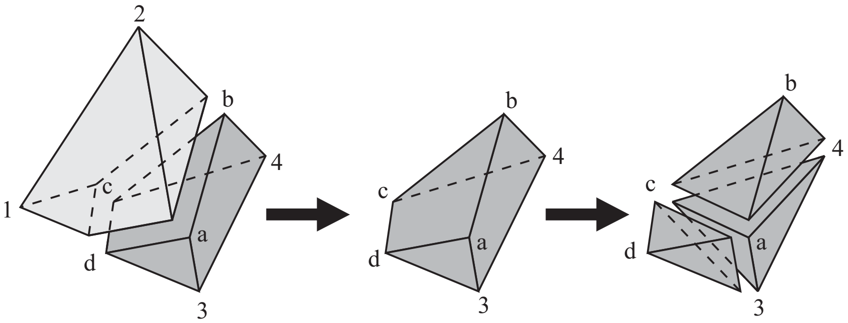

Figure 2.3: Split of a pentahedral mushy region into three tetrahedra.

2.4 Solution scheme

Time integration is done with the unconditionally stable first-order backward Euler method. This implicit scheme is applied on equation (2.11), which leads to a set of non-linear equations to be solved for the values of the temperatures at finite element nodes, at the end of the time increment considered:

$$\boldsymbol{\Psi}_{n+1} = \boldsymbol{C}_{n+1}\frac{\boldsymbol{T}_{n+1}-\boldsymbol{T}_n}{\Delta t} + \frac{\boldsymbol{L}_{n+1}-\boldsymbol{L}_n}{\Delta t} + \boldsymbol{K}_{n+1}\boldsymbol{T}_{n+1} - \boldsymbol{F}_{n+1} = \boldsymbol{0} \tag{2.18}$$

The solution of the highly non-linear discrete balance equation (2.18) is achieved by means of the well-known Newton-Raphson method. Because of its quadratic convergence rate, it provides a fast way to solve non-linear equations [ZT00], whenever the initial solution stays into the convergence or “attraction” zone.

At each new iteration i, $\boldsymbol{\Psi}$ is approximated using a first order Taylor expansion,

$$\boldsymbol{\Psi}_{(\boldsymbol{T}^{(i)})} \approx \boldsymbol{\Psi}_{(\boldsymbol{T}^{(i-1)})} + \boldsymbol{J}_{(\boldsymbol{T}^{(i-1)})}\Delta\boldsymbol{T}^{(i)} = \boldsymbol{0} \tag{2.19}$$

being $\boldsymbol{J} = \mathrm{d}\boldsymbol{\Psi}/\mathrm{d}\boldsymbol{T}$ the Jacobian or tangent matrix of the equation system (2.18), and $\Delta\boldsymbol{T}^{(i)} = \boldsymbol{T}^{(i)} - \boldsymbol{T}^{(i-1)}$ the incremental correction of temperatures. Thus, $\Delta\boldsymbol{T}$ can be evaluated as follows:

$$\Delta\boldsymbol{T}^{(i)} = -[\boldsymbol{J}_{(\boldsymbol{T}^{(i-1)})}]^{-1}\boldsymbol{\Psi}_{(\boldsymbol{T}^{(i-1)})} \tag{2.20}$$

All the terms of the tangent matrix for transient conduction heat transfer problems, may be found in the classical texts, e.g. Zienkiewicz and Taylor [ZT00]. The latent heat contribution $\frac{\mathrm{d}\boldsymbol{L}}{\mathrm{d}\boldsymbol{T}}$ is detailed below. This particular matrix is the assemblage of the element matrices:

$$\begin{aligned}\frac{\mathrm{d}\boldsymbol{L}^e}{\mathrm{d}\boldsymbol{T}^e} = \boldsymbol{C}_L^e + \frac{\mathrm{d}\boldsymbol{C}_L^e}{\mathrm{d}\boldsymbol{T}^e}\boldsymbol{T}^e - \frac{\rho\mathcal{L}T_{sol}}{T_{liq}-T_{sol}}\left[\frac{\mathrm{d}\boldsymbol{N}^e(\boldsymbol{x}_{bar,m})}{\mathrm{d}\boldsymbol{T}^e}V_m^e + \boldsymbol{N}^e(\boldsymbol{x}_{bar,m})\frac{\mathrm{d}V_m^e}{\mathrm{d}\boldsymbol{T}^e}\right] + \\ +\rho\mathcal{L}\left[\frac{\mathrm{d}\boldsymbol{N}^e(\boldsymbol{x}_{bar,l})}{\mathrm{d}\boldsymbol{T}^e}V_l^e + \boldsymbol{N}^e(\boldsymbol{x}_{bar,l})\frac{\mathrm{d}V_l^e}{\mathrm{d}\boldsymbol{T}^e}\right]\end{aligned} \tag{2.21}$$

As aforementioned, the Newton-Raphson scheme is efficient provided that the initial guess $\boldsymbol{T}^{(0)}$ lies within the convergence radius of the solution $\boldsymbol{T}$. Alternatively, the convergence can be improved using a line-search procedure [MS79]. Assuming that $\Delta\boldsymbol{T}$, as defined by equation (2.20), is the correct search direction, then $\boldsymbol{T}$ at the iteration i is predicted as follows

$$\boldsymbol{T}^{(i)} = \boldsymbol{T}^{(i-1)} + \beta\Delta\boldsymbol{T}^{(i)} \tag{2.22}$$

being the scalar parameter β determined under the condition of orthogonality between the new residual vector and the search direction, i.e.,

$$\boldsymbol{\Psi}(\boldsymbol{T}^{(i)}) \cdot \Delta\boldsymbol{T}^{(i)} = 0. \tag{2.23}$$

Line-search must be activated whenever

$$\boldsymbol{\Psi}(\boldsymbol{T}^{(i-1)} + \Delta\boldsymbol{T}^{(i)}) \cdot \Delta\boldsymbol{T}^{(i)} > k\boldsymbol{\Psi}(\boldsymbol{T}^{(i)}) \cdot \Delta\boldsymbol{T}^{(i)}. \tag{2.24}$$

For the application presented below, the factor k was chosen to be unit. Reference [FCH99] contains a detailed description of the currently implemented algorithm.

2.5 Validation - A benchmark problem

Verification of the model has been performed comparing numerical and analytical results for a transient non-linear heat transfer problem with exact solution. This benchmark problem simulates the solidification of a material which is initially at a temperature just above its freezing point and subject to a line heat sink in an infinite medium with cylindrical symmetry. The substance has an extended freezing temperature range between the solidus and liquidus temperatures. This problem was solved exactly by Özisik and Uzzel [OU79]. The solid fraction is assumed to vary linearly with the temperature. Since the material has a high latent heat, severe numerical discontinuities are present at the liquid-solid boundary. The material properties are summarized in table 2.1. Only a circular sector of the cylinder (see Figure 2.4), forming a wedge, was discretized because of the symmetry.

The cylinder surface at $r = L$ is maintained at a constant, uniform temperature T_0. The dimensions of the wedge are: radius = 1 m, sector angle = 15 degrees, and thickness = 0.01 m. The mesh is shown in Figure 2.6.

The numerical results are in agreement with the corresponding analytical results for $t = 3600[s]$ as shown in Figure 2.5.

The use of a concentrated heat sink leads to large thermal gradients as $r \to 0$. This singularity explains the error increment in the vicinity of the axis (see Figure 2.5).

As described in [MGOB87], a concentrated thermal load in an infinite half space has a singularity proportional to the inverse of the radial distance. Therefore concentration of elements and nodes around the (welding) source, where gradients change rapidly, is required. In Figure 2.5 the relative errors between the exact and 3D FEM solution is plotted.

Figure 2.6 offers a general view of the computed temperature distribution through the

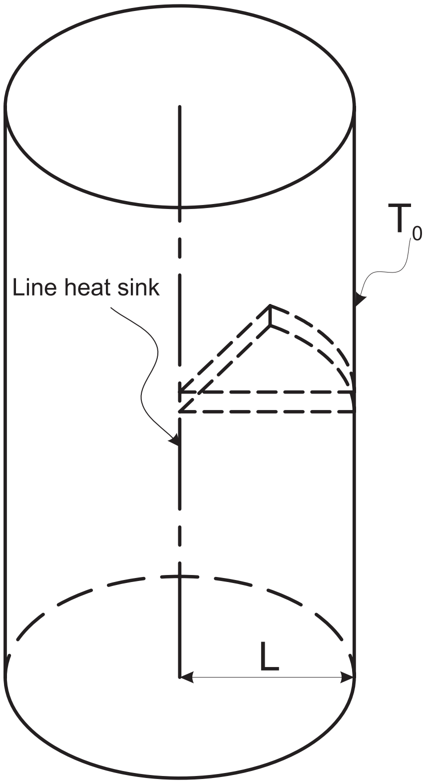

Figure 2.4: Validation problem description

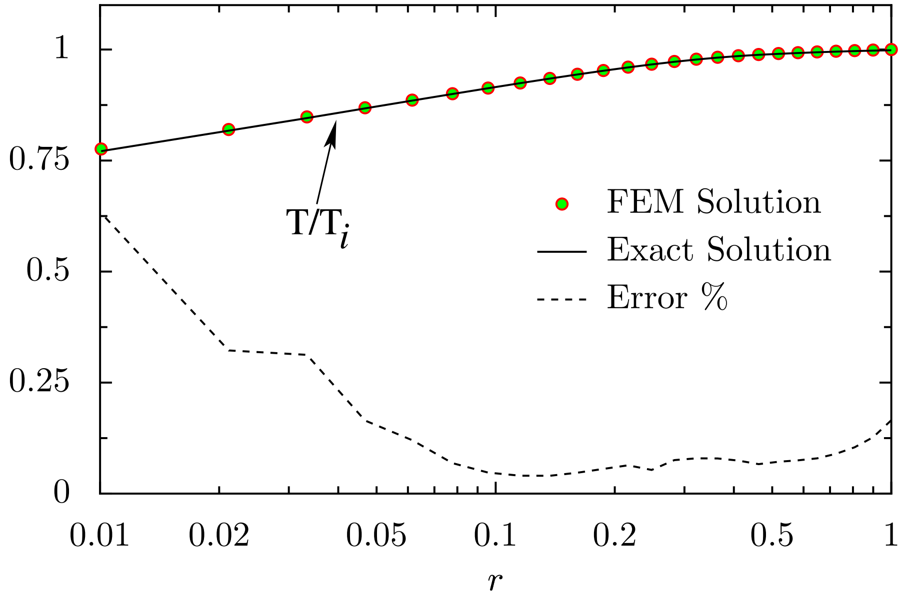

Figure 2.5: Analytical solution, FEM solution, and relative error of a model phase change problem for $t = 3600[s]$

Parameter	Symbol	Value	Unit
Density	ρ	2723.2	$[kg/m^3]$
Specific Heat, (solid)	c_s	1046.7	$[J/kg^oC]$
Specific Heat, (liquid)	c_l	1256.0	$[J/kg^oC]$
Latent Heat	$\mathcal{L}$	395403	$[J/kg]$
Conductivity (solid)	κ_s	197.3	$[W/m^oC]$
Conductivity (liquid)	κ_l	181.7	$[W/m^oC]$
Solidus temp.	T_{sol}	547.8	$[^oC]$
Liquidus temp.	T_{liq}	642.2	$[^oC]$
Initial temp.	$T_i = T_0$	648.9	$[^oC]$
Line heat sink	q	50000	$[W/m]$

Table 2.1: Material and problem data for the thermal validation problem

domain after 1 hour.

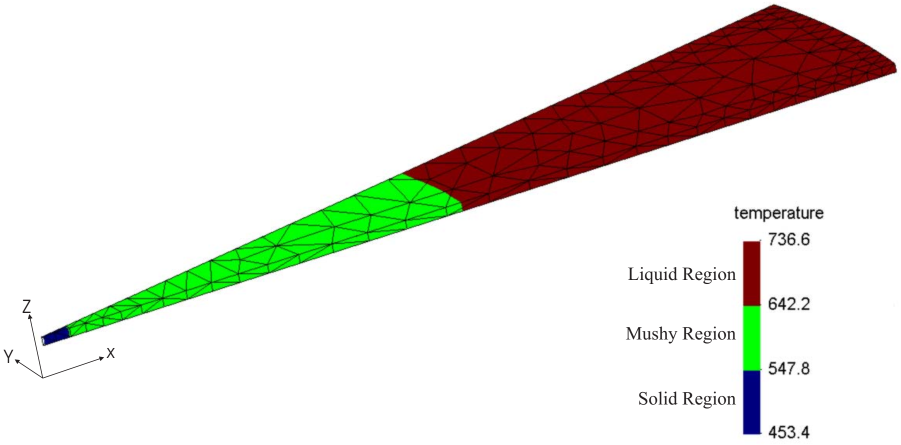

Figure 2.6: FEM mesh and temperature distribution at time t=1 hour

2.6 Heat Source Modeling in Welding

The moving heat source is implemented as a typical transient formulation where the heat source moves along the part with time. In order to model the heat source the 3-dimensional double ellipsoid proposed by Goldak et al. [GCB84] as shown in Figure 2.7 is studied. One characteristic of the double ellipsoid geometry is that it can be easily changed to model both the shallow penetration arc welding processes and the deeper penetration laser and electron beam processes. The heat flux distribution is Gaussian along the longitudinal axis. The front half of the source is a quadrant of one ellipsoidal source while the rear half is a quadrant of another ellipsoidal source. Four parameters define each ellipsoid. Physically, they correspond to the dimensions of the molten zone. Knowing the cross-section of the molten zone from experiment, the heat source parameters can be determined. As a first approximation, Goldak et al. [GCB84] assume that it is reasonable to take the distance in front of the source equal to one half of the weld width and the distance behind the source equal to twice the weld width.

The equivalent heat input to simulate arc heating effects, is assumed as a constant internal heat generation per unit volume.

It is convenient to introduce a coordinate, ξ, fixed on the heat source and moving with it. The moving reference frame on the heat source is related to the coordinate fixed on the work piece by:

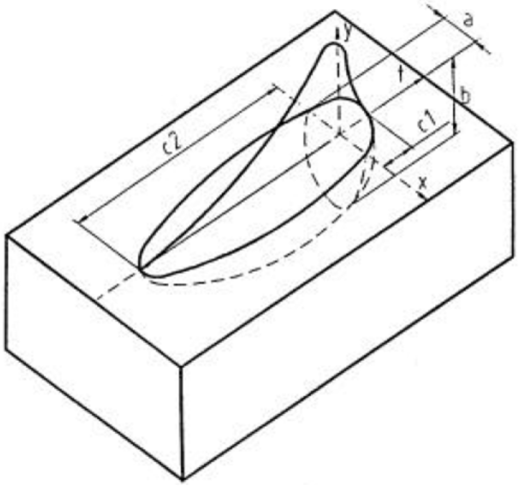

Figure 2.7: Heat source Goldak double ellipsoid

$$\xi = z - v(t - \tau) \tag{2.25}$$

where v is the welding speed, τ is a time lag necessary to define the position of the heat source at time $t = 0$. The weighting fractions associated with the front and rear ellipsoids are denoted by f_f and f_r, respectively, and these fractions are specified to satisfy $f_f + f_r = 2$. Let us denote q the power density in W/m^3 within the ellipsoid, and let a , b and c denote the semi-axes of the ellipsoid parallel to the x, y, ξ axes. Then the power density distribution, inside the front quadrant, is specified by

$$q(x, y, \xi) = (\frac{6\sqrt{3} f_f Q}{abc_f \pi \sqrt{\pi}}) \exp(-3\frac{x^2}{a^2}) \exp(-3\frac{y^2}{b^2}) \exp(-3\frac{\xi^2}{c_f^2}) \tag{2.26}$$

and in the rear quadrant is specified by

$$q(x, y, \xi) = (\frac{6\sqrt{3} f_f Q}{abc_r \pi \sqrt{\pi}}) \exp(-3\frac{x^2}{a^2}) \exp(-3\frac{y^2}{b^2}) \exp(-3\frac{\xi^2}{c_r^2}) \tag{2.27}$$

In equations (2.26) and (2.27) , Q is the heat available at the source. For an electric arc the heat available is

$$Q = \eta V I \tag{2.28}$$

where η is the heat source efficiency, V is the arc voltage, and I is the arc current. The parameters a, b, c_f and c_r are independent, and can take on different values for the front and rear quadrants of the source, to properly model the weld arc. One characteristic of this model is that start and stop effects of the heat source can be taken into account.

The spatial distribution of heat is calculated from equations (2.26) and (2.27) and is applied on elements as a volumetric heat generation.

2.6.1 Verification

In order to verify the developed moving heat source model, a 3D finite element model of a thick plate was generated. Because of symmetry a half of the welding plate was meshed. Figure 2.8 shows the problem geometry used in the 3D FEM analysis.

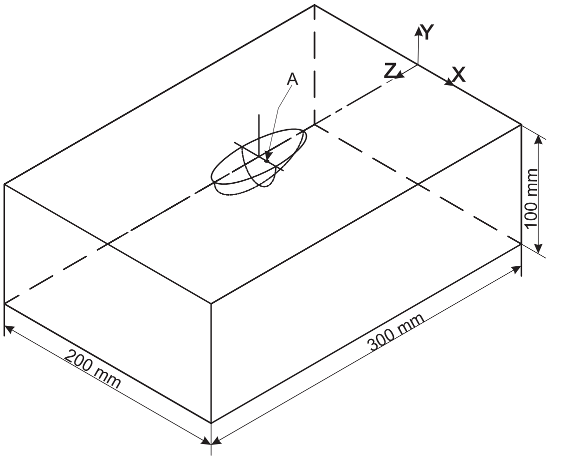

Figure 2.8: Geometry used in the 3D FEM verification analysis.

The model uses the same heat source distribution and material properies as those in Goldak's work and are summarized in tables 2.2, 2.3 and 2.4.

Arc Parameter	Symbol	Value	Unit
Current	I	1170	A
Voltage	U	32.9	V
Efficiency	η	0.95	–
Total Heat	Q	36538.35	W
Speed	v	5	mm/s

Table 2.2: Arc parameters

Figure 2.9 plot the top surface temperature distribution along the x axe at 11.5 seconds after the arc passed. The numerical results we have computed are compared with the 2D Goldak solution and the experimental test of Cristensen.

Parameter	Value	Unit
a	20	mm
b	20	mm
cf	15	mm
cr	30	mm
ff	0.6	–
fr	1.4	–

Table 2.3: Goldak's Parameters

Parameter	Symbol	Value	Unit
Density	ρ	7200.0	$[kg/m^3]$
Specific Heat, (solid)	c_s	680.0	$[J/kg^oK]$
Specific Heat, (liquid)	c_l	680.0	$[J/kg^oK]$
Latent Heat	$\mathcal{L}$	291660	$[J/kg]$
Conductivity (solid)	κ_s	34.0	$[W/m^oK]$
Conductivity (liquid)	κ_l	$2\kappa_s$	$[W/m^oC]$
Solidus temp.	T_{sol}	1774	$[^oK]$
Liquidus temp.	T_{liq}	1763	$[^oK]$
Initial temp.	T_0	283	$[^oK]$

Table 2.4: Material data for thermal problem

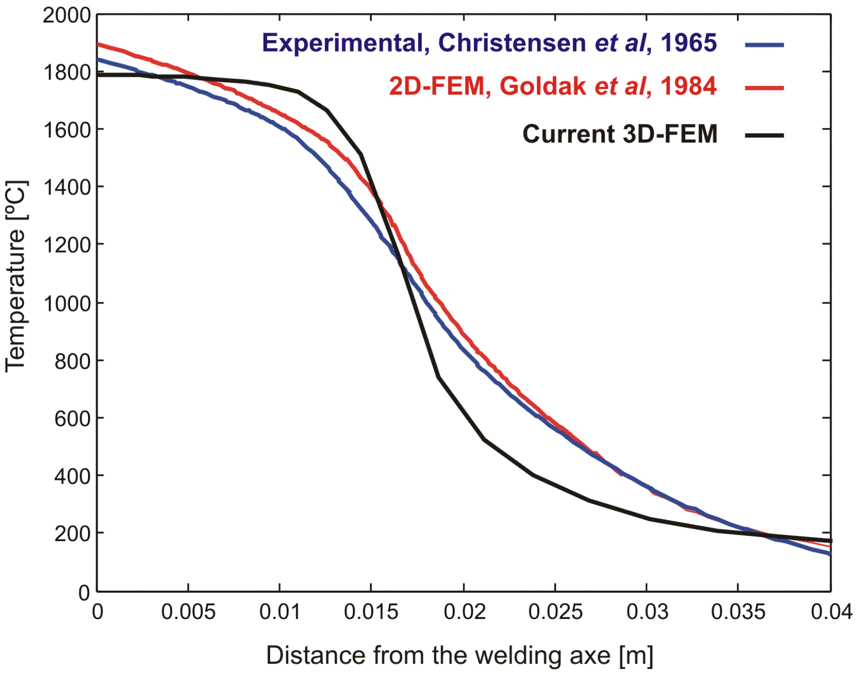

Figure 2.9: Comparison of the present 3D model solution with Goldak's 2D FEM [GCB84] solution and Christensen [CDG65] experimental results.

In order to further validate the heat input moving source, the implemented Goldak's model was compared with the analytical solution for the transient temperature field of a semi-infinite body subjected to 3-D power density moving heat source proposed by Nguyen et al. [NOM$^+$99, NMSO04] and revised by Fachinotti [Fac08]. Same geometry, material and problem parameters, as in the previous validation were used. Figure 2.10 shows the semi-analytical transient temperatures at point $A = (5, 0, 150)$ (see Figure 2.8) and the corresponding current model temperatures at the same point.

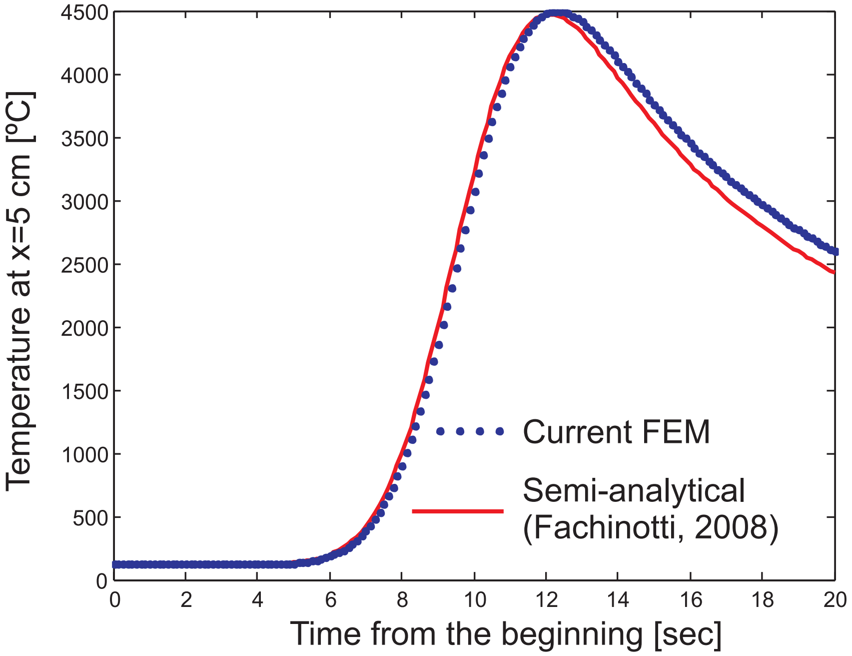

Figure 2.10: Comparison of the present 3D model solution with the Nguyen's semi-analytical solution [NOM$^+$99, Fac08].

Chapter 3

Metallurgical Model

A kinetics based model was integrated into the multiphysics finite element program to compute the time evolution of the microstructure [Lin01]. The material properties required for the non-linear thermomechanical analysis are temperature and phase dependent, and this dependency is accounted for by computing the microstructure evolution and using this information to estimate the material properties. This is done by assigning temperature dependent material properties to each phase and applying mixture rules to predict macro material properties.

3.1 Metallurgical Material Model

Welding operations in steel involve solid state structural transformations. Austenite forms during heating if the temperature becomes higher than Ac3 and it will decompose, during cooling, bellow Ar3. Depending on cooling rate, ferrite, pearlite, bainite and/or martensite will be formed. These transformations induce thermal, metallurgical and mechanical effects in the material, some of which cause:

- changes in thermal properties of the material;
- changes in mechanical properties of the material;
- changes in isotropic specific volume between parent and product phases.

This makes the material properties strongly dependent on temperature and temperature history.

The method used in this work to account for the temperature dependency of the material properties is to calculate microstructure evolution and assign temperature dependent material properties to each phase. The phase properties are combined using a linear mixture rule to obtain macro material properties.

3.2 Modeling the kinetic of the Solid-State phase transformations in metals

In the present work, only solid state transformations that occur during the cooling stage of welding processes are accounted for. An instantaneous austenization model was assumed.

Therefore no other solid-state phase than austenite will exist above Ac3 temperature. We use data obtained from isothermal Temperature-Time-Transformation (IT) curves to predict the evolution of transformations during continuous cooling.

Austenite decomposition into ferrite, pearlite or bainite is driven mainly by diffusion of carbon atoms, and is therefore said to be a diffusive transformation. This case is described by an isothermal Avrami-type[Avr39, Avr40] evolution law (also known as Johnson-Mehl-Avrami-Kolmogorov or JMAK law). The use of this equation to calculate the fraction transformed during cooling is related with the Scheil's additivity rule [Sch35], which states that the fraction which transforms at any given temperature is a function only of the proportion of the metal already transformed and the temperature T.

The diffusionless transformation from austenite to martensite takes place at the highest cooling rates and it is described by the Koistinen-Marburger formulae.

3.2.1 Diffusive kinetics

The kinetics of diffusion-controlled transformations was extended by Jones and Bhadeshia [JB97] and followed by other authors (e.g. Reti et. al.[RFF01]) to model austenite multi-phase decomposition.

For an isothermal transformation at temperature T the volume fraction y_i of the product constituent k at time t is:

$$y_k(t) = Y_k(t)\left[1 - \exp\left(-B_k t^{m_k}\right)\right], \tag{3.1}$$

where B_k, m_k and Y_k are parameters that depend on the temperature T; and k (ferrite, pearlite, bainite) are phase products involved in the reaction.

The coefficients $B_i = B_i(T)$ and $m_i = m_i(T)$ can be determined from isothermal transformation diagrams (IT-diagrams). IT-diagrams that give the start and final transformation times for a giving temperature. The parameter $Y_i = Y_i(T)$ is the maximum volume fraction of the precipitating phase i that follows an isothermal transformation at temperature T and has to be determined experimentally.

3.2.2 Martensite kinetics

During cooling, when the temperature reaches the M_s temperature, austenite starts to transform into martensite.

The martensitic volume fraction is usually described by the Koistinen-Marburger (KM) law:

$$y_m = Y_m\left(1 - \exp\left(-\widetilde{k}(M_s - T)\right)\right), \qquad T < M_s, \tag{3.2}$$

where Y_m is the residual volume fraction of austenite at M_s, and $\widetilde{k}$ describes the martensitic development as function of temperature ($\widetilde{k} = 0.011$ for steels).

3.2.3 The additivity-rule

We based our approach on the additivity rule, where cooling curve is divided into successive isothermal steps.

From the fraction y_k^i transformed at the end of the time step t^i, the new transformed fraction at the end of this step ($t^{i+1} = t^i + \Delta t^{i+1}$) is determined by

$$y_k^{i+1} = Y_k^{i+1}\left(1 - \exp\left(-B_k^{i+1}(\hat{t}^i + \Delta t^{i+1})^{m_k^{i+1}}\right)\right), \tag{3.3}$$

where all the parameters are evaluated at T^{i+1} and $\hat{t}^i$ is a fictitious time defined as:

$$\hat{t}^i = \left(-\frac{\ln\left(1 - \frac{y_k^i}{Y_k^{i+1}}\right)}{B_k^{i+1}}\right)^{1/m_k^{i+1}} \tag{3.4}$$

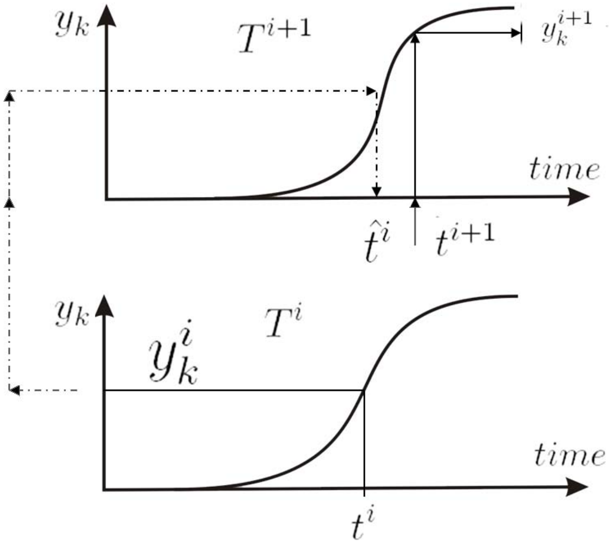

Figure 3.1: Fictitious time determination

3.2.4 The JMAK-rate model

Strictly speaking, the additivity rule holds only for isokinetic reactions, i.e., reactions where the nucleation rate is proportional to the growth rate. Mathematically, it can be shown [LJ97, RF99] that the transformation described by equation (3.1) is isokinetic only if m does not depend on temperature. If it is not the case, the additivity rule is no longer valid in a strict mathematical sense. Therefore, the evolution of the transformed phase during non-isothermal processes should not be modelled as a series of isothermal steps but computed by integrating the rate form of the JMAK equation, written as the autonomous differential equation

$$\dot{y}_k(t) = B_k^{1/m_k} m_k (Y_k(t) - y_k) \left(\ln \frac{Y_k(t)}{Y_k(t) - y_k} \right)^{1-1/m_k} \qquad \forall t > 0, \tag{3.5}$$

$$y_k(0) = y_{k0}, \tag{3.6}$$

where the superimposed dot indicates time derivative.

Regarding the initial condition, y_{k0} should be null but it is often assigned a small value in order to facilitate the numerical integration of equation (3.5), particularly when explicit methods are used.

In order to integrate equation (3.5), the following single-step algorithm will be used:

$$\frac{y_{k_{i+1}} - y_{k_i}}{\varDelta t_{i+1}} = B_{k_{i+\theta}}^{1/m_{k_{i+\theta}}} m_{k_{i+\theta}} (Y_{k_{i+\theta}} - y_{k_{i+\theta}}) \left(\ln \frac{Y_{k_{i+\theta}}}{Y_{k_{i+\theta}} - y_{k_{i+\theta}}} \right)^{1-1/m_{k_{i+\theta}}}, \tag{3.7}$$

where, for any variable λ,

$$\lambda_{i+\theta} = \lambda_i + \theta(\lambda_{i+1} - \lambda_i) \tag{3.8}$$

with $0 \leq \theta \leq 1$. Particularly, $\theta = 0$ gives the explicit, conditionally stable, first-order accurate forward-Euler (fE) method; $\theta = 1$ gives the implicit, unconditionally stable, first-order accurate backward-Euler (bE) method, and $\theta = 0.5$ gives the implicit, unconditionally stable, second-order accurate Crank-Nicolson (CN) method. For the implicit methods, equation (3.7) is nonlinear and has to be solved numerically using iterative methods.

3.3 Generating CCT-diagrams from a IT-diagram

Let us consider the pearlite portion of the IT-diagram of a SAE 6150 steel, as defined by Lusk and Jou [LJ97], with:

$$m_{pearlite} = 3.76 + 0.0235(600 - T), \tag{3.9}$$

$$B_{pearlite} = 4.3099 \times 10^{-10} \exp\left(-4.2355 \left(\exp\left(4.9374 \times 10^{-5}(602.55 - T)^2\right)\right)^2\right), \tag{3.10}$$

where T is given in degrees Celsius. The C-curves corresponding to 1% and 99% of transformed phase are plotted with solid lines in Figure 3.2.

Lusk and Jou's CCT-diagram was obtained for an unspecified exponential cooling history. Here, in an attempt to approach Lusk and Jou's conditions, the following exponential cooling law is imposed

$$T = T_s - \frac{\exp(c \quad t) - 1}{\exp(c \quad t_f) - 1}(T_s - T_f), \tag{3.11}$$

where T is given in degrees Celsius, t in seconds, $c = 5. \times 10^{-4}$, $T_s = 660^o$C, $T_f = 430^o$C, and t_f is the time spent to cool from T_s to T_f, varying between $10^{2.2}$ to 10^4 sec.

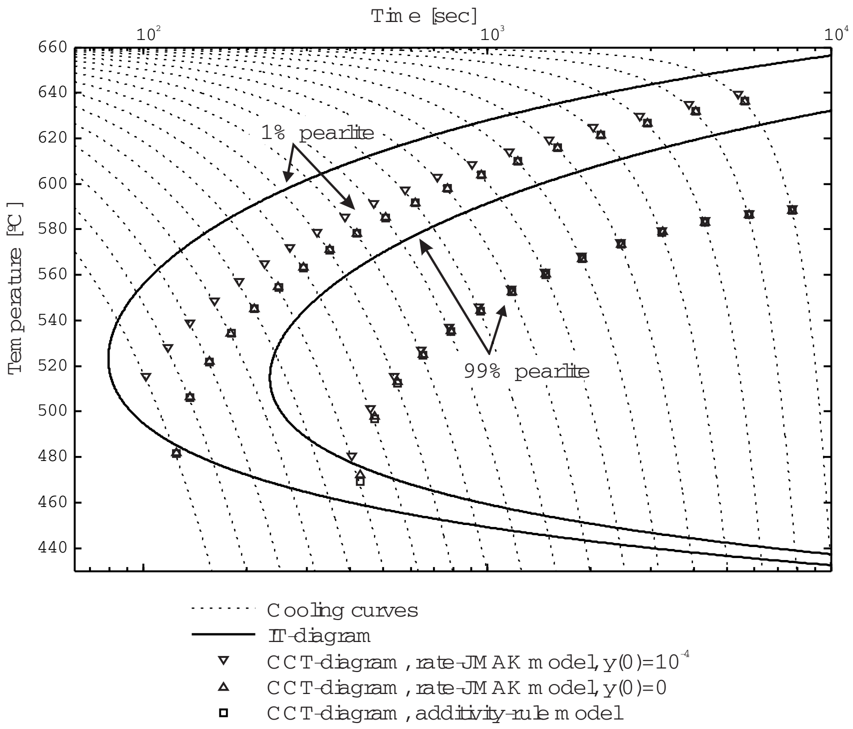

Figure 3.2: IT-diagram and derived CCT-diagrams

Furthermore, in order to compare with Lusk and Jou's results, the transformation is assumed to be complete (i.e., $Y_k = 1$) in the whole range of temperatures considered.

The time step Δt, defining either the duration of each isothermal step when the additivity rule is applied or the time step used for integrating equation (3.5), is set to $t_f/4000$.

Figure 3.2 shows the CCT-diagram computed on the basis of the given IT-diagram using both the model based on the additivity rule and the JMAK-rate model.

When equation (3.5) is solved with $y_{k0} = 10^{-4}$ as initial condition (the value 10^{-4} is recommended in several articles by Lusk and coworkers [BPK$^+$96, LL99, LJR$^+$01, LWSL03]), a difference, with the results obtained by using the Additivity Rule (AR) model, is observed. The difference is similar to that observed in [LJ97], which had motivated these authors to criticize the applicability of the additivity rule for transformation kinetics where m depends on the temperature. However, taking $y_{k0} = 0$, the solution of equation (3.5) is in excellent agreement with that obtained by the additivity rule.

Now, in order to test accuracy with respect to the time step size, the AR model and the rate-JMAK model integrated with fE, bE and CN methods were applied to predict the pearlite fraction at the end of the exponential cooling history given by equation (3.11) with $t_f = 5$ min, that is

$$T = 660. - 1421.207\,(\exp(0.0005t) - 1)\,, \tag{3.12}$$

where T is given in degrees Celsius and t in seconds.

The computed pearlite fractions are plotted on the left of Figure 3.3.

In order to evaluate the evolution of the error as the time step increases, considering that an exact analytical solution does not exist, the exact value y_{exact} is approximated by the average of the different numerical solutions for an extremely fine time step (0.01 sec), $y_{exact} \approx y_{ave} = 0.36360496$.

As shown on the right of Figure 3.3, compared to fE- and bE-rate-JMAK models, the AR model has the same convergence rate but its error is two orders of magnitude smaller than the former ones. The CN-rate-JMAK model converges faster than fE- and bE-rate-JMAK models, but its accuracy remains poorer than that of the AR model for typical time step sizes (0.1 to 1 sec), and as poor as fE- and bE-rate-JMAK models for larger time steps.

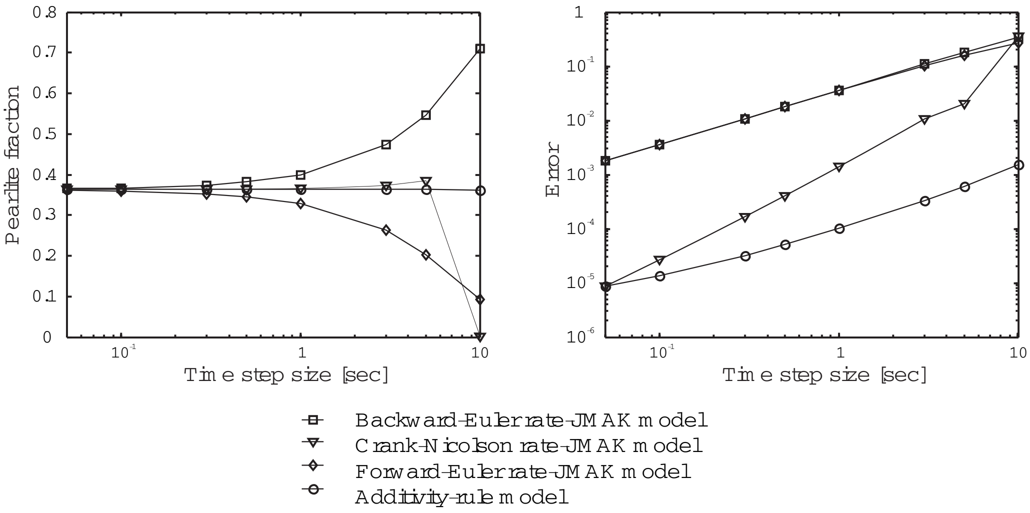

Figure 3.3: Pearlite fraction after 5 min for the cooling history given by equation (3.12), as a function of the time step used for tracking the fraction evolution.

Regarding the computational cost, the fE-rate-JMAK and AR models are the cheaper ones, since the function for updating y_k is explicit. On the other hand, using bE- and CN-rate-JMAK models, the evolution of y_k is governed by a nonlinear equation to be solved numerically by an iterative process. Additionally, as demonstrated by the influence of the initial value y_{k0}, at the beginning of the transformation, very small variations of y_k correspond to large variations of t, and in such case equation (3.7) must be solved with a very strict convergence criterion (10^{-12} for the variation of y_k is adopted), which increases the computational cost.

Therefore, regarding accuracy and computational cost, is concluded that the AR model results the best scheme for numerical modelling of non-isothermal transformations, even if the transformation is not isokinetic.

3.3.1 Multi-phase CCT diagrams

An additional example of the implemented formulation is proposed. A CCT diagram diagram is obtained with the implemented code. Taking as input an isothermal transformation diagram (Figure 3.4) that describes ferritic and pearlitic transformations, and applying the multi-phase transformation model for different constant cooling rates ($\dot{T} = constant$) a continuous cooling transformation diagram is derived and shown in Figure 3.5.

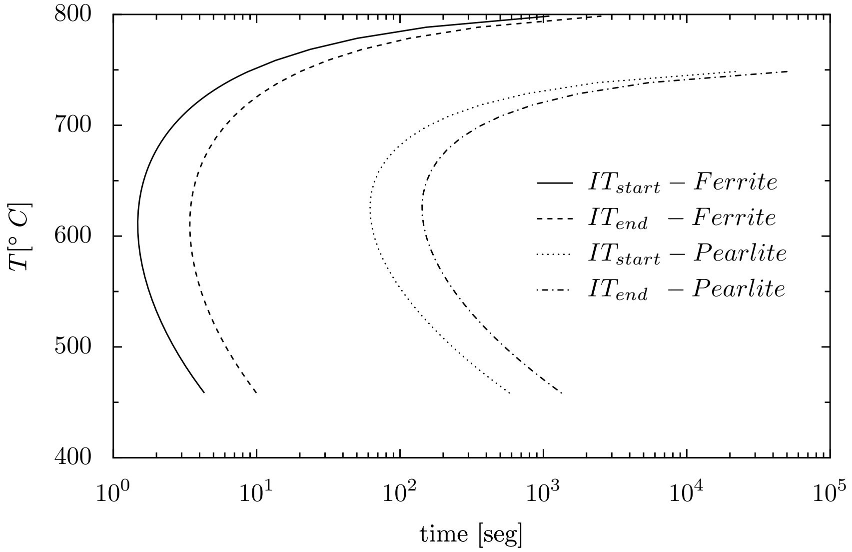

Figure 3.4: IT-diagram

The computed phase fractions vs. time for multi-phase isothermal transformations are also plotted on Figure 3.6.

3.4 Mixture Rules and Material Properties

The material properties are computed by assigning temperature dependent properties to each phase. They are combined by using linear mixture rules to obtain macro materials properties. The general formula for overall macro properties based on the properties for the different k phases is

$$\hat{P}(T,t) = \sum_k y_k(T,t)\hat{p}_k(T) \tag{3.13}$$

where y_k = volume fraction of phase k; $\hat{p}_k$ = material property for phase k; $\hat{P}$ = macro property.

The material properties computed by the mixture rule are heat capacity, heat conductivity, Young modulus, yield limit, hardening modulus, thermal expansion coefficient and Poisson ratio.

3.5 Application

Let us consider the Jominy end-quench test, as treated by Hömberg [Höm96].

The material is an eutectoid carbon steel C1080, whose IT-diagram is observed in Figure 3.8. This diagram is digitalized by taking a series of points (t, T) on two C-curves. Intermediate values are obtained by piecewise-cubic Hermite interpolation based on the gathered points.

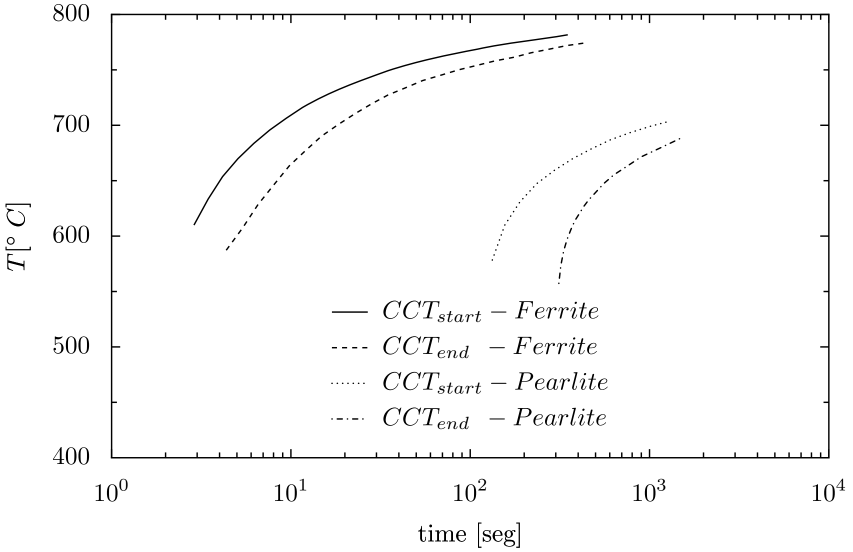

Figure 3.5: CCT-diagram

Then, taking one point on each curve for a given temperature T, the parameters $B(T)$ and $m(T)$ of the JMAK law are computed. The so-determined values of m and B are plotted in Figure 3.9.

Average values are adopted for the mass density ($\rho = 7200.\text{kg/m}^3$), the thermal conductivity ($\kappa = 34.\text{W/(m}^\circ\text{C))}$ as well as for the specific heat ($c_p = 680.\text{J/(kg}^\circ\text{C))}$ used to define the sensible part of the enthalpy of each constituent. The total enthalpy $\mathcal{H}$ is defined as

$$\mathcal{H} = c_p T - L_p p - L_m m, \tag{3.14}$$

where $L_p = 77000.\text{J/kg}$ and $L_m = 84000.\text{J/kg}$ are the latent heats released during pearlitic and martensitic transformations, respectively.

For martensitic transformation, it is assumed $M_s = 224^\circ\text{C}$ and $M_f = 100^\circ\text{C}$, values that have been estimated from the IT-diagram in Figure 3.8.

The domain of interest consists of a cylindrical specimen, with radius $R = 1.25$ cm and length $L = 6.25$ cm, which is initially fully austenitic at homogeneous temperature $T^0 = 720.^\circ\text{C}$, and suddenly cooled by applying a water jet to the lower end, according to the convection heat exchange law:

$$q_{wj} = h_{wj}(T)(T_{wj} - T), \tag{3.15}$$

with $T_{wj} = 25.^\circ\text{C}$, and

$$h_{wj}(T) = -1670. + 108.T - 0.0977.T^2 \tag{3.16}$$

given in $\text{W/(}^\circ\text{C m}^2)$ for T in °C [Höm96].

Additionally, the specimen exchanges heat with the environment through its lateral surface. This heat flux is mainly radiative and is defined as [MLA+02]

$$q_{ls} = \varepsilon\sigma(T_{env}^4 - T^4), \tag{3.17}$$

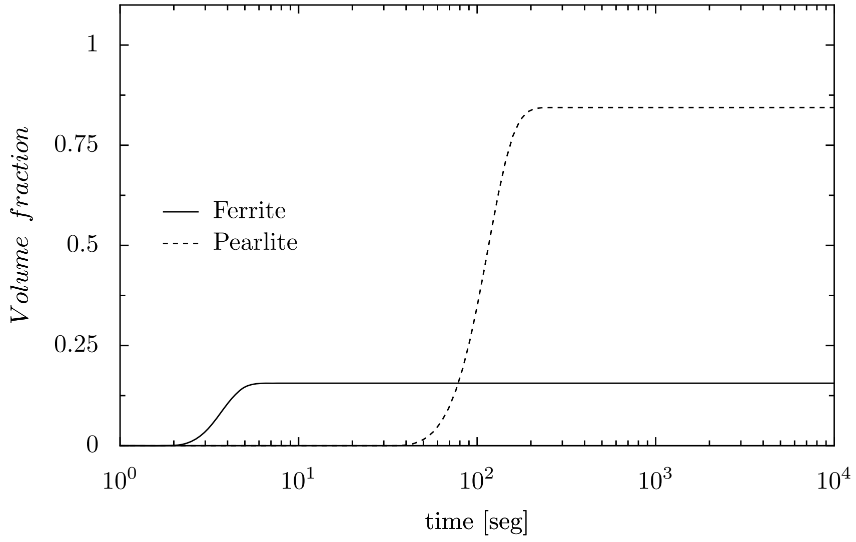

Figure 3.6: Isothermal evolution of phase fractions of ferrite and pearlite at 650°C

where $\varepsilon = 0.8$ is the surface emissivity, σ is the Stefan-Boltzmann constant, and $T_{env} = 25.°\mathrm{C}$ is the environment temperature. We make this boundary conditions fit equation (2.13) by defining the non-linear radiative heat transfer coefficient

$$h_{ls}(T) = \varepsilon\sigma(T_{env}^2 + T^2)(T_{env} + T). \tag{3.18}$$

The upper end is supposed to be adiabatic.

Linear tetrahedra finite elements are used for the spatial discretization of the cylinder, as shown in Figure 3.10. Considering that the specimen, as well as the boundary conditions, is symmetric with respect to the axis of the specimen, we only model a small sector of the cylinder. Even if an axisymmetric model is best suited for this particular problem in terms of computational cost, a 3D model is used keeping in mind future industrial applications.

The heat equation is integrated in time using a time step $\Delta t_{HE} = 0.5$ sec, while the duration of each isothermal step is $\Delta t_{AR} = 0.1$ sec.

Figure 3.11 shows the distribution of the different constituents along the axis of the specimen, as computed using different models. First, the case of martensitic transformation defined by equation (3.2) is considered. At the quenched end ($z = 0$), the material is mainly martensitic ($\approx$ 89%), with a small fraction of retained austenite ($\approx$ 11%). From this end to a section located at $z \approx 7.\,\mathrm{mm}$, the material presents the three constituents: martensite, austenite and pearlite. The remaining material is predicted to have a fully pearlitic microstructure. Compared to experimental results [Ame77] as well as to previous numerical results [Höm96], the martensite fraction is understimated at the quenched end. However, the estimated width of the martensitic region is closer to the experimental result [Ame77] than that of Hömberg [Höm96].

The underestimation of the martensite fraction is associated to the use of the KM formula. In fact, equation (2.11) has been evaluated at the lowest temperature attainable during the cooling process $T_{min} = T_{wj} = T_{env} = 25°\mathrm{C}$ gives $m(T_{min}) \leq 88.80\% = m_{max}$, that is the maximum martensite fraction attainable under the present conditions.

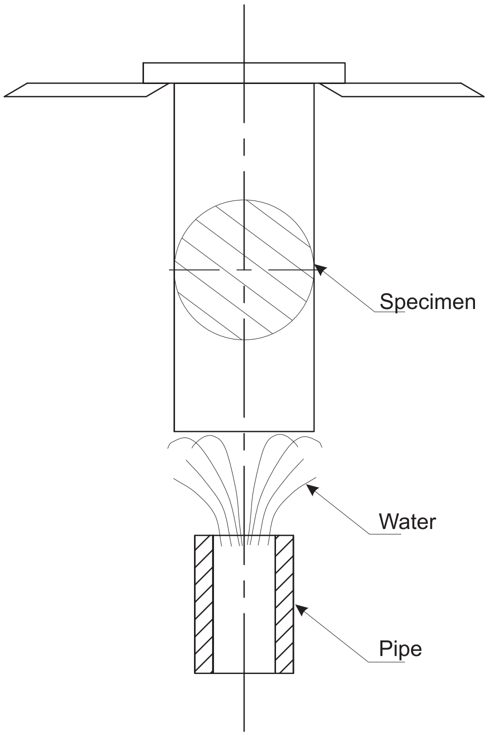

Figure 3.7: Jominy end-quench test.

The Yu law[Yu77], for martensite evolution, enables the modelling of the complete austenite decomposition into martensite by introducing the temperature M_f such that $m(M_f)/\bar{\gamma} = 1$. The current model, using Yu law for martensitic transformation, gives the better results in terms of agreement with the experimental measures [Ame77]. In this case, no austenite is retained at the end of the process. Note that the pearlite fraction is practically identical to that computed using the KM law for martensite evolution.

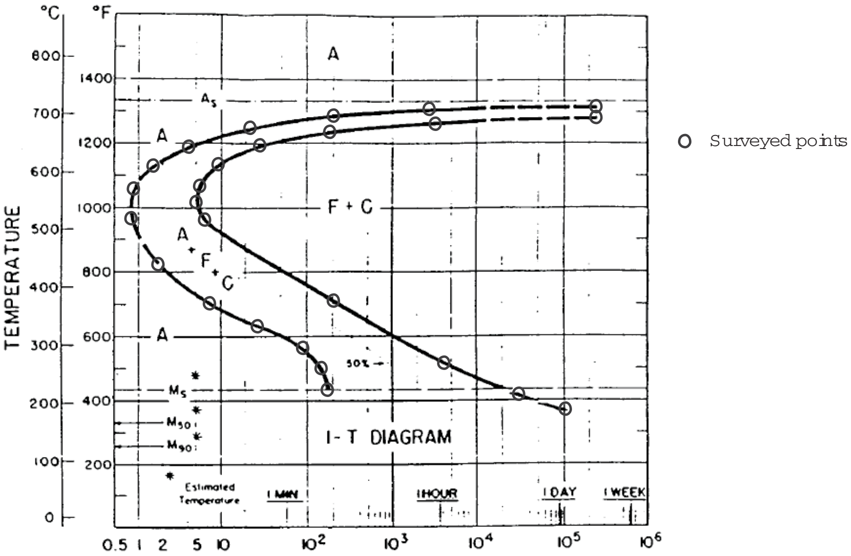

Figure 3.8: IT-diagram for C1080 steel.

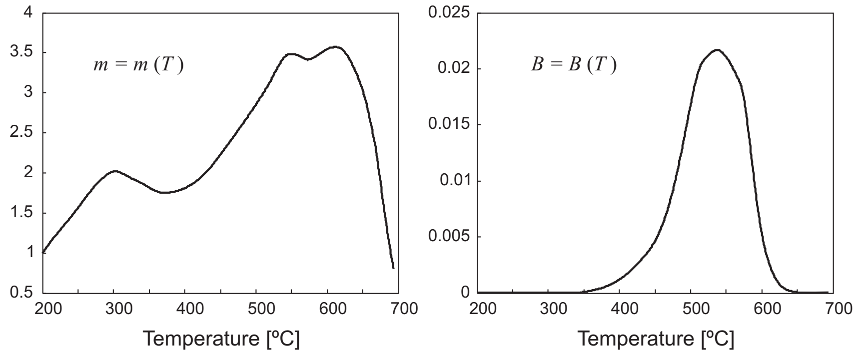

Figure 3.9: Parameters for the Johnson-Mehl-Avrami-Kolmogorov law computed from the IT-diagram for C1080 steel.

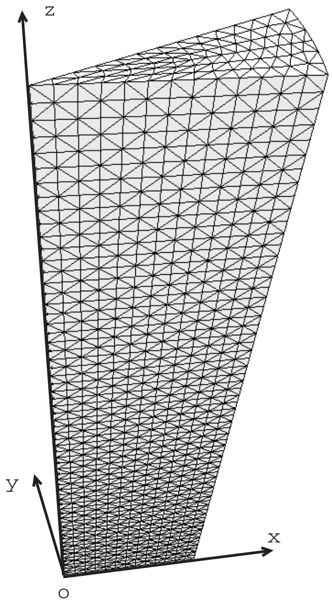

Figure 3.10: Linear tetrahedral finite element mesh of a longitudinal sector the specimen.

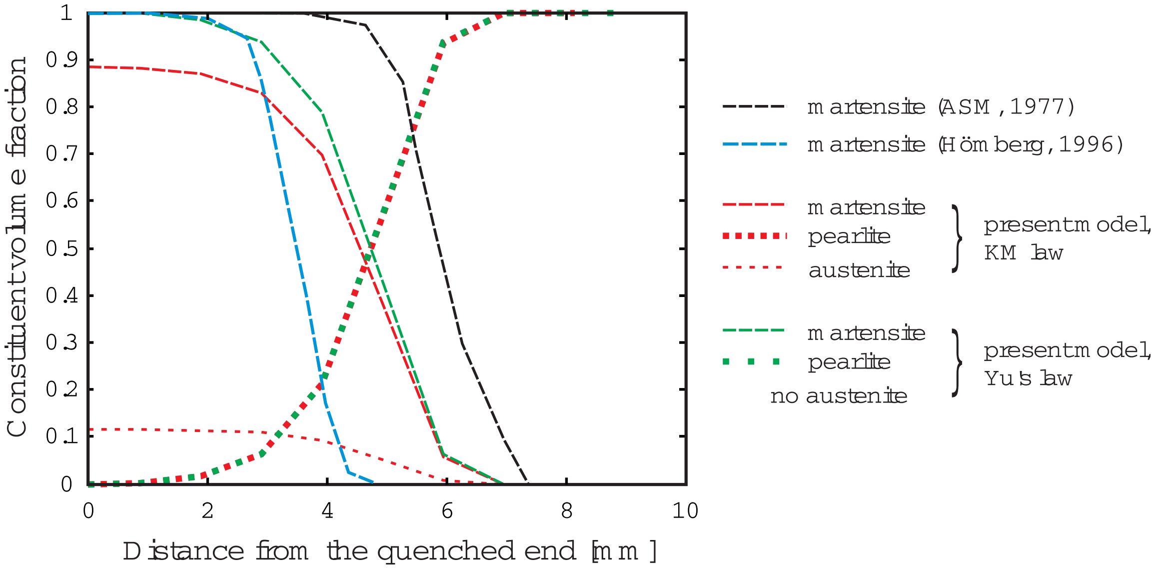

Figure 3.11: Volume fraction of the different constituent along the axis of the specimen.

Chapter 4

Mechanical problem

During a thermal welding process, the weld site and immediate surrounding area experience different rates of heating/cooling and thus expansion/contraction. This effect leads to considerable thermal strains. Due to the heat application localized nature, the expansion due to these strains is constrained by the cooler material away from the site of the applied heat. The physical and chemical properties of the material also change at the weld site and heat affected zone (HAZ), both during and after the welding process. These changes affect mechanical material properties, and must be taken into account in the mechanical analysis.

Due to the intrinsic three-dimensional nature of loads, boundary conditions and geometry usually involved in welding processes, a 3D mechanical model was implemented. It should be noted that the weld pool itself is not modelled in the mechanical analysis. This is only a soft region serving as the means of the heat input to the thermomechanical model. In this sense, the use of cut-off temperature, or zero-strength temperature, ZST, was assumed. This is also the temperature above which no further changes in material properties are accounted for in the mechanical analysis. A schematic diagram of the mechanical properties in the solid/liquid interface of steels in the mushy zone and the corresponding structure are shown in Figure 4.1. Above ZST, the steel has no strength and behaves as a liquid.

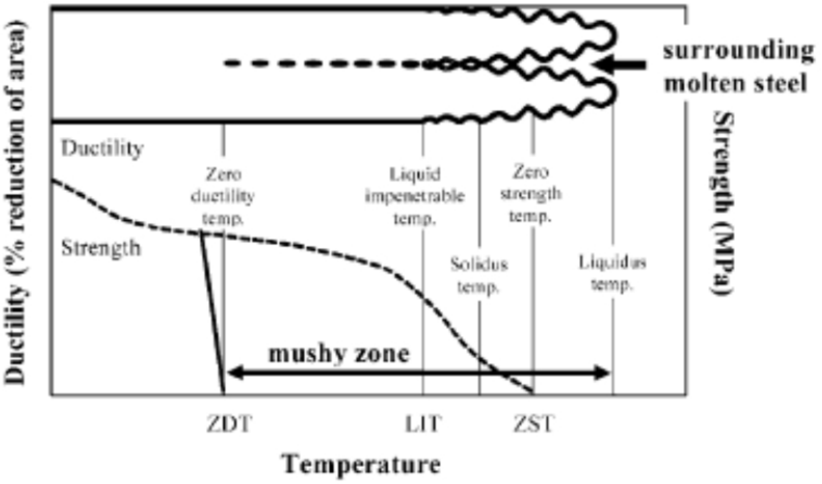

Figure 4.1: Mechanical properties of steel in the mushy zone

The thermoelastic material behavior, is for most cases, based on a hypoelastic version of Hooke's law with inclusion of thermal strains. The Young's modulus and the thermal dilatation coefficient, are the most important parameters. Poisson ratio has a smaller influence [TM91] on the residual stresses and deformations. The plastic material model used for solidified metal was a rate-independent model with an associative J2 von Mises law and isotropic hardening. The argument for using rate-independent plasticity at high temperatures is based on the involved time scales [Lin01]. In the the weld thermal cycle the material has a high temperature during a relatively short time, and therefore the accumulated rate-dependent plasticity may be neglected.

Inertial effects are ignored in momentum balance equations, according to the assumption of null aceleration within the solid.

4.1 Melting-Solidifying Behavior

It is recognized that finite element techniques, with standard constitutive material modelling, yield good solutions in thermal stress analysis. Even when the solid is subjected to temperatures near the solidification ones. However, there are particular aspects in the formulation for melting/solidifying problems that need to be carefully considered.

Three different configurations for every material point and its neighborhood (Figure 4.2) are considered for the mechanical simulation of this process:

i) the reference configuration (B), in which the particle label is assigned;

ii) the (intermediate) natural configuration (B^0) which corresponds to that state where the material point solidified just below the zero strength temperature (ZST), and started to develop mechanical strength;

iii) the current configuration (B^t).

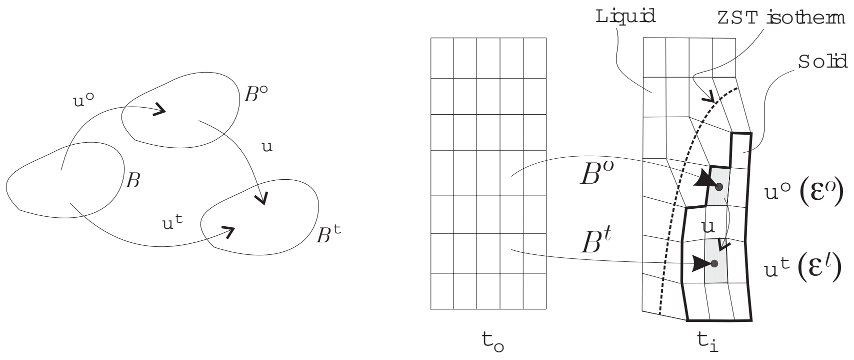

(a) (b)

Figure 4.2: Reference (B), natural (B^0) and current (B^t) body configurations in the solidification problem

Note that, since the solidification time instant is not the same one for all points in the domain of analysis, each material point has its own (intermediate) natural configuration.

Defining $\boldsymbol{u}^o$ as the displacement from the reference to the natural configuration, $\boldsymbol{u}^t$ the displacement from the reference to the current configuration and $\boldsymbol{u}$ the displacement from the natural to the current configuration, one can write:

$$\boldsymbol{u}^t = \boldsymbol{u} + \boldsymbol{u}^o \tag{4.1}$$

Usually, when a finite element procedure is used, the mesh is defined in the reference configuration (the set of points at time $t = 0$) as depicted schematically in Figure 4.2-b.

Let us consider that $\boldsymbol{X}$ and $\boldsymbol{x}^o$ are coordinate systems in the reference and natural configurations, respectively. As a consequence of the assumption of small deformations introduced to describe motion, and by assuming the existence of the intermediate deformation gradient in the neighborhood of every point, one has: $\nabla_{\boldsymbol{X}} \boldsymbol{x}^o \approx \mathbb{1}$. The same assumption allows us to evaluate the strain $\boldsymbol{\varepsilon} = \nabla^{sym}_{\boldsymbol{x}^o} \boldsymbol{u}$, related to the motion from the natural to the final configurations, by the following approximation:

$$\boldsymbol{\varepsilon} = \nabla^{sym}_{\boldsymbol{x}^o} \boldsymbol{u} \approx \nabla^{sym}_{\boldsymbol{X}} \boldsymbol{u} \tag{4.2}$$

By taking gradients in equation (4.1) and using the assumptions stated above, we can verify the validity of the additive decomposition of strains:

$$\boldsymbol{\varepsilon}^t = \boldsymbol{\varepsilon} + \boldsymbol{\varepsilon}^o \tag{4.3}$$

where $\boldsymbol{\varepsilon}^t = \nabla^{sym}_{\boldsymbol{X}} \boldsymbol{u}^t$ is the strain tensor at the actual configuration (time t) with respect to the reference configuration, and $\boldsymbol{\varepsilon}^o = \nabla^{sym}_{\boldsymbol{X}} \boldsymbol{u}^o$ is the strain at the natural configuration with respect to the reference one.

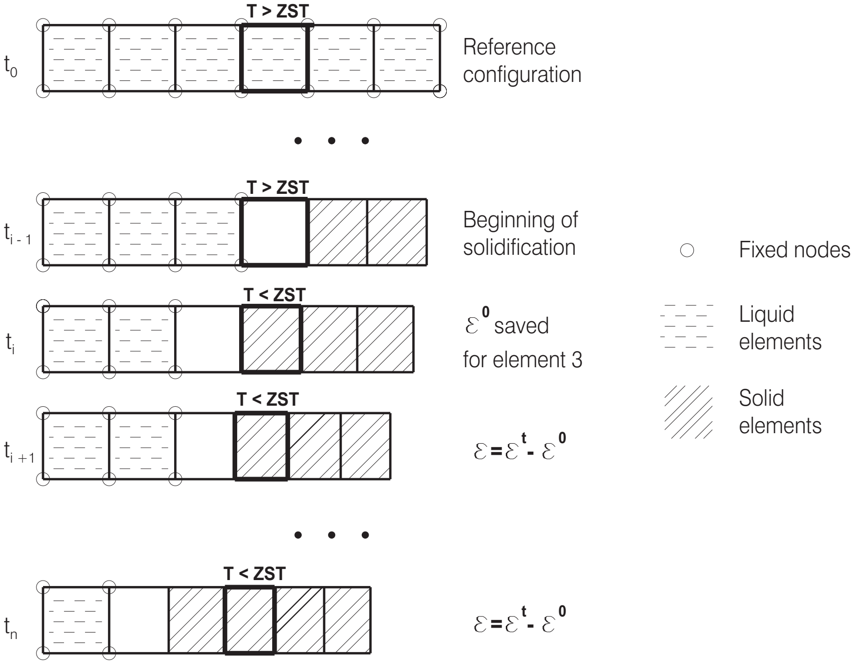

Figure 4.3: Evolution of d.o.f.s and strains in solidification problems

Stresses in the solid shell are directly related to the mechanical strains through the constitutive material law.

In order to test the formulation we selected a standard elastoplastic model, based on the classical J_2 theory with isotropic hardening [SH98] and the von Mises yield criteria.

We remark that for a correct representation of the steel constitutive behavior in the zone of interest, it is mandatory to account for the strong dependence of the material parameters on temperature.

Remarks:

- The strain $\boldsymbol{\varepsilon}^o$ is computed the first time that all nodal temperatures of the considered element fall below the zero strength temperature (ZST), and is stored at the finite element Gauss point as an additional tensorial internal variable. The *Zero Strength Temperature* is defined as the minimum temperature amongst those at which strength is zero [NUM$^+$95a]. Temperatures corresponding to solid fraction values ranging from 0.65 to 0.80 are commonly used for this parameter in the literature [MTZ93, YNO95, WKYO98].

- In this model, the solid phase domain changes with time. This fact introduces some difficulties concerning the mesh definition for the FE analysis. The procedure we have implemented consists in defining a fixed mesh that describes the complete domain, including the liquid and mushy zones. Nodes in the liquid and mushy zones are initially fixed. In subsequent time steps, when the nodal temperatures fall below the ZST, nodal d.o.f.'s are freed and the stiffness contribution of the solidified zone is taken into consideration (see Figure 4.3).

- The described numerical model does not predict the real displacement field inside the solid phase, because the displacement field of the natural configuration is not recorded. However, displacements in the natural configuration of the elements located on the solid surface are known and equal to zero, so the real displacements of the solid surface are correctly approximated.

- The technique of subtraction of the strain term $\boldsymbol{\varepsilon}^o$ from the total strain $\boldsymbol{\varepsilon}^t$ must be emphasized for its simplicity and accuracy. Stress computations based on total strain, without subtraction of the initial strain $\boldsymbol{\varepsilon}^o$, give completely unrealistic results. A fact that may be verified by comparison with results obtained by using the semi-analytical formulation of Weiner et al. [WB63] We note also that this approach is less expensive than that used by other authors based on recording flow strain for liquid elements [LT02].

- Mechanical elements have special treatment during the liquid/solid and solid/liquid phase changes. While the temperature is above the ZST, the corresponding elemental d.o.f.'s are not included in the system of equations for the unknowns of the mechanical problem. This methodology incorporates an advantage compared to other techniques found in literature, such as assigning a very low stiffness to the elements that are in liquid/mushy phases, which brings poor conditioning of the algebraic equation system to be solved.

4.2 Lagrangian formulation of the constitutive equations

According to the local state theory [LC94], at a given instant t the thermodynamic state at any particle $\boldsymbol{X}$ of a material medium is completely defined by the values of a certain number of state variables at this particle. Computations on inelastic materials take advantage of strain-driven formulations, in which state variables are the total strain $\boldsymbol{\varepsilon}$ and a set of phenomenological internal strain-type variables describing material history, together with the temperature field T here assumed to be known a priori.

A linear kinematics is assumed. Even when small strain approximations are often used in this type of problems, one must be aware that even moderate rotations will create spurious stresses [TT83]. Then, the total strain can be additively decomposed as follows:

$$\boldsymbol{\varepsilon} = \boldsymbol{\varepsilon}^e + \boldsymbol{\varepsilon}^i, \tag{4.4}$$

$\boldsymbol{\varepsilon}^e$ being the thermoelastic (reversible) strain and $\boldsymbol{\varepsilon}^i$ the inelastic (irreversible) strain. Either term may play the role of an internal variable, but $\boldsymbol{\varepsilon}^i$ is typically chosen (option followed in this work).

We also adopt a scalar internal variable α, which characterizes isotropic hardening from the phenomenological point of view. The hypothesis of isotropic hardening is widely accepted in welding applications [Lin01, FR00, CT04].

Furthermore, the hardening parameter α is the equivalent inelastic strain:

$$\alpha = \int_0^t \sqrt{\frac{2}{3}}\,\|\dot{\boldsymbol{\varepsilon}}^i(\tau)\|\,\mathrm{d}\tau, \tag{4.5}$$

where $\dot{\boldsymbol{\varepsilon}}^i$ is the inelastic strain rate and $\|\dot{\boldsymbol{\varepsilon}}^i\| = \sqrt{\dot{\varepsilon}^i_{ij}\dot{\varepsilon}^i_{ij}}$ its L_2-norm.

Although driving variables lie in the strain space, response functions (i.e. the yield criterion and the evolution laws) are usually written in terms of their conjugated thermodynamic forces: the stress tensor $\boldsymbol{\sigma}$ (dual of $\boldsymbol{\varepsilon}^e$) and the isotropic hardening variable in stress space, $R = R(\alpha)$.

The stress tensor $\boldsymbol{\sigma}$ depends on $\boldsymbol{\varepsilon}$ and $\boldsymbol{\varepsilon}^i$ through the decomposition (4.4). For linearly-elastic isotropic materials, the stress is defined by the state law:

$$\boldsymbol{\sigma} = \underbrace{\kappa\left[\,\mathrm{tr}\,(\boldsymbol{\varepsilon}^e) - 3\varepsilon_T\right]}_{\sigma_m}\mathbb{1} + \underbrace{2\mu\,\mathrm{dev}(\boldsymbol{\varepsilon}^e)}_{\boldsymbol{s}}, \tag{4.6}$$

where $\kappa = \kappa(T)$ and $\mu = \mu(T)$ are thermo-dependent material properties known as bulk and shear moduli, respectively, ε_T is the thermal strain, $\mathbb{1}$ the second-order unit tensor, $\mathrm{tr}\,(\boldsymbol{\varepsilon}^e) = \varepsilon^e_{ii}$ and $\mathrm{dev}(\boldsymbol{\varepsilon}^e) = \boldsymbol{\varepsilon}^e - \mathrm{tr}\,(\boldsymbol{\varepsilon}^e)\mathbb{1}/3$ are the trace and the deviator of the second-order tensor $\boldsymbol{\varepsilon}^e$, $\sigma_m = \mathrm{tr}\,(\boldsymbol{\sigma})/3$ is the mean stress and $\boldsymbol{s} = \mathrm{dev}(\boldsymbol{\sigma})$ is the stress deviator. Here, the thermal expansion is defined by the thermal linear expansion (TLE) function:

$$\varepsilon_T = \mathrm{TLE}\,(T) = \int_{T_{ref}}^{T} \alpha_T(\tau)\,\mathrm{d}\tau, \tag{4.7}$$

with α_T as the linear thermal expansion coefficient and T_{ref} an arbitrary reference temperature.

The von Mises criterion is defined:

$$f = \|\boldsymbol{s}\| - \sqrt{\frac{2}{3}}\,\left[\sigma_Y + R(\alpha)\right], \tag{4.8}$$

with σ_Y denoting the initial yield stress and $R(\alpha)$ the hardening relation .

Associated to this yield criterion, the following J_2 flow rule is considered:

$$\dot{\boldsymbol{\varepsilon}}^i = \gamma\boldsymbol{n}, \tag{4.9}$$

being $\boldsymbol{n} = \boldsymbol{s}/\|\boldsymbol{s}\|$ the normalized stress deviator defining the normal to the Von Mises yield surface $f = 0$ in the deviatoric-stress space, and $\gamma \geq 0$ the consistency parameter. For plastic materials, γ is determined by means of the consistency condition

$$\gamma\dot{f} = 0. \tag{4.10}$$

Finally, having chosen the equivalent inelastic strain as hardening variable, the flow rule (4.9) completely defines the hardening law:

$$\dot{\alpha} = \sqrt{\frac{2}{3}}\,\|\dot{\boldsymbol{\varepsilon}}^i\| = \sqrt{\frac{2}{3}}\,\gamma. \tag{4.11}$$

4.3 Integration of the evolution equations

Following Simo and Taylor [SH98], the evolution laws (4.9) and (4.11) are discretized using the implicit Euler-backward finite-difference scheme. Then, given the total strain increment $\Delta\boldsymbol{\varepsilon}$ at the particle $\boldsymbol{X}$ during the time interval $[t_n, t_{n+1}]$, $t_{n+1} = t_n + \Delta t$, the material state at $\boldsymbol{X}$ is updated from the previous instant t_n to the current one t_{n+1} by a standard return-mapping algorithm.

Also the consistent tangent matrix was implemented. The correct evaluation of this matrix is essential to achieve good numerical response in the determination of equilibrium condition. In this procedure it has been neglected derivatives of stresses with respect to temperature changes without affecting seriously the convergence rate.

4.4 Finite element implementation

Momentum balance equation ignoring inertial effects

$$\nabla \cdot \boldsymbol{\sigma} + \rho \boldsymbol{b} = 0 \quad \forall \boldsymbol{X} \in \Omega_s, \tag{4.12}$$

subjected to the following boundary conditions

$$\boldsymbol{u} = \bar{\boldsymbol{u}} \quad \forall \boldsymbol{X} \in \partial\Omega_{s,u} \tag{4.13}$$

$$\boldsymbol{\sigma} \cdot \boldsymbol{n} = \bar{\boldsymbol{t}} \quad \forall \boldsymbol{X} \in \partial\Omega_{s,t}, \tag{4.14}$$

leads to the standard quasi-static boundary value problem in solid mechanics [Hug87] which consists in finding the displacement field $\boldsymbol{u}$ that satisfy the integral equations

$$\int_{\Omega_s} \boldsymbol{\sigma} : \nabla^s \boldsymbol{w} dV = \int_{\Omega_s} \rho \boldsymbol{b} \cdot \boldsymbol{w} dV + \int_{\partial\Omega_{s,t}} \bar{\boldsymbol{t}} \cdot \boldsymbol{w} dS, \tag{4.15}$$

throughout the domain Ω_s, for all the admissible displacement weighting functions $\boldsymbol{w}$.

Equation (4.15) is the weak form of the momentum balance equations (4.12), where $\rho\boldsymbol{b}$ is the body-force (per unit volume) and $\bar{\boldsymbol{t}}$ is the traction prescribed over the portion $\partial\Omega_{s,t}$ of the boundary (displacement boundary conditions over the complementary portion $\partial\Omega_{s,u}$ are assumed to hold a priori).

The displacement trial functions are defined as follows:

$$\boldsymbol{u} = \sum_{i=1}^{n_u} N_i \boldsymbol{U}_i \tag{4.16}$$

being N_i the displacement shape function associated to the node $i = 1, 2, \ldots, n_u$, being $\boldsymbol{U}_i$ the nodal displacement

After replacing $\boldsymbol{u}$ in (4.15) by its respective finite element approximation (4.16), and by adopting the shape functions as weight functions (Galerkin formulation), it yields

$$\boldsymbol{R} = \boldsymbol{F}_{int} - \boldsymbol{F}_{ext} = \boldsymbol{0}, \tag{4.17}$$

where

$$\boldsymbol{F}_{int} = \int_{\Omega_s} \boldsymbol{B}^T \boldsymbol{\sigma}(u)\,\mathrm{d}V \tag{4.18}$$

$$\boldsymbol{F}_{ext} = \int_{\Omega_s} \boldsymbol{N}^T \rho \boldsymbol{b}\,\mathrm{d}V + \int_{\partial\Omega_{s,t}} \boldsymbol{N}^T \bar{\boldsymbol{t}}\,\mathrm{d}S \tag{4.19}$$

$\boldsymbol{B}$ is the typical finite element matrix defining the strain-displacement kinematics relation

$$\boldsymbol{\varepsilon}^t = \boldsymbol{B}\boldsymbol{U}. \tag{4.20}$$

The nonlinear system of equations (4.17) is solved iteratively, approximating this system at the i-th iteration using a linear Taylor expansion

$$\boldsymbol{R}_{(\boldsymbol{U}^{(i)})} \approx \boldsymbol{R}_{(\boldsymbol{U}^{(i-1)})} + \boldsymbol{J}_{(\boldsymbol{U}^{(i-1)})} \Delta\boldsymbol{U}^{(i)} = \boldsymbol{0} \tag{4.21}$$

where $\boldsymbol{J} = \mathrm{d}\boldsymbol{R}/\mathrm{d}\boldsymbol{U}$ is the Jacobian or tangent matrix, and $\Delta\boldsymbol{U}^{(i)} = \boldsymbol{U}^{(i)} - \boldsymbol{U}^{(i-1)}$ is the search direction. Iterative correction of variables is defined by:

$$\Delta\boldsymbol{U}^{(i)} = -[\boldsymbol{J}_{(\boldsymbol{U}^{(i-1)})}]^{-1} \boldsymbol{R}_{(\boldsymbol{U}^{(i-1)})} \tag{4.22}$$

As described for the thermal problem, this Newton-Raphson scheme is complemented with line-search procedures to accelerate the convergence.

Mixed $\boldsymbol{u}$-p Formulation

Mixed $\boldsymbol{u}$-p elements use both, displacement and hydrostatic pressure as primary unknown variables. Incompressible material behavior may lead to some difficulties in numerical simulation, such as volumetric locking, inaccuracy of solution, checkerboard pattern of stress distributions, or occasionally, divergence. Mixed $\boldsymbol{u}$-p elements are intended to overcome these problems.

The standard quasi-static boundary value problem in solid mechanics, stated in mixed $\boldsymbol{u}$-p form [Hug87], consists in finding the displacement field $\boldsymbol{u}$ and the mean-stress field p that satisfy the integral equations

$$\int_{\Omega} \boldsymbol{\sigma}_{dev}\,\mathrm{grad}\,\boldsymbol{w}\,\mathrm{d}V + \int_{\Omega} p\,\mathrm{div}\,\boldsymbol{w}\,\mathrm{d}V = \int_{\Omega} \rho\boldsymbol{b}\cdot\boldsymbol{w}\,\mathrm{d}V + \int_{\partial\Omega_\sigma} \bar{\boldsymbol{t}}\cdot\boldsymbol{w}\,\mathrm{d}S, \tag{4.23}$$

$$\int_{\Omega} \left[\mathrm{tr}\,(\boldsymbol{\varepsilon}_M) - \frac{p}{\kappa}\right] q\,\mathrm{d}V = 0, \tag{4.24}$$

throughout the domain Ω, for all the admissible displacement and mean-stress weighting functions $\boldsymbol{w}$ and q, respectively.

Equation (4.23) is the weak form of the momentum balance equations, where $\rho\boldsymbol{b}$ is the body-force (per unit volume) and $\bar{\boldsymbol{t}}$ is the traction prescribed over the portion $\partial\Omega_\sigma$ of the boundary (displacement boundary conditions over the complementary portion $\partial\Omega_u$ are assumed to hold a priori).

The displacement and mean-stress trial functions are defined as follows:

$$\boldsymbol{u} = \sum_{i=1}^{n_u} N_i \boldsymbol{U}_i = \boldsymbol{N}\boldsymbol{U}, \tag{4.25}$$

$$p = \sum_{j=1}^{n_p} N_{p\,j} P_j = \boldsymbol{N}_p \boldsymbol{P}, \tag{4.26}$$

N_i being the displacement shape function associated to the displacement node $i = 1, 2, \ldots, n_u$, $\boldsymbol{U}_i$ the nodal displacement, $N_{p\,j}$ the mean-stress shape function associated to the mean-stress node $j = 1, 2, \ldots, n_p$, and P_j the nodal mean stress.

Appropriate mixed finite elements should be employed in order to deal with the numerical difficulties eventually caused by the inelastically-incompressible behavior of metals. We refer to the classical finite element literature [Hug87, ZT00] for a detailed discussion of admissible $\boldsymbol{u}$- and p-shape functions that guarantee the fulfillment of the Babuška-Brezzi stability conditions.

After replacing $\boldsymbol{u}$ and p by their respective finite element approximations, and by adopting the corresponding shape functions as weight functions (Galerkin formulation), it yields

$$\boldsymbol{R}_1 = \boldsymbol{F}_{int} - \boldsymbol{F}_{ext} = \boldsymbol{0}, \tag{4.27}$$

$$\boldsymbol{R}_2 = \boldsymbol{K}_p^T \boldsymbol{U} - \boldsymbol{M}_p \boldsymbol{P} = \boldsymbol{0}, \tag{4.28}$$

where

$$\boldsymbol{F}_{int} = \int_{\Omega} \boldsymbol{B}^T \boldsymbol{\sigma}_{dev}\, \mathrm{d}V + \boldsymbol{K}_p \boldsymbol{P}, \tag{4.29}$$

$$\boldsymbol{F}_{ext} = \int_{\Omega} \boldsymbol{N}^T \rho \boldsymbol{b}\, \mathrm{d}V + \int_{\partial\Omega_\sigma} \boldsymbol{N}^T \bar{\boldsymbol{t}}\, \mathrm{d}S, \tag{4.30}$$

$$\boldsymbol{K}_p = \int_{\Omega} \boldsymbol{B}^T \mathbb{1} \boldsymbol{N}_p\, \mathrm{d}V, \tag{4.31}$$

$$\boldsymbol{M}_p = \int_{\Omega} \frac{1}{\kappa} \boldsymbol{N}_p^T \boldsymbol{N}_p\, \mathrm{d}V, \tag{4.32}$$

$$\tag{4.33}$$

In the above equations, symmetric second order tensors like the stress deviator $\boldsymbol{\sigma}_{dev}$ and the unit tensor $\mathbb{1}$ are mapped into vectors as usually done in the finite element practice, and $\boldsymbol{B}$ is the typical finite element matrix defining the shape functions derivative.

We implemented this formulation using the C++ templates technique. Only one code was written for all topologies, including linear and quadratic tetrahedron and hexahedron elements. As pointed out by Lindgren [CK92, BPM$^+$95], hexahedral elements are superior to linear tetrahedral elements, and also better than quadratic tetrahedron elements when plastic deformation occurs, and therefore we used $q1 - p0$ hexahedral elements to do the tests.

The discrete equilibrium equations are solved by using a standard Newton-Raphson method. The Jacobian matrix corresponds to that obtained from an equivalent purely

Lagrangian elastoplastic quasi-static incremental problem (see for instance Simo et al. [SH98]).

4.5 Validation of the model

The thermal stress calculated by the finite element model developed in the present work has been compared with the semi- analytical solution developed by Weiner and Boley [WB63] for thermal stresses during one-dimensional solidification of a semi-infinite elastic perfectly plastic body after a sudden decrease in surface temperature.

The thermal problem they solved corresponds to the Neumann's classical one, a phase change 1D problem with uniform initial temperature T_s (solidification temperature) and fixed temperature $T_w < T_s$ on one end, being $T^o = T_s - T_w$ defined as the temperature drop.

They took an elastic-perfectly plastic material model for the mechanical problem, with a constant Young modulus E and yield stress σ_y varying linearly with temperature:

$$\sigma_{y(T)} = \sigma_y^o \frac{T_s - T}{T^o} \qquad ; \qquad T \leq T_s \tag{4.34}$$

where σ_y^o is the yield stress at temperature T^o.

The Neumann's solution introduces a characteristic length $\bar{y} = p\sqrt{t}$, where t denotes time and the parameter p is given by:

$$p = 2\sqrt{K_s}\gamma \quad ; \quad K_s = \frac{\kappa}{\rho C_p} \quad ; \quad \gamma \approx \sqrt{\frac{T^o C_p}{2L}} \qquad (\gamma^2 \ll 1); \tag{4.35}$$

The thermal diffusivity (K_s) is the ratio of conductivity (κ) to density (ρ) and specific heat (C_p), while L is the latent heat.

Weiner et al. introduced also the dimensionless quantities:

$$\hat{y} = \frac{y}{\bar{y}} \qquad ; \qquad \hat{T} = \frac{T - T_s}{T^o}$$

$$\hat{\sigma} = \frac{(1-\nu)\sigma}{\alpha_T E T^o} \quad ; \quad \hat{\sigma_y} = \frac{(1-\nu)\sigma_y}{\alpha_T E T^o} = -m\hat{T} \quad ; \quad m = \frac{(1-\nu)\sigma_y^o}{\alpha_T E T^o}$$

where α_T is the thermal expansion coefficient and ν the Poisson ratio.

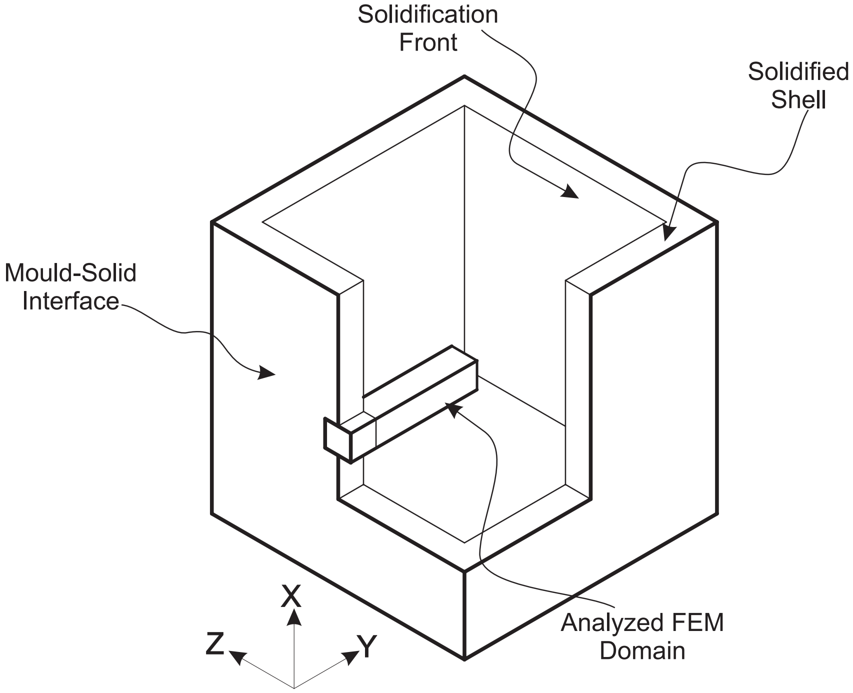

Figure 4.4: Weiner [WB63] problem description.

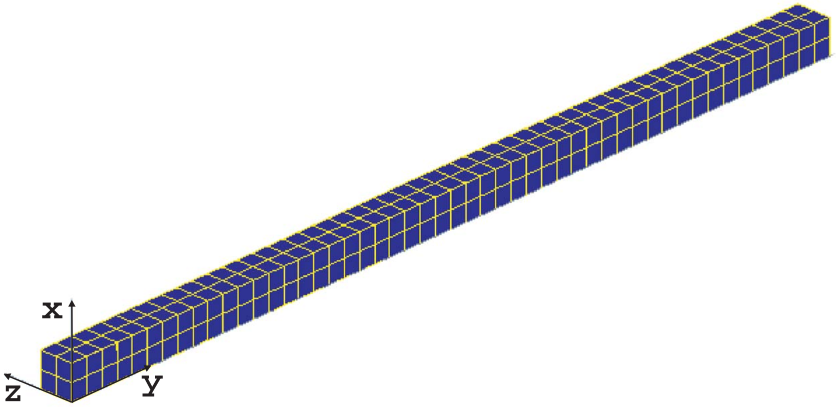

Figure 4.5: Finite element model for the 1-D numerical validation test.

The problem has been solved in a prismatic domain using the finite element procedure described in subsection 4.4, and imposing Extended Plane Strain (EPS) conditions along transversal directions z and x, to be consistent with the original hypothesis proposed by Weiner et al.

The FE mesh consists in hexahedral elements, as shown in Figure 4.5. The EPS conditions ($\varepsilon_x =$ constant $\varepsilon_z =$ constant) are imposed via Lagrange multipliers, constraining all nodal x- and z-displacements to be identical.

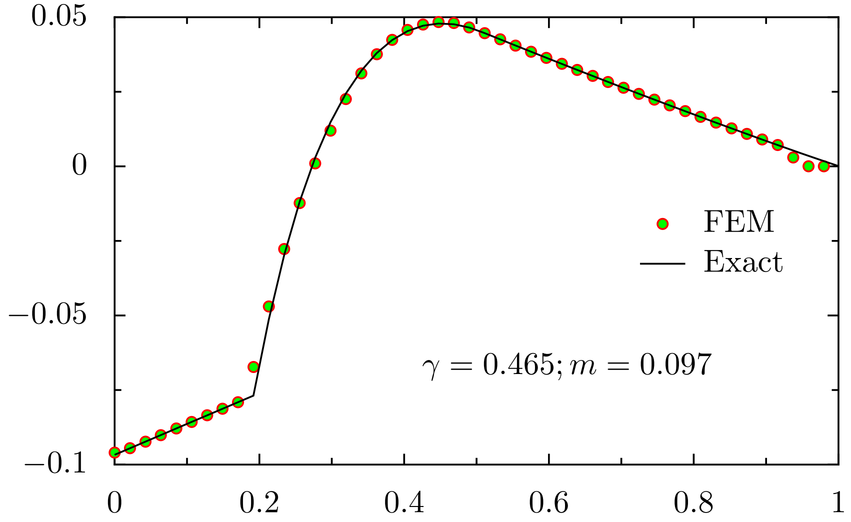

Figure 4.6: Stress distribution along the $\hat{y}$-coordinate. Comparison of semi-analytical [WB63] and numerical solutions.

Figure 4.6 compares the semi-analytical results with the numerical ones. The curves plot the non-dimensional stress component $\hat{\sigma}_{xx}(=\hat{\sigma}_{zz})$ along the non-dimensional $\hat{y}$-line (longitudinal direction) for $m = 0.097$ and $\gamma = 0.465$. The agreement of the numerical FE solution with the semi-analytical one is evident from the figure.

It should be noted that this semi-analytical solution gives a maximum tensile (compressive) stress which is constant in time. This behavior is due to the particular thermal boundary conditions adopted (which correspond to a similarity solution) in the mentioned semi-analytical study.

Chapter 5

Coupling

In this section different couplings between the problems mentioned in the precedent chapters are discussed. For example, simulations that are concerned with the mechanical effects of welding are based on the thermal solution. Also the material behavior, due to the changing microstructure, may depend on the temperature and deformation histories. This requires that one consider the microstructure evolution when modeling the material behavior.

The possible couplings to be considered are:

1. Material properties depending on the phase fractions.
2. Volume change affecting the mechanical stress-strain states depends on phase transformations.
3. Microstructure evolution is based on thermal history.
4. Microstructure evolution affects the thermal field by latent heat and microstructure dependent material properties.
5. Thermal expansion and temperature dependent material properties.
6. Mechanically generated heat.
7. Phase transformations are affected by stress.

The two latter couplings effects are not included in this work and finally the adopted coupling scheme is summarized in Figure 5.1.

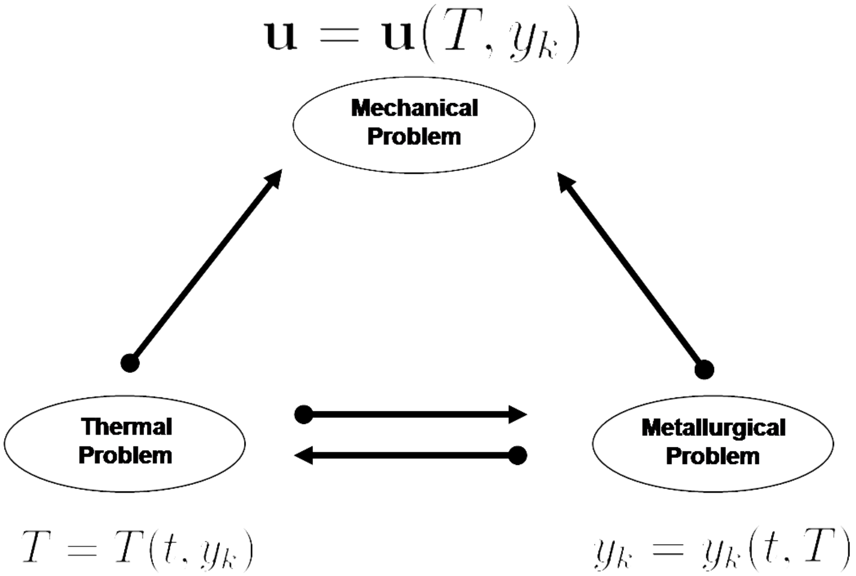

Figure 5.1: Thermo-metallurgical-mechanical coupling

Assuming small relative displacements within the welding portions of the structure, a one way coupled thermal and mechanical analyses can be implemented. Assuring small displacements, the welding electrode and consequently the location of heat flux applied to the model do not change position [BS92].

Oddy et al. [OGM89] state that the heat generated by the plastic deformation is much less than the heat introduced by the weld arc itself. Therefore, the thermal analysis may be performed separately from the mechanical analysis.

Metallurgical transformations are an important aspect in welding simulation [KBJ90, OGM89, OG93, VJC+99, BS92]. The physical and chemical properties of the material also change at the weld site and heat affected zone (HAZ), both during and after the welding process. These changes may result in varying material properties. Metallurgical calculations are included in the analysis to determine the phases fractions in the heat affected zone (HAZ). These transformations have influence in the following factors:

1. The mechanical properties of the HAZ are derived from the mechanical properties of the individual phases.

2. The final residual stress distribution depend on the expansion and contraction of the different phases formed as a result of different temperature dependent properties during transformation. The thermal strains are calculated from the phase and temperature dependent thermal expansion coefficients.

3. During metallurgical transformations the level of plastic deformations decreases because of the movement of dislocations. Each phase of the material has a different strain hardness character.

During phase transformations there is a release or absorption of energy upon solidification or melting known as the latent heat effect. The latent heat effect associated with a solid-solid phase change is much smaller than that associated with a solid-liquid phase change [OGM89].

This study included the latent heats for all the phase transformations: fusion, solidification, austenitic, ferritic, bainitic, and martensitic. Also, the phase dependencies of the heat capacity and conductibility were included.

The metallurgical and thermal calculations are coupled so that at each temperature the phase proportions are calculated. Any material property in the heat balance equation is temperature-dependent and it is assumed to be given by the mixture law described in §3.4 by equation (3.13).

5.1 Solution scheme

Sequentially coupled thermal stress analyses are performed to investigate the temperature history, residual stresses and deformations.

Due to the weak nature of mechanical to thermal field coupling, the non-linear transient analysis is divided in two parts.

First, thermal analysis is performed to predict the temperature history of the whole domain, and then it is applied as input for the subsequent structural analysis.

A fully coupled thermal, metallurgical and mechanical analysis of a single pass weld was made by Inoue and Wang [IW84]. In the present work, a so-called staggered approach was used to couple the thermal and mechanical fields as shown in Fig. 5.2.

The thermal field is first calculated followed by the microstructural evolution and finally the mechanical quantities are determined.

The coupling is organized using a staggered scheme, where for every time step the thermal and metallurgical problem are solved first, and then the mechanical problem is solved using as inputs the previous obtained results, as shown in figure 5.2.

Algorithm 1 shows the global calculation scheme. At the time being, a fixed time step is specified.

Algorithm 1 Staggered Solver

```
while $t < t_{end}$ do
    $t = t + \Delta t$
    $THERMAL\_NEWTON$
    while $\|\boldsymbol{\Psi}_{(\boldsymbol{T}^{(i)})}\| > Tol_{ther}$ do
        Calculate $\Delta\boldsymbol{T}^{(i)} = -[\boldsymbol{J}_{(\boldsymbol{T}^{(i-1)})}]^{-1}\boldsymbol{\Psi}_{(\boldsymbol{T}^{(i-1)})}$
        Compute $\boldsymbol{\Psi}_{(\boldsymbol{T}^{(i)})}$
    end while
    $MECHANICAL\_NEWTON$
    while $\|\boldsymbol{R}_{(\boldsymbol{U}^{(i)})}| > Tol_{mech}$ do
        Calculate $\Delta\boldsymbol{U}^{(i)} = -[\boldsymbol{J}_{(\boldsymbol{U}^{(i-1)})}]^{-1}\boldsymbol{R}_{(\boldsymbol{U}^{(i-1)})}$
        Compute $\boldsymbol{R}_{(\boldsymbol{U}^{(i)})}$
    end while
end while
```

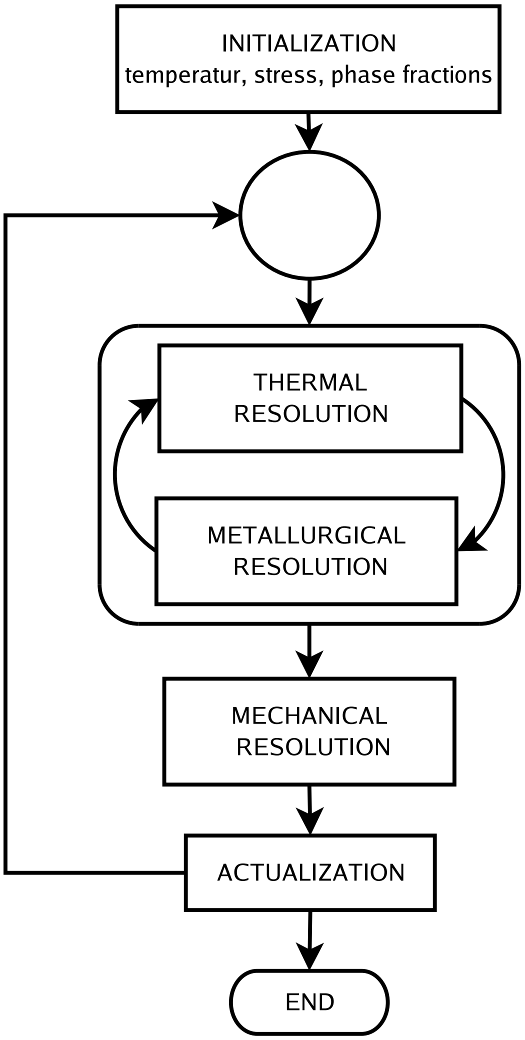

Figure 5.2: Thermo-metallurgical-mechanical solution scheme

Chapter 6

Application Examples

6.1 Residual Stresses in Fusion Welding

Residual stresses associated with thermal welding processes are of particular importance because they are frequently of yield or greater magnitude in the direction of the weld. Fatigue failure of welded structures occurs usually at the weld site, along or adjacent to the weld toe. Residual stresses and strains may also approach yield magnitude in the transverse direction to the weld.

The magnitude of the residual stresses and their distribution depends on numerous factors, including the type of welding, number of passes, material properties and degree of constraint during the process. Material that is rigidly constrained will have greater residual stresses than one that is allowed to distort during the process.

During a thermal welding process, the weld site and immediate surrounding area experience different rates of heating/cooling and thus expansion/contraction and this leads to large thermal strains. Due to the heat application localised nature, the expansion due to these strains is constrained by the cooler material away from the site of the applied heat.

A stress parallel to the direction of the weld bead is called longitudinal residual stress, denoted by the letter σ_z. The longitudinal residual stress arises due to longitudinal expansion and contraction during welding. Along the weld line, a high tensile residual stress arises near the weld toes, and then decreases to zero, finally becoming compressive, as distance from the weld line on the flange increases.

A stress normal to the direction of the weld bead is known as a transverse residual stress, denoted by the letter σ_x. A tensile residual stress is produced at the surface of the specimen near the weld and decreasing close to zero as the distance from the weld toes increases.

Figure 6.1 depicts the formation of residual stresses and their typical distribution in a butt-welded plate:

Figure (a) shows the weld immediately upon completion, with both the weld site and the region adjacent to this being at the same high temperature and of equal length whilst the remaining plate is at a lower temperature.

Figure (b) illustrates what the outcome if the three elements were separated and allowed to cool. The plates would remain their original length, whilst the weld would contract on cooling.

Figure (c) represents the stresses that would develop on cooling of the plates and weld. The contraction of the weld is resisted by the parent material and thus experiences a tensile stress along its length, while the parent plate, in resisting the contraction of the weld, is subject to a compressive stress.

Figures (d), (e) and (f) portray the typical residual stress distribution longitudinal to, transverse to and through the thickness of the weld respectively. The weld bead also contracts across its width and depth, resulting in the tensile residual stress fields at the surface, which are at right angles to the weld direction and occur in both the through-thickness and transverse planes.

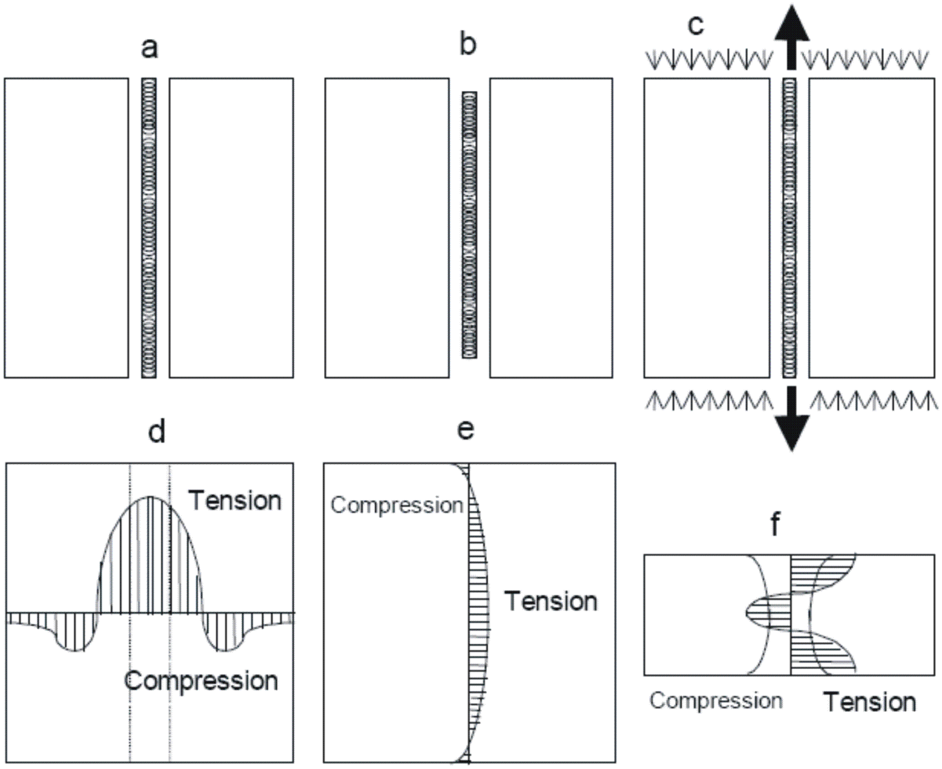

Figure 6.1: Typical residual stresses distribution (Gurney, TR (1979) and Parlane, AJA (1981))

6.2 Numerical Examples

6.2.1 Butt-welded Strip

In this section, we analyze the strain-stress field in a butt welded joint between strips of 0.3%C carbon steel.

Figure 6.2 depicts the geometry and the finite element mesh. The x, y and z directions represent the length L , width W and thickness H of the strip.

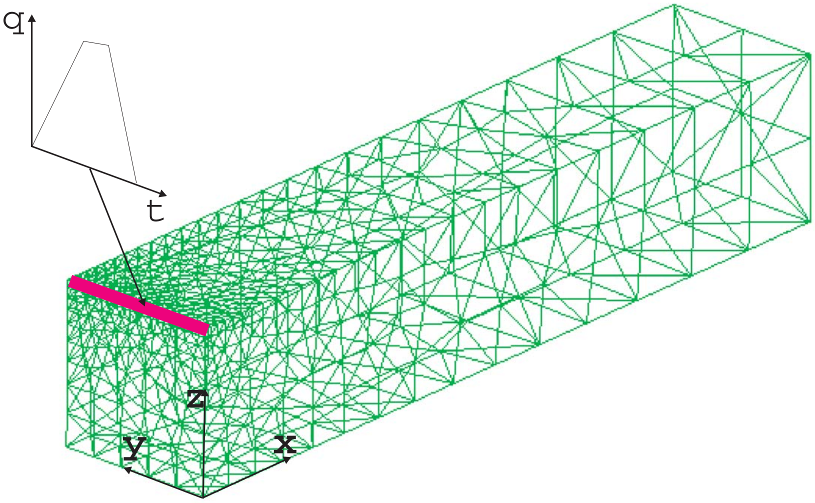

Figure 6.2: Butt-welded joint. Geometry and FEM mesh

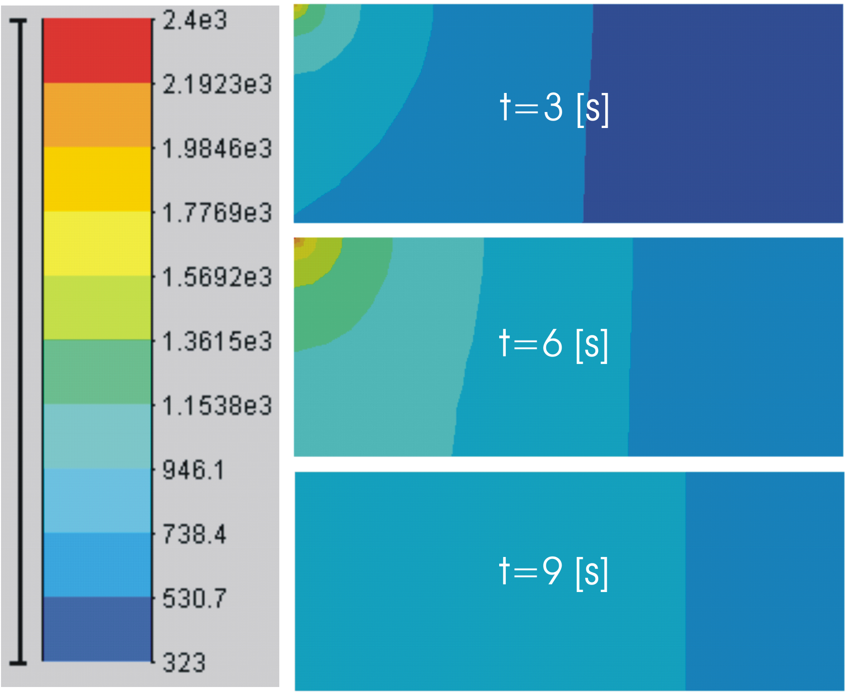

Figure 6.3: Butt-welded joint. Temperature distribution

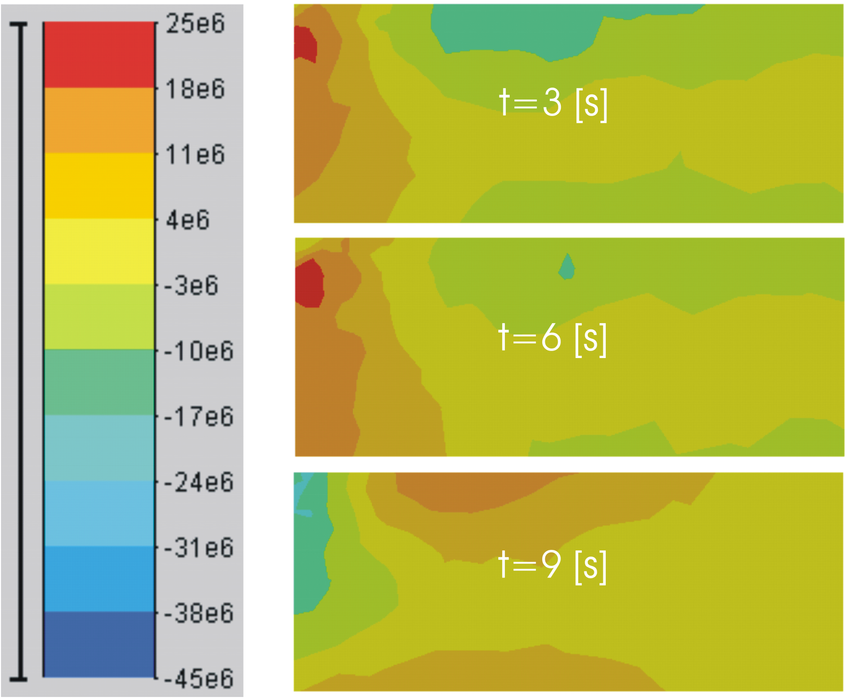

Figure 6.4: Butt-welded joint. σ_x stress distribution

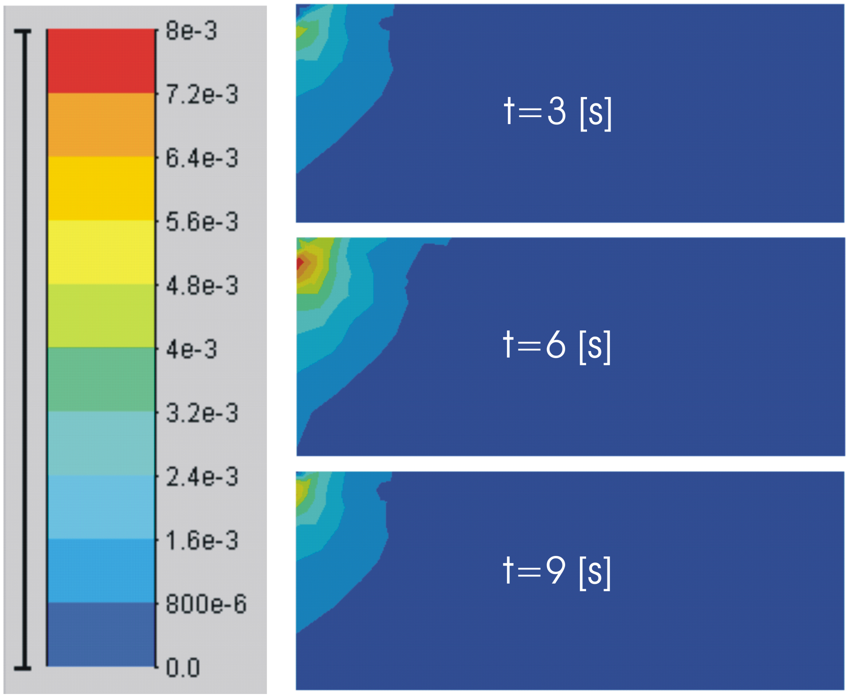

Figure 6.5: Butt-welded joint. Equivalent plastic strain distribution

In the thermal analysis the domain was discretized with linear tetrahedrons. The mesh was refined in the HAZ, and was coarsened gradually farther along the longitudinal direction.

The welding speed was assumed to be infinite. An external heat input is imposed in the edge marked in the figure 6.2. Initial temperature was defined at $To = 373\ K$, and all faces were defined as adiabatic boundaries, except at $x = L$ where the temperature was fixed to $T_w = 373\ K$.

The mechanical boundary conditions were $u_z(0, y, 0) = 0, u_y(0, 0, 0) = 0, u_x(0, y, z) = 0$, assuming a symmetry condition in $x = 0$.

Figure 6.3 shows the temperature distribution, obtained with the thermal model previously developed in Chapter 2. The σ_x stress field is plotted in figure 6.4. Even when geometry and material properties were different, the distribution of tensile and compressive stresses compares well with several case studies published in the literature [YJMX04].

Finally the equivalent plastic strain is shown in figure 6.5.

6.2.2 Butt-welded Plates

In this example a butt-welded plate is presented with length, width and thickness respectively equal to $L = 500mm$, $W = 500mm$, $th = 6mm$. A 3-dimensional symmetrical model was used to estimate the residual stresses of the butt-welded joint using the finite element method.

The material properties used in the model correspond to a CMn steel. The plate is clamped in the corners opposite at the site to the welded line. Natural convection from the top and bottom of the plate is assumed with a heat transfer coefficient of 45 $[W/mm2]$.

The welding parameters are summarized in table 6.1 and 6.2.

Arc Parameter	Symbol	Value	Unit
Current	I	250	A
Voltage	U	23	V
Efficiency	η	0.825	–
Total Heat	Q	4743.75	W
Speed	v	4.8	mm/s

Table 6.1: Arc parameters

Goldak Parameter	Value	Unit
a	5	mm
b	3	mm
cf	5	mm
cr	10	mm
ff	0.6	–
fr	1.4	–

Table 6.2: Goldak's Parameters

The symmetric model has 3750 elements and 6000 nodes after meshing.

Simulation results

The process takes about 100 s to complete the weld. After extinguishing the arc, cooling of the weldment takes about 35 min to return to the ambient temperature. The time stepping has a minimum time step of 0.5 s during welding. The complete analysis has taken about 14 hs of CPU.

The temperature results (Figure 6.6) shows that because of the locally concentrated heat source, the temperature near the weld bead and heat-affected zone rapidly changes with the distance from the centre of the heat source. Therefore, the highest temperature is limited to the domain of the heat source.

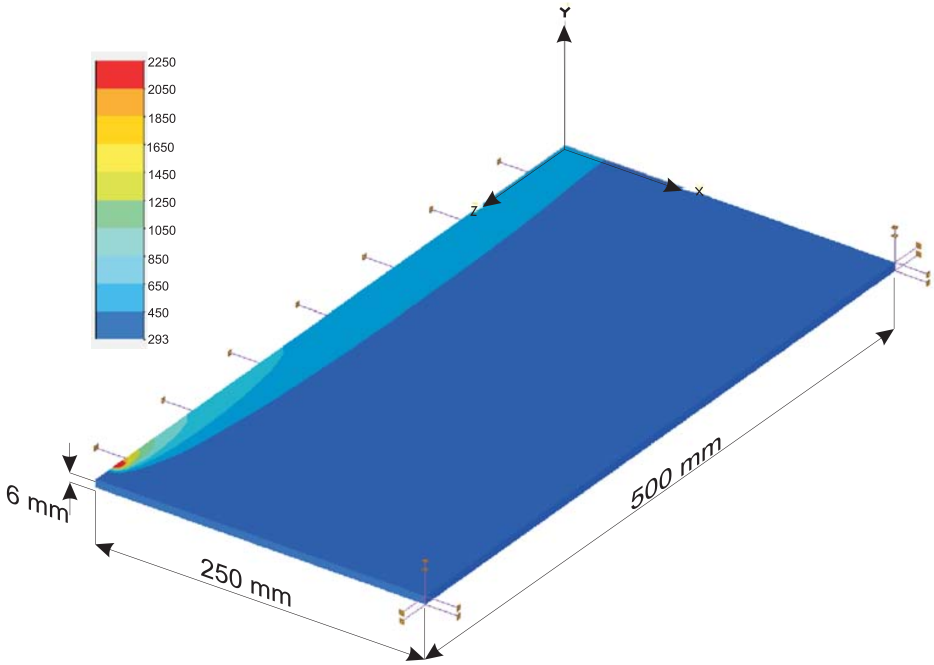

Figure 6.6: Temperature field $[K]$ at time $t = 100s$.

Figure 6.7 depicts the out of plane displacement of the plate along the transverse direction. As expected the plate shows a bending pattern.

Related to the residual stresses, Figures 6.8 and 6.9 show calculated longitudinal (σ_z) and transverse (σ_x) stresses. The behaviour is analogous to that found in the literature. As expected the maximum residual stress is produced near the heat affected zone. The longitudinal normal component of stress is in the order of the yield stress.

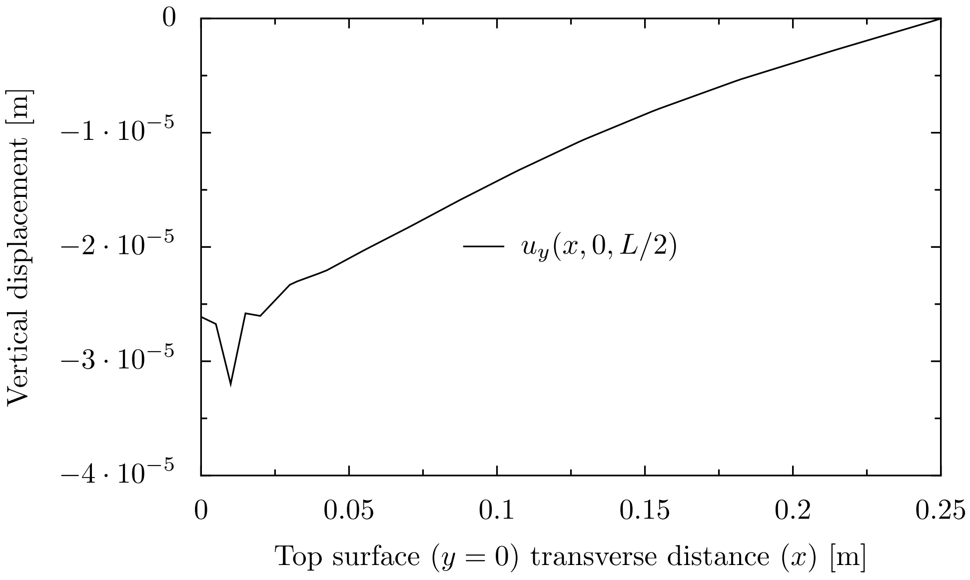

Figure 6.7: Transverse out-off plane displacement at time $t = 300s$.

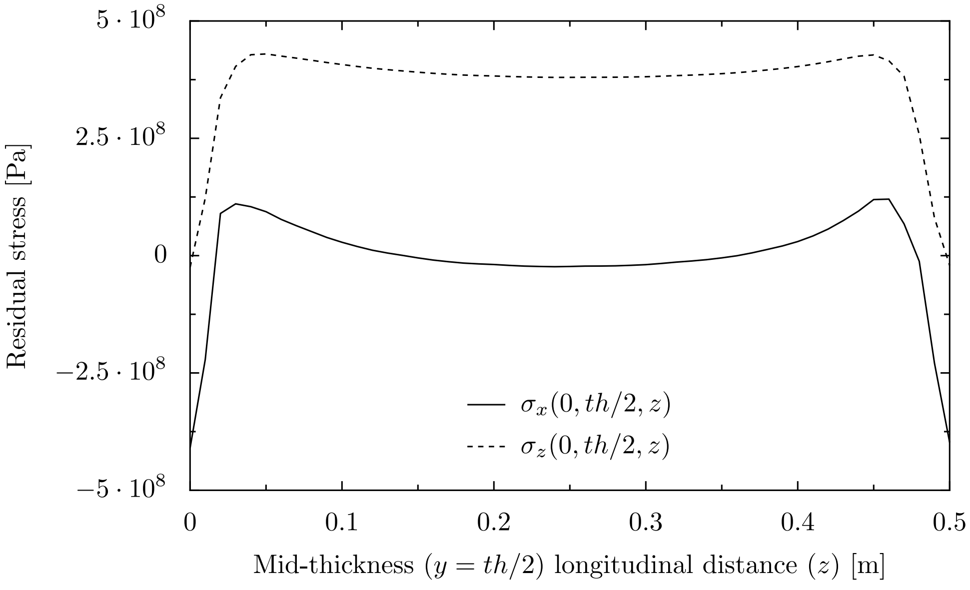

Figure 6.8: Longitudinal residual stress distribution at $t = 300s$.

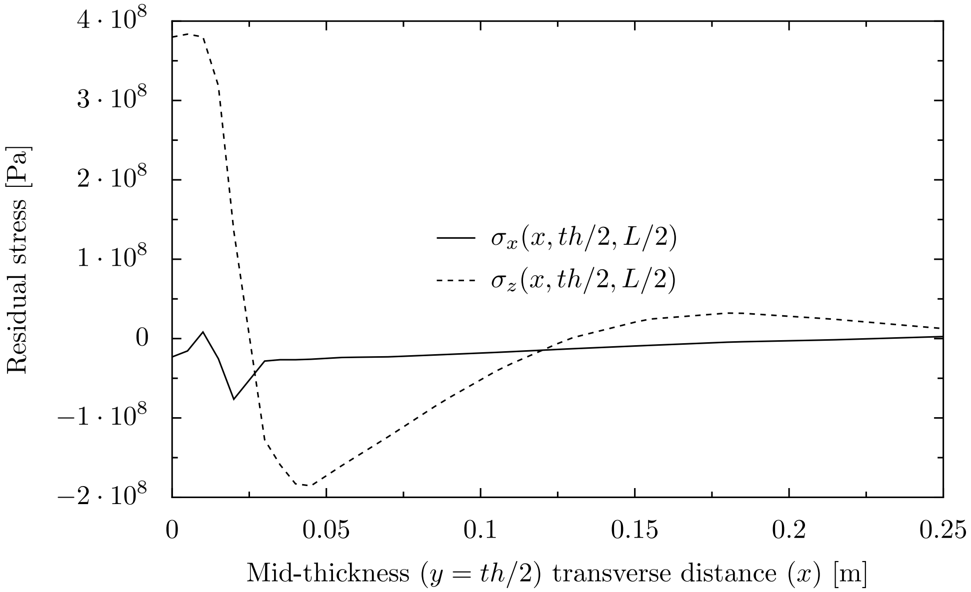

Figure 6.9: Transverse residual stress distribution at $t = 300s$.

6.3 Stress and strain evolution during heat treatment of work rolls

Heat treatment of metallic alloys is a complex thermomechanical process involving solid state metallurgical transformations that change both the thermal and the mechanical properties of materials. This process is widely used in industrial applications to release internal stresses, reduce fragility, improve machinability or modify properties like hardness or strength to satisfy the requirements of a definite application. However, heat treatment can cause undesirable strains and stresses, and also cracking of parts. This fact must be taken into account when designing the heating and cooling sequence in the process. Numerical simulation of heat treatment has been the subject of much research work, which focuses either on thermal and mechanical analysis of the process [BGB98, AM98, SGV98, Ber01], or on aspects of material modeling [KTB78, Höm96, Alb03, SZGMS03]. Material models with the ability to account for variations in thermal and mechanical properties due to temperature and metallurgical structure changes are a key point to simulate accurately the thermomechanical evolution of parts subjected to heat treatment. Several models describe material properties as functions of alloy composition, temperature and microstructure. Other models describe the evolution of microstructure as a function of alloy composition and cooling time, reproducing isothermal (TTT) or continuous cooling (CCT) diagrams for different alloys and chemical compositions. Material models developed to describe phase transformations and properties of metals during heat treatment analytically [JM39, Lem59, KM59, LDD89, Leb89, LJ97] are very useful to cover a broad range of chemical compositions for some well-known alloys (carbon and low-alloy steels, austenitic stainless steels, etc.), but their effectiveness for special alloys (e.g. for high-alloy white iron) is very limited because of the difficulty to obtain all the coefficients needed to represent accurately their behavior [Tal02]. In this work, we take an alternative way to simulate heat treatment. We use material properties defined as functions of time and temperature, which were obtained by merging TTT/CCT diagrams with curves of dependency of thermomechanical properties in terms of temperature and metallurgical composition. Simulations were done using a finite element software [S.A04].

6.3.1 Numerical model

6.3.2 Thermomechanical model

Numerical analysis of heat treatment processes can be made by modeling the time evolution of two coupled problems:

- A thermal problem which involves heating and cooling of parts and must take into account the variations of material properties (thermal conductivity and enthalpy) due to temperature and microstructural transformations, and also heat releasing/absorption (related to latent heat) during metallurgical transformations.

- A mechanical problem to predict stresses and strains generated by thermal expansion/contraction produced by temperature changes and also by metallurgical phase transformations.

The thermal problem is non-linear because thermal parameters are dependent on temperature. The mechanical problem is also non-linear because thermal and transformation-induced strains often generate plastic deformations. In the absence of very strong mechanical perturbations that could induce metallurgical transformations (e.g. transformation of retained austenite to martensite, induced by stresses generated by external loads), mechanical phenomena do not affect thermal properties. This fact releases the dependency of the thermal model on the mechanical variables, and enables us to perform an uncoupled thermal analysis followed by a mechanical analysis that takes the thermal results as inputs.

The dependence of the thermal problem on metallurgical transformations is simulated with an enthalpy model that takes into account heat capacity of metal, and latent heat exchange occurring during phase changes. The dependence of the mechanical properties on material microstructure, is simulated using material models that account for variations in metallurgical constituents with time. The thermal dependence of the mechanical problem is modeled using a thermal field calculated in the thermal simulation, and given as input, to evaluate the mechanical properties for the mechanical analysis and to compute the strains.

In the mechanical simulation, we use a elastoplastic model in which the stresses are calculated as

$$\boldsymbol{\sigma} = C(T, \epsilon_p, m)\boldsymbol{\varepsilon}^e = C(T, \epsilon_p, m)(\boldsymbol{\varepsilon} - \boldsymbol{\varepsilon}^i - \boldsymbol{\varepsilon}^{T-M}) \tag{6.1}$$

where $\boldsymbol{\sigma}$ and $\boldsymbol{\epsilon}$ are the stress and strain tensors, C is the constitutive tensor, $\boldsymbol{\epsilon}_e$ is the elastic strain, $\boldsymbol{\varepsilon}^i$ is the plastic strain and $\boldsymbol{\varepsilon}^{T-M}$ is the thermal-microstructural strain, which integrates the effect of thermal expansion and volume variations during metallurgical phase changes. The stress field must satisfy the Von Mises yield criterion with isotropic hardening. Since the limit stress σ_y is a function of the equivalent plastic strain (α) and temperature, the model can take into account the variation in material hardening behavior with temperature.

6.3.3 Material model

Most material properties are functions of temperature and microstructure, and therefore they have indirect dependency on variables defining material microstructure, like time and maximum heating/cooling temperature. In austenizing processes (heating), the microstructure is modeled as a function of temperature only. In quenching processes (cooling), the microstructure is a function of temperature and time. In tempering processes (heating and cooling) the microstructure is considered as a function of temperature only (dependency upon temperature and time could be modeled if data about transformations of retained austenite were available). Then, for the whole process, we can formulate any general property μ, as a function of temperature and time, as

$$\mu = \mu(T, m(T, t))) = \mu(T, t). \tag{6.2}$$

To define the material parameters, we first construct a map of microstructure as a function of temperature and time, using data about heating and cooling periods, and isothermal (TTT) or continuous cooling (CCT) diagrams for the quenching cooling interval, as shown

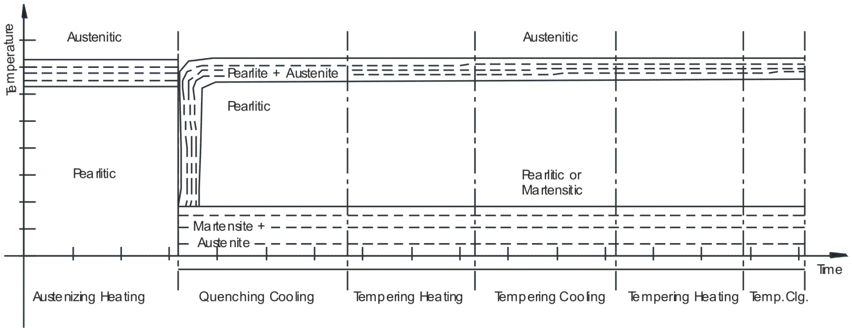

Figure 6.10: Temperature – Time – Transformation approximation.

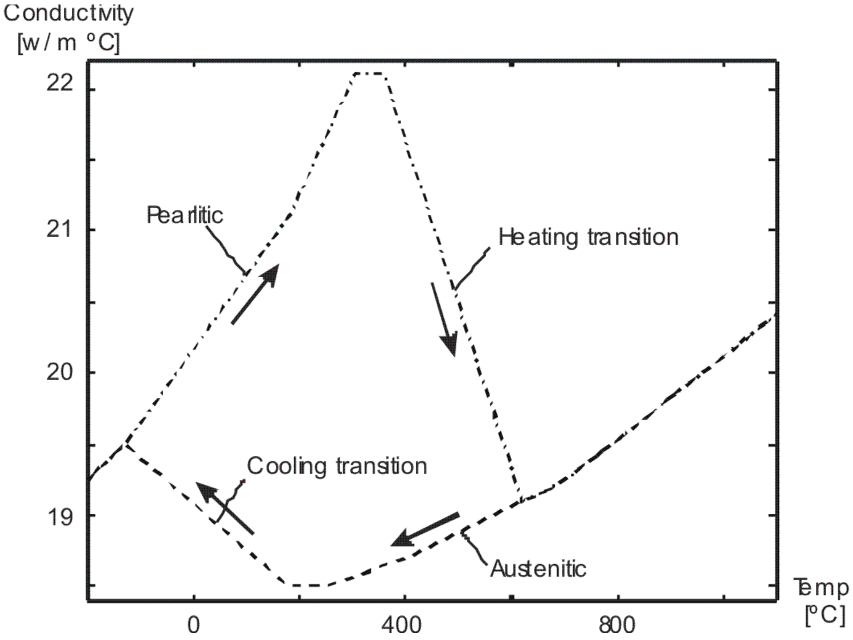

Figure 6.11: Conductivity vs. temperature approximation.

in Figure 6.10.

Then, for every definite material microstructure (i.e.: austenitic, pearlitic, martensitic), we define the value of every property as a function of temperature. Figure 6.11 is an example for conductivity. Finally, by combining the map of microstructure as a function of temperature and time with the curves of temperature dependence of the considered property, and by using the rule of mixtures for regions with mixed structure (e.g. austenite + pearlite), a map of the property as a function of temperature and time (continuous piecewise linear approximation) can be built, as shown in Figure 6.12.

In the finite element procedure, we have used material properties that depends on temperature, as was described in the precedent paragraphs. Using such standard material model, special care must be taken to adapt the map of microstructure as a function of temperature and time to the real quenching cooling process, thus avoiding reversions in austenite-pearlite and austenite-martensite transformations. In the thermal analysis,

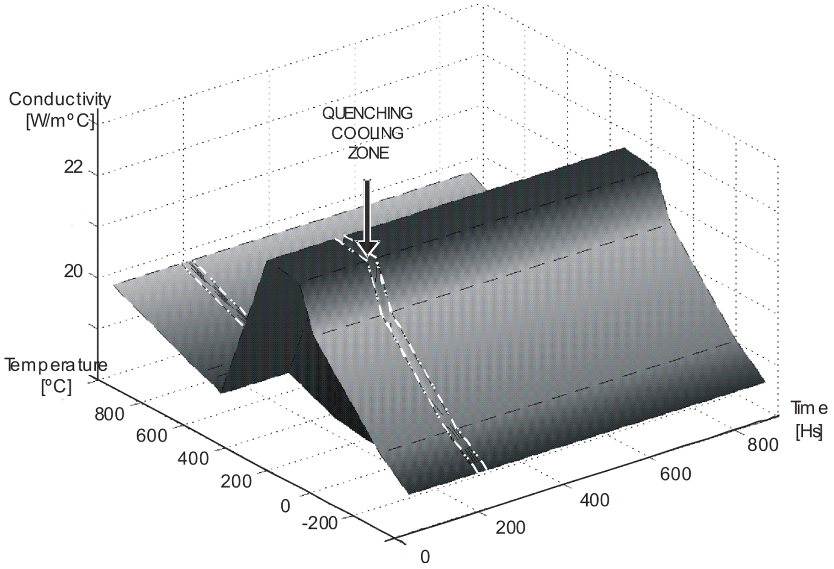

Figure 6.12: Conductivity vs. temperature and time diagram.

the material parameters are the enthalpy and the thermal conductivity. In the mechanical analysis, the material parameters are the Young's modulus, the Poisson's ratio, the thermal-metallurgical expansion coefficient, and the yield stress. All of them are modeled following the above mentioned procedure to account for variations during the heat treatment process.

6.3.4 Application case

Problem description

The Hi-Chrome work rolls used in the initial stages of steel lamination have an exterior layer (shell) of Hi-Chrome white iron, an intermediate layer of low-alloy iron, and a core of spheroidal graphite iron. The first two layers are centrifugally casted, and then the core is poured statically. Typical as-cast dimensions are shown in Figure 6.14. After casting the rolls, they are heated to 1020^oC (with complete austenitization). Then, they are quenched cooled in air to room temperature. Finally, they are subjected to two tempering processes at 480^oC and 540^oC with air cooling to room temperature. After the heat treatment, some rolls have shown cracks near the corners of the barrel. In all cases the cracks has conic shape, starting at the end of the barrel in the vicinity of the interface between Hi-Chrome and interface layers, and ending at the external diameter of the barrel, approximately 250 mm away from the barrel's edge, as shown in Figure 6.15.

Even though, circumferential cracks in the external diameter of the roll were observed several hours after the end of the second tempering, when rolls reached ambient temperature; the presence of black ferrous oxides in the initial zone of the cracks, indicated that the cracking started in an intermediate stage of the heat treatment (at least previously to the last tempering heating). The aim of this analysis is to determine instant when cracking was supposed to start, and to confirm the presence of residual stresses, which may

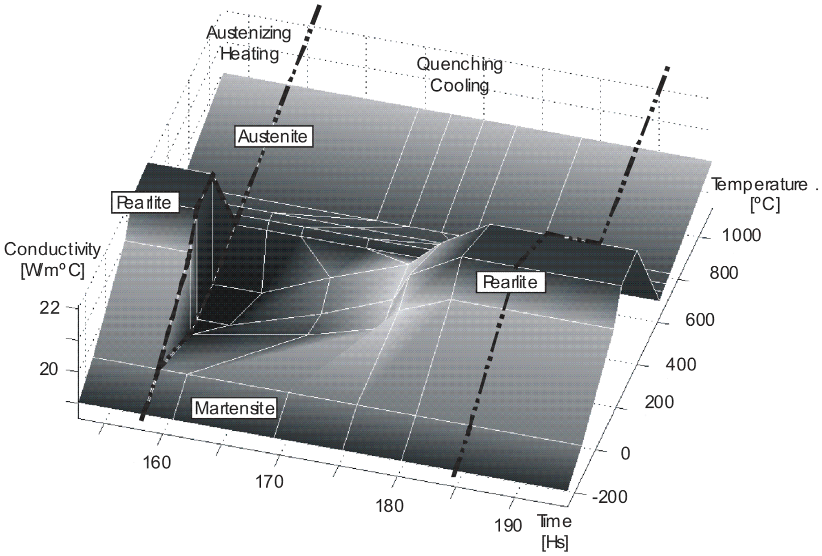

Figure 6.13: Conductivity vs. time and temperature diagram Ű Detail in the quenching cooling zone

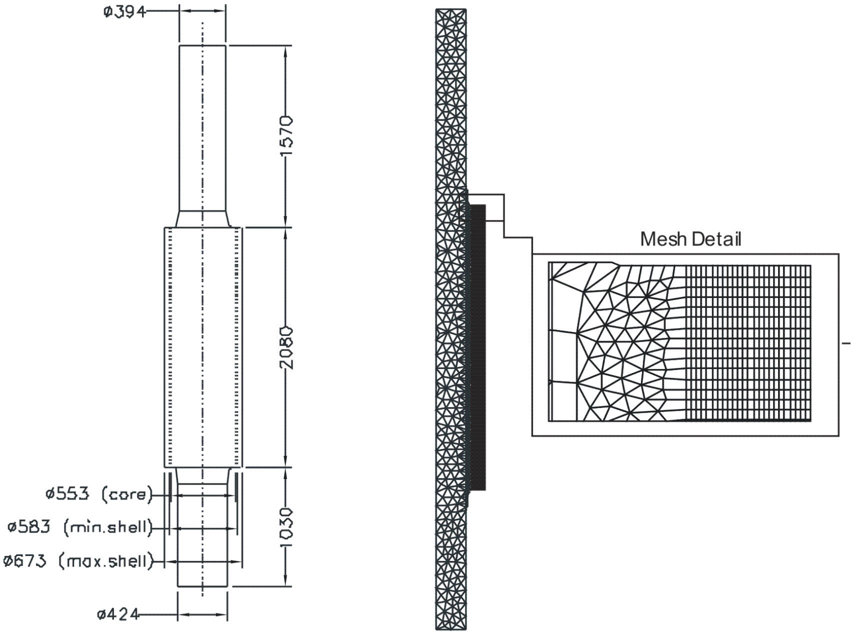

Figure 6.14: a) Work roll general dimensions. b) FEM Mesh .

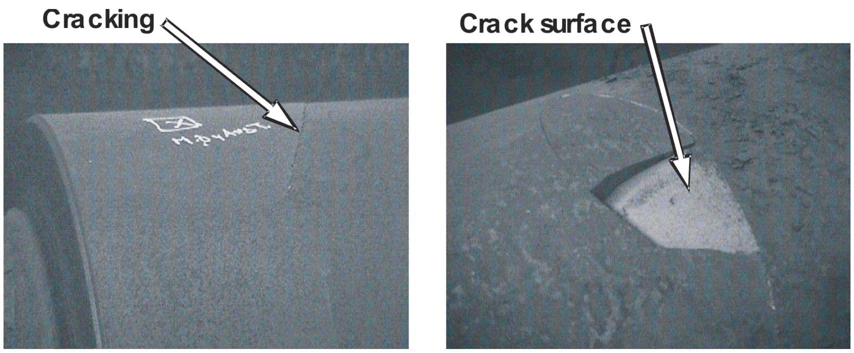

Figure 6.15: Cracks in the barrel of work rolls.

explain the advancement of the cracking. By ignoring small circumferential temperature differences and small bending stresses generated by the horizontal mounting of cylinders in the heater, the problem can be modeled assumin axial symmetry conditions. The finite element mesh is shown in Figure 6.14b. Convective boundary conditions were imposed on the external surface of the roll. Convection coefficients ranging from $5[W/(m^2{}^oC]$ to $40[W/(m^2{}^oC]$ were used in the different stages of heating and cooling, depending on the agitation of surrounding air.

Shell material data (Hi-Chrome white cast iron)

The TTT diagram of a similar alloy was used to determine the position of the pearlitic nose [Bet04]. The cooling behavior of the shell material was determined using data of Hi-Cr white iron without Ni [GD03], with a correction of the transformation time to take into account the influence of Ni and Mo as suggested by Laird et al.[LGR96]. The diagram is shown in Figure 6.16.

The thermal conductivity, as a function of temperature and microstructure was taken from data for High-Alloy white iron [17,20]. Enthalpy values were calculated integrating the effective thermal capacity data [Bet04, Ste95] along the temperature range covered in the process.

In order to calculate thermal-metallurgical strains, a secant expansion coefficient averaged from values found in bibliography [GD03, Ste95], and based on a reference state of pearlitic structure at 20^oC, was used. The elastic modulus as a function of temperature and chemical composition was obtained from data published by Belyakova et al. [LGR96, Bel75]. The Poisson's ratio was assumed constant and equal to 0.28. Since data on the temperature dependent yield stress has not been found, we assumed a variation based on the room temperature yield stress with the thermal dependency of the ultimate tensile stress for Hi-Cr white iron [LGR96]. An isotropic hardening law was used.

6.3.5 Layer and core material data (Gray and spheroidal graphite cast iron)

Since the transformation curves of gray and spheroidal graphite (SG) cast iron are similar, the strategy used to determine their material parameters was the same for both.

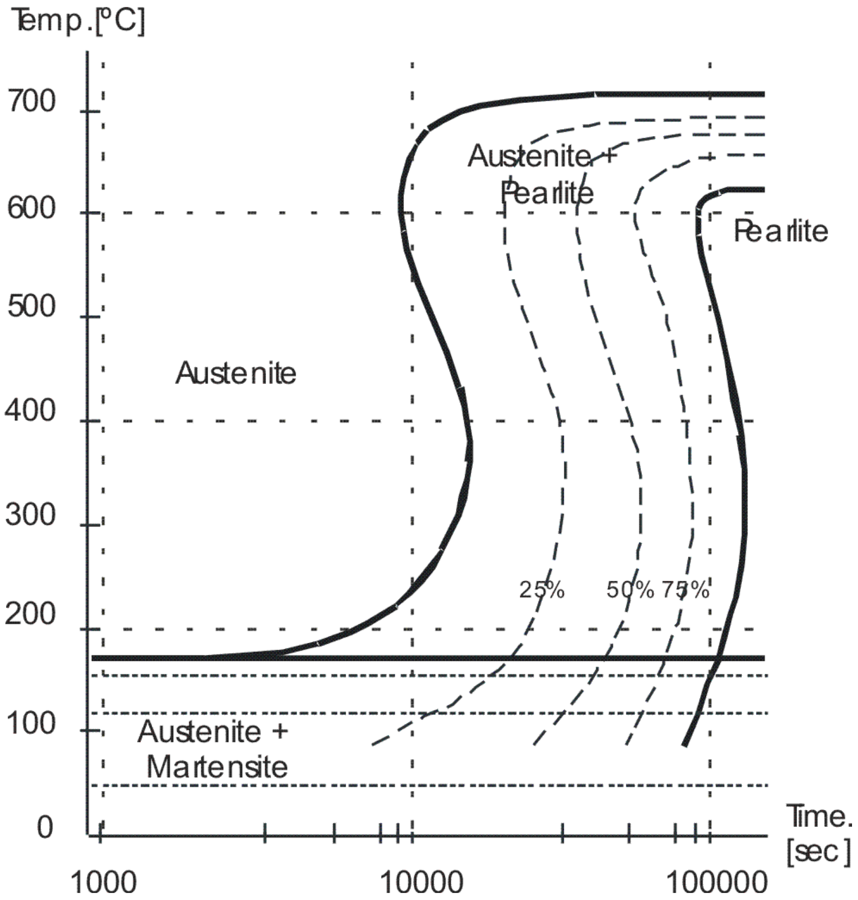

Figure 6.16: Temperature Time – Transformation diagram for Hi-Cr iron (shell).

Temperature $[C]$	Enthalpy $[J/kg]$	Conductivity $[W/(mC)]$	Young modulus $[Pa]$	Secant thermal-metall. expansion coefficient $[1/C]$
180	0.62E5	18.50	2.07E11	-2.60E-5
250	1.06E5	18.50	2.04E11	-1.00E-5
400	2.11E5	18.60	1.95E11	0.23E-5
620	3.87E5	19.00	1.74E11	0.95E-5
650	4.11E5	19.07	1.69E11	1.01E-5
680	4.40E5	19.12	1.65E11	1.07E-5
720	5.25E5	19.20	1.62E11	1.13E-5
1030	7.91E5	20.00	0.75E11	1.90E-5

Table 6.3: Properties for Hi-Cr iron (shell) in austenitic state.

Temperature [C]	Enthalpy [J/kg]	Conductivity [$W/(mC)$]	Young modulus [Pa]	Secant thermal-metall. expansion coefficient [$1/C$]
-130	0.0	19.00	2.18E11	0.80E-5
180	1.07E6	19.50	2.12E11	0.88E-5
250	1.51E6	21.10	2.09E11	0.98E-5
400	2.56E5	22.00	2.00E11	1.18E-5
620	4.32E5	22.10	1.79E11	1.30E-5

Table 6.4: Properties for Hi-Cr iron (shell) in pearlitic-bainitic state

Temperature [C]	Yield stress (austenitic) [Pa]	Yield stress (pearl./bain.) [Pa]
0	–	8.00E+8
100	–	7.00E+8
300	4.30E+8	5.00E+8
620	2.40E+8	2.60E+8
650	2.20E+8	–
680	1.90E+8	–
720	1.60E+8	–
1030	0.40E+8	–

Table 6.5: Yield stress for Hi-Cr iron (shell).

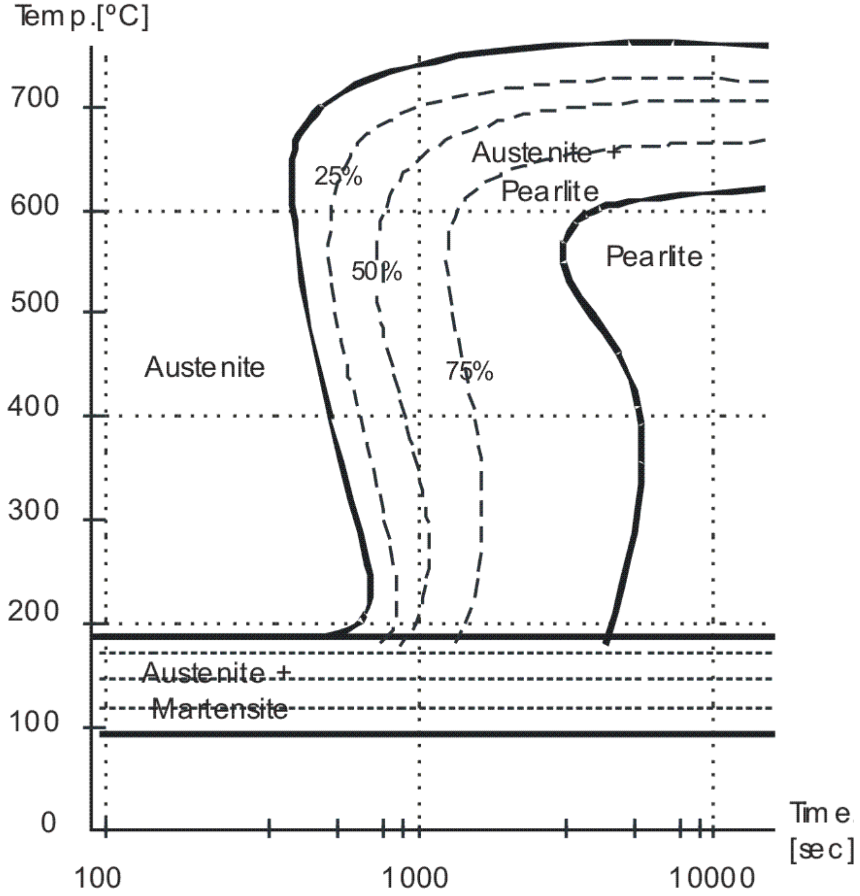

Figure 6.17: Temperature Time – Transformation diagram for SG iron (core).

After determining the microstructure as a function of time and temperature, appropriate parameter values were selected. A TTT diagram for Ni-Mo ductile iron [Boy77] was used to define the microstructure as a function of time and temperature in quenching. This diagram is shown in Figure 6.17.

The thermal conductivity and enthalpy (obtained integrating apparent thermal capacity) as a function of heating and cooling temperature was taken from data published by Auburn University researchers [Wan01].

To compute thermal-metallurgical strains, a secant expansion coefficient based on a reference state of pearlitic structure at 20^oC was calculated from tables of dilatometry in heating and cooling published by the Auburn Solidification Design Center [Wan01]. The elastic modulus as a function of temperature was extrapolated from values at room temperature [Bet04] and thermal dependency of this parameter for pearlitic steels. The Poisson's ratio was assumed constant and equal to 0.26. The temperature dependent yield stress was taken from tables for gray and spheroidal graphite iron of similar composition [Lyn75].

Temperature $[C]$	Enthalpy $[J/kg]$	Conductivity $[W/(mC)]$	Young modulus $[Pa]$	Secant thermal-metall. expansion coefficient $[1/C]$
190	0.28E5	29.80	1.12E+11	-2.10E-5
400	1.40E5	31.00	1.06E+11	0.26E-5
600	2.85E5	31.80	0.97E+11	0.94E-5
650	3.31E5	32.00	0.95E+11	1.01E-5
675	3.59E5	32.10	0.94E+11	1.07E-5
700	4.30E5	32.20	0.92E+11	1.10E-5
750	5.52E5	32.50	0.89E+11	1.17E-5
1030	8.01E5	37.00	0.44E+11	1.95E-5

Table 6.6: Properties for gray iron (layer) in austenitic state.

Temperature $[C]$	Enthalpy $[J/kg]$	Conductivity $[W/(mC)]$	Young modulus $[Pa]$	Secant thermal-metall. expansion coefficient $[1/C]$
0	0.0	42.50	1.22E+11	1.22E-5
190	0.91E5	42.90	1.18E+11	1.28E-5
400	2.08E5	39.90	1.12E+11	1.35E-5
600	3.48E5	37.10	1.04E+11	1.39E-5
650	3.89E5	36.25	1.01E+11	1.42E-5

Table 6.7: Properties for gray iron (layer) in pearlitic-bainitic state.

Temperature $[C]$	Enthalpy $[J/kg]$	Conductivity $[W/(mC)]$	Young modulus $[Pa]$	Secant thermal-metall. expansion coefficient $[1/C]$
190	0.28E5	18.00	1.51E11	-1.90E-5
400	1.43E5	18.20	1.43E11	0.23E-5
600	2.91E5	18.60	1.32E11	0.91E-5
650	3.36E5	18.70	1.29E11	1.01E-5
675	3.65E5	18.75	1.27E11	1.06E-5
700	4.36E5	18.80	1.25E11	1.10E-5
750	5.57E5	18.95	1.20E11	1.17E-5
1030	8.05E5	20.00	0.60E11	1.95E-5

Table 6.8: Properties for SG iron (core) in austenitic state.

Temperature $[C]$	Enthalpy $[J/kg]$	Conductivity $[W/(mC)]$	Young modulus $[Pa]$	Secant thermal-metall. expansion coefficient $[1/C]$
0	0.0	39.00	1.65E11	1.06E-5
190	0.93E5	36.65	1.59E11	1.15E-5
400	2.12E5	29.85	1.51E11	1.30E-5
600	3.60E5	25.49	1.40E11	1.36E-5
650	4.04E5	25.00	1.36E11	1.38E-5

Table 6.9: Properties for SG Iron (core) in pearlitic-bainitic state.

Temperature $[C]$	Layer (austenitic) Yield stress $[Pa]$	Layer (pearl./bain.) Yield stress $[Pa]$	Core (austenitic) Yield stress $[Pa]$	Core (pearl./bain.) Yield stress $[Pa]$
0	–	6.60E+8	–	7.00E+8
100	–	6.20E+8	–	6.50E+8
300	4.30E+8	4.50E+8	4.50E+8	4.80E+8
620	1.60E+8	1.70E+8	1.80E+8	1.90E+8
650	1.50E+8	–	1.70E+8	–
680	1.30E+8	–	1.45E+8	–
720	0.97E+8	–	1.10E+8	–
1030	0.18E+8	–	0.20E+8	–

Table 6.10: Yield stress for gray iron and SG iron (layer and core).

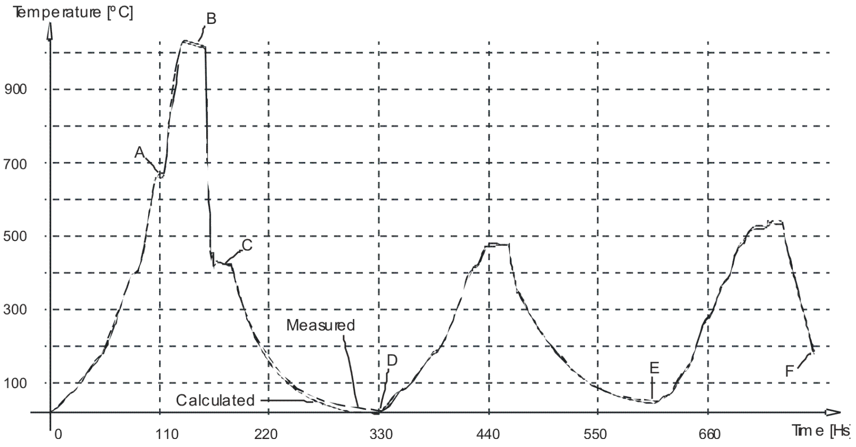

Figure 6.18: Comparison between calculated and measured temperatures in barrel midpoint.

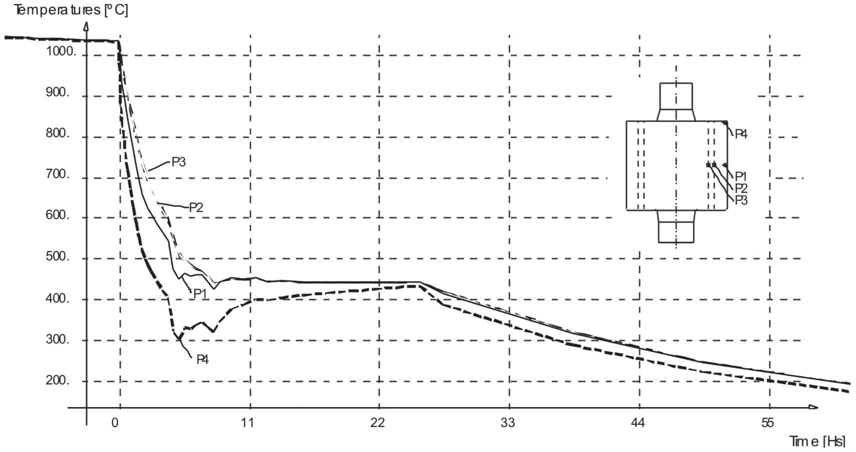

Figure 6.19: Temperature evolution in quenching cooling

6.3.6 Results

In Figure 6.18, a comparison between calculated (continuous line) and measured (dashed line) temperatures at the midpoint of the barrel surface is shown. The agreement between curves has been found to be acceptable the purposes of the analysis.

In order to determine the maximum temperature gradients during the process, the largest differences between temperatures in different points of the roll are found at the initial stage of quenching cooling. Figure 6.19 shows a detail of the differences between points located in the surface of the barrel (P1, P4) and other points situated in the zones of transition between layers of different materials (P2, P3). Even in the worst situation of quenching cooling, the difference between the surface and the core of the roll is lower than 300^oC. In figures 6.18 to 6.26, the evolution of temperatures, principal stresses and equivalent plastic deformations near the corner are shown. The time instants of these plots along the complete heat treatment are referred by letters (A) to (F) in Figure 6.18.

Temperature plots show very small differences between temperatures in different sec-

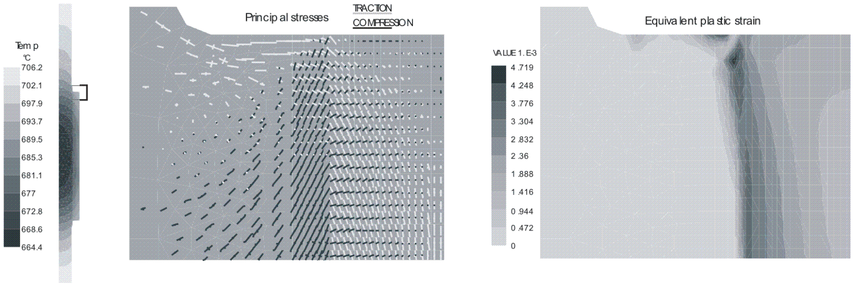

Figure 6.20: Intermediate point (A) of austenizing heating (110 hs)

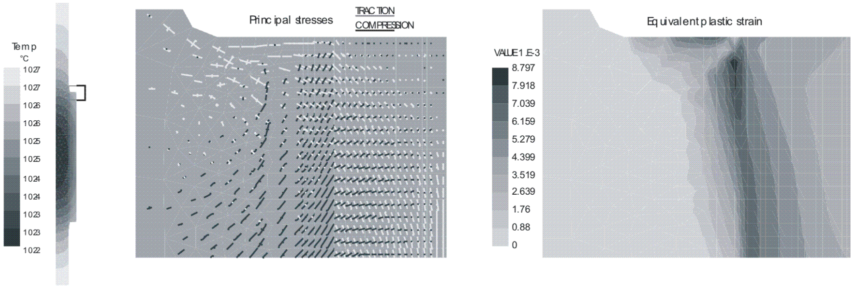

Figure 6.21: End (B) of austenizing heating (156 hs)

tors of the roll during heating processes. Even during cooling processes with very high variations in time, the maximum temperature differences at a given time instant are below 200^oC. The computed temperature space gradients (radial) were also relatively small.

During the austenizing heating, axial stresses in the shell are tensile stresses. However, as plastic deformations occur during heating, in the quenching cooling and in the tempering processes axial stresses in the shell are compressive. Moreover, at the end of the process, residual compressive stresses have enough magnitude to justify the advance of the previously formed crack front up to the external diameter of the barrel.

Figure 6.26 shows the evolution of equivalent plastic strains in different points near the barrel corner.

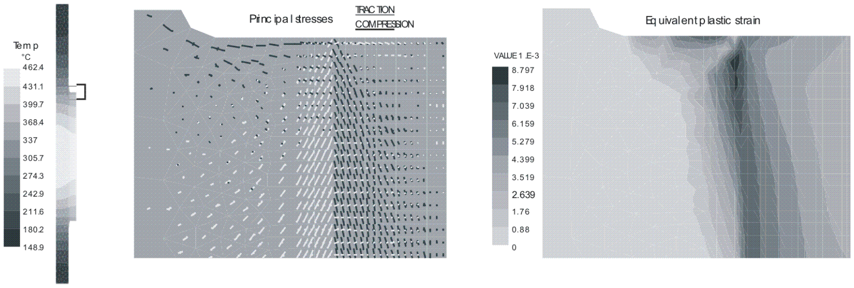

Figure 6.22: Intermediate point (C) of quenching cooling (166 hs)

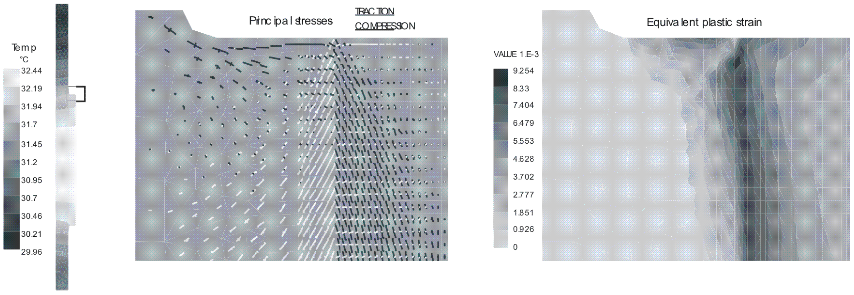

Figure 6.23: End (D) of quenching cooling (332 hs)

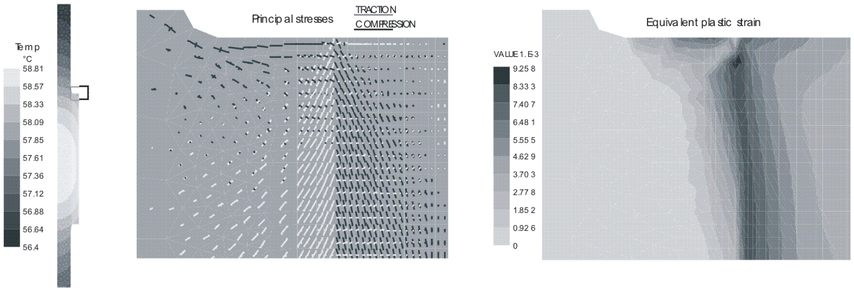

Figure 6.24: End (E) of first tempering (609 hs)

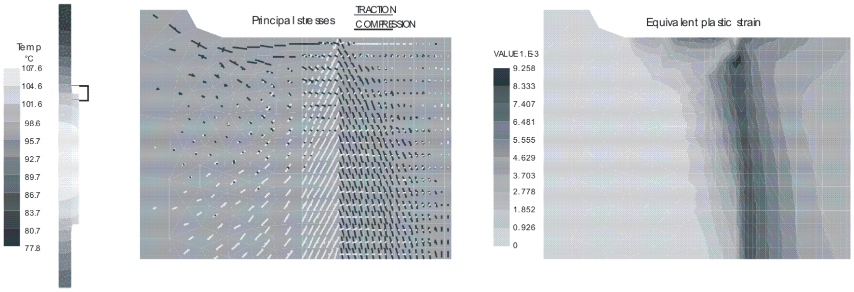

Figure 6.25: End (F) of second tempering cooling (792 hs)

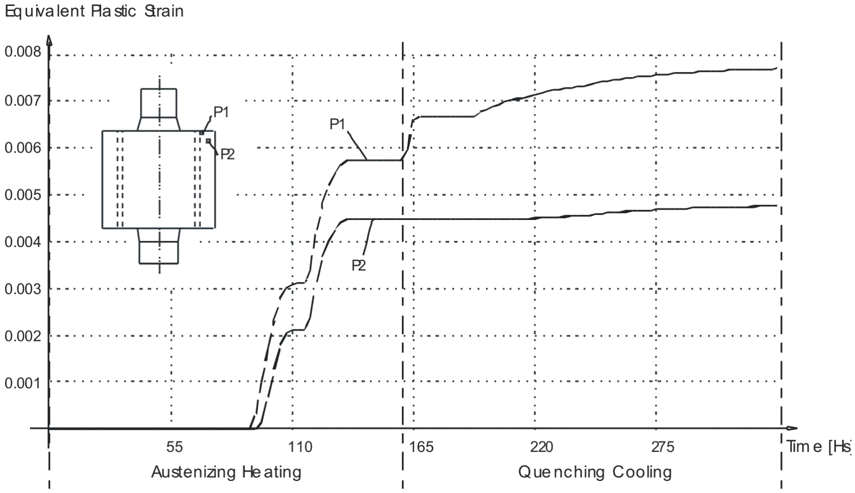

Figure 6.26: Evolution of equivalent plastic strain

Most inelastic deformations occur during the second half of the austenizing heating process and during the quenching cooling, as shown in the plots of equivalent plastic strain. Only a small increment of plastic strains is found during tempering processes (even when this result could be influenced by the lack of information about percentages of retained austenite after quenching cooling and transformations of retained austenite during tempering). The magnitude of inelastic strains found near the interface between shell and intermediate layers (close to 1 percent) are significant, specially taking into account the brittle nature of Hi-Chrome white iron.

These two facts suggest that cracks start in the last stage of austenizing heating, and evolve during the entire process because of the presence of high residual stresses.

Chapter 7

Conclusions

In this thesis finite element models have been developed to analyze the thermal, metallurgical and mechanical phenomena observed in industrial processes which involve the processing of metals at high temperature such as welding and heat treatment of steel. Thermal histories and residual stresses can be predicted and also resulting changes in the microstructure and mechanical properties can be estimated. An important part of this work has been addressed to the validation of the implemented models. The described methods provide a powerful means to optimize process parameters off-line. The welding model can be used to predict and minimize deformations due to changes in the weld sequence during the product development stage. The metallurgical model is expected to give adequate accuracy to predict phase fractions.

Some conclusion, related to the numerical methods presented in the previous chapters of this thesis, can be summarized as follows:

- A finite element model to simulate the 3D transient conduction problem with phase-change has been presented. The use of linear tetrahedral elements facilitates the exact analytical integration of the finite element arrays, and therefore the exact evaluation of the discrete balance equation. Furthermore, the discontinuous integration procedure takes correctly into account, and in a straightforward manner, the discontinuous nature of phase-change phenomena. This feature is not commonly found in alternative models simulating the liquid/solid phase change in welding process

  Thermal results have been correctly validated by means of a non-isothermal phase change problem analytical solution. A mathematical model was implemented to represent the power density distribution of the external heat source. Results obtained in this work using the heat source model are in close agreement with the original results obtained by both, the experimental data of Christensen et al. and the ellipsoidal model proposed by Goldak et al. [GCB84].

- The additivity rule (AR) has been found to be a well adapted scheme to track the microstructure evolution during cooling processes. Microstructure calculations have been coupled with the solution of the heat equation in the three-dimensional space, giving a complete tool for the thermal analysis of industrial processes that involves metals at high temperature. The model has been applied to simulating the Jominy end-quench test, showing satisfactory qualitatively results compared to experiments.

- A standard finite element formulation limited to the solid domain has been adopted for the mechanical analysis, proving to be effective. Regardly the material description, a standard model with isotropic hardening has proven to characterize well the behavior of steel at high temperatures.

  In relation to the methodology described in Chapter 4 (section 4.1) the melting/solidifying treatment of mechanical elements is also an original contribution of this thesis. This methodology is straightforwardly generalized to the study of any metal at high temperatures displaying phase changes from solid to liquid and vice versa.

  The research has also proved to be satisfactory in validating the thermo-mechanical analysis of phase-change problems with the semi-analytical solution of Weiner et al. [WB63] as described in Chapter 4. This is a solid basement to continue software development with ability to simulate accurately complex welding processes.

- The finite element models described in this thesis were applied to solve several examples. Simulations of temperatures and phase fractions involving phase transformation kinetics, latent heat of transformations, etc., were performed. Acceptable results were obtained and comparisons with other author's results have been satisfactory.

  This research effort was successful in determining the final residual stress state of butt-welded joints using finite element simulations. Temperatures and stresses results were obtained.

  Also a simplified model developed to simulate heat treatment of metals was presented. The approximation used to model the thermomechanical variables was found to be useful in this case, for which material parameters are very scattered and difficult to be obtained.

Proposals for future work

Several extensions of the models described in this thesis are possible. For example the filler material modeling can be included, as well as considering an adaptive meshing technique would be valuable to later consider a multipass welding procedure simulation.

Inclution of transformation plasticity in the material model would also be of interest. It is proposed also to perform the Satoh [Sat72] test to validate the implementation.

Further research is needed to include the stress relief process in order to model the pre and post-weld heat treatment.

The current work focuses on thermal history and stresses. However, cracking is another important issue and development of techniques to predict cracking would be of significant industrial interest.

Appendix A

Parallel FEM application

High performance computing makes it possible to reduce analysis times. Frequently a limiting factor is computer memory and then it is possible to obtain a gain running the analysis in a cluster of processors

In this Apendix a parallel non-linear thermal finite element simulation driven in a cluster of PC's using the Python programming language is presented. Previously developed *MPI*, *PETSc* and *ParMETIS* packages are used together to deploy a parallel FEM framework [DPA$^+$05], integrating an important subset of *OOFELIE* toolkit, the sequential C++ code for FEM simulation used in this tesis.

A.1 FEM Simulations

This section describes application of a temperature-based model to simulate an unsteady heat conduction problem in a media undergoing mushy phase change described in Charpter 2. Results of a parallel simulation on a three-dimensional domain with linear tetrahedral finite elements are shown.

Using PETSc and OOFELIE modules, the solidification of an aluminum-copper alloy was simulated in parallel. This alloy has solidus and liquidus temperatures of approximately 540°C and 640°C respectively. Initial temperature was set to 800°C, temperature at the boundary was imposed to 200°C. The domain was a regular cube with 2 meters long edges. Because of symmetry, only one-eighth of the domain was discretized with a million degree of freedom. The mesh was obtained from a regular, structured mesh of hexahedra by splitting each hexahedron in six tetrahedra.

Results are shown in figure A.1 for two representative time steps. Black lines are solidus and liquidus temperature isolines; they clearly indicate the separation of solid, mushy, and liquid phases.

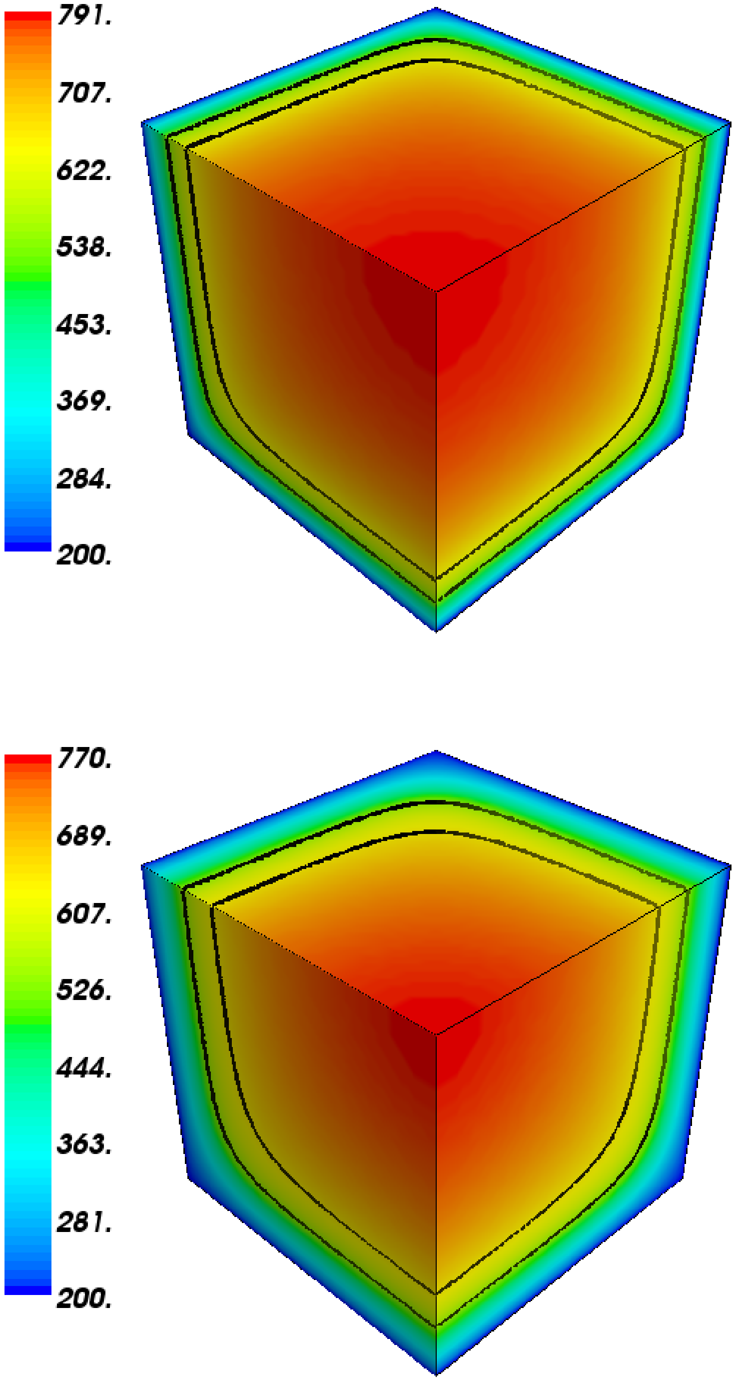

Figure A.1: FEM solution: temperature (°C) for a phase change problem on a 3D domain

Appendix B

Publications arising from this Thesis

A number of publication have arising during the course of this thesis including the following:

1. A. Anca, A. Cardona, and J. Risso. 3d thermo-mechanical simulation of welding processes. In O. Zamonsky G. Buscaglia, E. Dari, editor, *Mecánica Computacional, XIV Congreso de Métodos Numéricos y sus Aplicaciones (Enief 2004)*, volume XXIII, pages 2301–2318, 2004.

2. A. Anca, A. Cardona, V. Colpachi, and J. Risso. Numerical simulation of stress and strain evolution during heat treatment of work rolls. In *15th IAS Rolling Conference and 2nd IAS Conference on Uses of Steel*, pages 641–650, 2004.

3. J. Risso, A. Cardona, and A. Anca. A simplified model for heat treatment simulation. In O. Zamonsky G. Buscaglia, E. Dari, editor, *Mecánica Computacional, XIV Congreso de Métodos Numéricos y sus Aplicaciones (Enief 2004)*, volume XXIII, pages 2443–2460, 2004.

4. A. Anca, A. Cardona, and J. Risso. Welding process simulation with simultaneous computation of material properties. In A. Larreteguy, editor, *Mecánica Computacional, VIII Congreso Argentino de Mecánica Computacional (MECOM 2005)*, volume XXIV, pages 915–932, Buenos Aires, Argentina, 2005.

5. L. Dalcín, R. Paz, A. Anca, M. Storti, and J. D Elía. Parallel fem application development in python. In A. Larreteguy, editor, *Mecánica Computacional ,VIII Congreso Argentino de Mecánica Computacional (MECOM 2005)*, volume XXIV, pages 1823–1838, 2005.

6. V. D. Fachinotti, A. Cardona, and A. A. Anca. Solid-state microstructure evolution in steels. *Mecánica Computacional, VIII Congreso Argentino de Mecánica Computacional (MECOM 2005)*, XXIV:901–914, 2005.

7. J. Risso, A. Cardona, A. Anca, and V. Colpachi. Computation of stress and strain evolution during heat treatment of work rolls. *Journal of Applied Mechanics - Transactions of the ASME*, 73:1045–1053, 2006.

Additional studies I was involved have results in the following works:

1. A. Anca, P. Sanchez, and J. Risso. Modos de falla ductil y bifurcacion material utilizando el modelo constitutivo de gurson. In V. H. Cortínez y D. V. Bambill M. B. Rosales, editor, *Mecánica Computacional, XIII Congreso de Métodos Numéricos y sus Aplicaciones (Enief 2003)*, volume XXII, pages 1867–1877, 2003.
2. P. Sánchez, A. Huespe, A. Anca, and V. Sonzogni. Modos de falla ductil y bifurcacion material utilizando el modelo constitutivo de gurson. In V. Sonzogni M. Storti A. Cardona, N. Nigro, editor, *Mecánica Computacional, XVII Congreso de Métodos Numéricos y sus Aplicaciones (Enief 2006)*, volume XXV, pages 1975–1995, 2006.

Appendix C

Resumen Extendido

C.1 Objetivo

El objetivo general es simular el estado tensional en procesos de producción que involucran fenómenos de cambio de fase y/o transformaciones microestructurales en aceros, a fin de lograr un mejor conocimiento de los fenómenos involucrados y poder optimizar diferentes aspectos relacionados al mismo proceso de producción. Para ello se desarrollan programas de computación especialmente orientados al tratamiento de este tipo de problemas. Los modelos implementados en el mencionado código podrán ser utilizados por ejemplo en simulación de soldadura, tratamientos térmicos o colada continua de aceros.

Los objetivos Particulares se refieren a la simulación numérica de la respuesta termomecánica y los cambios microestructurales que originan variación en propiedades de los materiales en procesos de soldadura por fusión constituyen los objetivos particulares de la presente tesis.

Se ha buscado especialmente validar los modelos utilizados. En particular se utilizaron modelos que describen la física del problema a escala macroscópica. El fin es obtener un código que provea resultados de precisión aceptable en aplicaciones industriales utilizando el método de los elementos finitos.

Como ejemplos de aplicación se estudiarán específicamente las tensiones y microestructura obtenida en los procesos de soldadura de aceros.

C.2 Motivación

El uso del Método de Elementos Finitos (MEF) en el desarrollo de productos está bien consolidado, sin embargo su uso en los procesos de manufactura no es tan común y forma parte del campo de nuevas aplicaciones en mecánica computacional. El mayor incentivo a este desarrollo se debe a la necesidad de la industria de mejorar productividad, la calidad de productos y tener mayor conocimiento de la influencia de diferentes parámetros del proceso sobre el producto.

Los fenómenos que se modelarán, juegan un rol importante en las diversas etapas que entran en juego en la producción de piezas de acero, por ejemplo, soldadura, tratamientos térmicos, fundición y colada entre otras.

La importancia de estas aplicaciones radica en determinar la evolución de tensiones y deformaciones para establecer, por ejemplo, la susceptibilidad a fisuración y prevenir de esta manera fallas durante la fabricación o incluso en servicio. Esta herramienta de simulación podrá ser utilizada además para optimizar algunos aspectos de los procesos de fabricación.

A continuación se citan algunos de los aspectos que pueden ser tratados mediante simulación numérica en pos de optimizar o estudiar los métodos de soldadura.

- Distorsión debida a una mala elección de la secuencia de soldado.
- Optimización de dispositivos de fijación. La elección del modo de sujetar las piezas a unir tiene una marcada influencia en las tensiones residuales y distorsión final de la pieza.
- El tiempo que una pieza debe permanecer en el dispositivo de sujeción puede ser minimizado teniendo en cuenta las distorsiones admisibles de la pieza.
- Los parámetros de los dispositivos soldadores pueden ser ajustados y evaluados a priori, por ejemplo robots, forma del impulso de corriente o casos similares.
- Pueden llevarse a cabo estimaciones tanto de la microestructura resultante, como de la dureza final a fines determinar el post-tratamiento térmico más adecuado.
- Los programas de simulación podrían posteriormente acoplarse con equipos de producción.

C.3 El proceso de soldadura por fusión

Las técnicas de soldadura constituyen uno de los métodos más importantes, y más utilizados en la industria para unión entre piezas. Cualquier información acerca de la forma, dimensiones y tensiones residuales de una pieza soldada es de especial interés para mejorar la calidad, evitar y/o disminuir fallas durante el proceso de manufactura o durante la vida en servicio de la pieza.

La soldadura por fusión es un proceso de unión, en el cual las partes metálicas son calentadas localmente hasta superar el punto de fusión, obteniéndose de esta manera una coalescencia localizada de ambas piezas. Los distintos tipos de soldaduras por fusión se diferencian entre sí por el tipo de fuente de calor que se utiliza para lograr la fusión de los metales. Algunos Ejemplos de fuentes externas de calor son arco eléctrico, laser, haz de electrones. Durante el proceso de soldadura es posible realizar el agregado de un material de aporte.

La resolución del problema de soldadura involucra varias ramas de la física, y requiere del acoplamiento de diferentes modelos que intentan describir el comportamiento fenomenológico de un sistema. Muchos de estos modelos han sido implementados numéricamente y están siendo utilizados en forma eficiente para resolver los problemas en forma individual.

En soldadura por arco, la energía necesaria para la fusión proviene de la liberación de calor por efecto Joule. El metal se encuentra inmerso en un campo electromagnético y la descarga eléctrica genera un arco de plasma entre la punta del electrodo y la pieza a soldar, el cual produce la energía necesaria para fundir el metal base y el de aporte, formándose lo que se conoce como la pileta líquida. La temperatura de la superficie de la pieza es de 1700 K a 2500 K, dependiendo del material. En la pileta liquida tienen lugar efectos convectivos que tienen influencia en el transporte de calor hacia el metal base aun no fundido y al ambiente. Finalmente al suprimir la fuente de calor, el metal solidifica. Los cambios de temperatura durante el proceso producen en la aleación transformaciones en estado sólido. Estas transformaciones microestructurales provocan cambios sensibles en las propiedades materiales durante la evolución del proceso. Los calentamientos y enfriamientos localizados inducen cambios volumétricos. Las deformaciones térmicas que ocurren en las inmediaciones del cordón de soldadura son de índole elastoplásticas. Las tensiones que resultan de estas deformaciones reaccionan produciendo tensiones internas causando las distorsiones típicas en soldadura. Las distorsiones o deformaciones residuales introducen inconvenientes para el ensamblado de estructuras soldadas y reducen su calidad. La forma de la pieza distorsionada y sus dimensiones comprometen en ciertas aplicaciones la utilidad de la pieza o estructura.

Lo mencionado remarca la importancia que tiene, en las etapas de diseño y fabricación, contar con herramientas para modelar el desarrollo de tensiones y deformaciones. Otro aspecto importante a considerar es la estimación de la fiabilidad de la pieza y el desarrollo de métodos adecuados para mejorar la precisión dimensional de las piezas o estructuras soldadas.

Actualmente la simulación de soldadura es utilizada en una amplia área de aplicaciones industriales, aeroespacial, nuclear y astilleros entre otras. Las simulaciones se realizan para obtener el estado de tensiones residuales y las deformaciones o distorsiones que se generan durante el proceso. Otros aspectos de interés en simulación de soldadura es la determinación y caracterización de los parámetros de soldadura, la evolución temporal de la micro-estructura, la temperatura y la deformación, aspectos que son de utilidad para predecir el comportamiento durante el proceso y en servicio de las piezas unidas.

C.4 Estado del arte

El problema de las tensiones residuales y deformaciones en soldadura es mencionado en un trabajo de Slavianov en 1892, en donde habla de lo perjudicial de las tensiones que se generan durante el soldado. Este problema aún persiste y sigue siendo materia de estudio de muchos investigadores.

La simulación de los procesos de soldadura ha avanzado en las tres últimas décadas desde los análisis llevados a cabo en laboratorios experimentales a aplicaciones computacionales que incluyen modelos complejos que describen el proceso y pueden ser utilizados en aplicaciones industriales. Desde los comienzos de los 70s se encuentran publicaciones utilizando el MEF para simular el problema mecánico en soldadura. Marcal [Mar74], Karlsson [Kar86, Kar93], Goldak et al., [GOG$^+$92], Smith [Smi92], and Radaj [Rad88] son referentes en simulaciones hasta los 90s. Algunos de los códigos escritos en la materia se pueden encontrar descriptos en Dexter [Dex91], Chandra [Cha85] and Ravichandran [RRGK97]. También se encuentran capítulos referidos a la simulación de soldadura utilizando MEF en Karlsson [Kar97].

A continuación se hace una reseña del estado del arte en modelización de soldadura, puntualizando las simplificaciones asumidas en artículos más recientes. Así, se encuentran modelos termomecánicos 2D en los trabajos de Song et al [SPNM03] sobre soldadura de juntas, de Branza et al [BDF$^+$04] sobre soldadura tipo TIG para reparación de piezas, de Cho et al [CZKK04] en soldadura por láser, de Hyde et al [HBSS06] para soldadura TIG a tope, de Hou et al[HKW$^+$06] para soldadura de resistencia por puntos, de Deng y Murakawa [DM06b] para soldadura de múltiples pasadas, etc. La motivación (no siempre reconocida) de dicha simplificación es el alto costo computacional de los modelos 3D. Duranton et al [DDR$^+$04] y Gery et al [GLM05] ponen de manifiesto las deficiencias del enfoque 2D en procesos de soldadura de cordones longitudinales al despreciarse el flujo de calor en la dirección de la soldadura. En el aspecto mecánico, el material soldado es modelado como elasto-plástico, independiemnte de la tasa de deformación, ya sea sin endurecimiento [SPNM03, AS05, HKW$^+$06, Moc06, MCGC06], con endurecimiento isotrópico [BDF$^+$04, DDR$^+$04, FPTB06, HBSS06], o cinemático [DM06a, DM06b, MDPM06], o como elasto-viscoplástico [NRLD06, HR06]. Alberg y Berglund [AB03] comparan modelos plásticos y viscoplásticos aplicados en condiciones de soldadura, aceptando el uso del modelo plástico, más simple, en las etapas iniciales del estudio. Sin embargo, no puede obviarse que a altas temperaturas, los efectos viscosos comienzan a tener un efecto notable en el comportamiento de los metales [FC03]. Asimismo, la soldadura en general involucra ciclos de calentamiento-enfriamiento cuyo efecto sobre el comportamiento mecánico del material es representado sólo si se tiene en cuenta endurecimiento cinemático. Por lo tanto, una vez más encontramos la justificación del uso de los modelos más simples como el elasto-plástico sin endurecimiento o sólo con endurecimiento isotrópico (a la sazón, los más utilizados) en una mera reducción de costo computacional. En cuanto al estudio de los cambios microestructurales durante la soldadura, el modelo termomecánico 2D de Deng y Murakawa [DM06b] es capaz de reproducir únicamente la transformación austenita -> martensítica en aceros, que se produce para tasas muy altas de enfriamiento, obviando las transformaciones ferrítica, perlítica y bainítica que se observan en la zona afectada a tasas inferiores. Modelos termo-mecánico-metalúrgico más sofisticados fueron propuestos por Alberg y Berglund [AB03] en 2D, y Ferro et al [FPTB06] en 3D, teniendo en cuenta todas las transformaciones mencionadas. Cabe destacar que en todos los casos, se considera la influencia de la microestructura sobre propiedades mecánicas (tensión de fluencia, dilatación térmica), pero se desprecia la influencia sobre propiedades térmicas como la conductividad, que varía considerablemente con los cambios microestructurales (como se observa en [MLA$^+$02]). Muy pocos modelos aplicados a soldadura tienen en cuenta la dinámica del material fundido. Che et al [CCT04] centran su interés en la determinación de la forma del cordón soldado. Wang et al [WSLT05], y DebRoy y colaboradores [DD06, HNFD06, RED06] modelan la convección en la pileta líquida y su efecto sobre la transferencia de calor. Aunque usualmente ese efecto es aproximado en el análisis térmico aumentando ad hoc la conductividad, se considera importante su inclusión y, si bien escapa a los objetivos inmediatos de este proyecto, será objeto de estudios posteriores. Los modelos 2D de Fan y Kovacevic [FK04] y Lu et al [LTYY06] incluyen como sofisticación adicional los efectos electromagnéticos, aunque se restringen al sistema arco de soldadura-metal fundido. En todos los modelos anteriores, la única interacción considerada entre los análisis térmico y mecánico es la influencia de la temperatura en las propiedades mecánicas, a pesar de observarse en algunos casos una distorsión importante de la pieza soldada, que modifica el flujo de calor por contacto con la mesa de soldadura.

C.5 Sumario de la Tesis

A continuación se expone el lineamiento seguido en la Tesis considerando el contenido de cada uno de los capítulos. El desarrollo de los contenidos y los resultados de los correspondientes capítulos estará conformado en parte por los siguientes trabajos ya publicados [RCAC06, FCA05, ACR05, DPA+05, RCA04, ACR04].

C.5.1 Modelo Térmico

Para obtener el campo de temperaturas durante la soldadura es necesario implementar numéricamente un modelo no estacionario y no lineal de transferencia de calor. El problema presenta, además de las no linealidades debidas a las variaciones de las propiedades térmicas con la temperatura, no linealidades debido al problema de cambio de fase líquido/sólido. En el caso de las aleaciones metálicas, la transformación es no isotérmica y se produce en un rango de temperaturas que se conoce como zona pastosa o mushy.

Modelo de fusión/solidificación tridimensionales no isotérmicos en metales

Este tipo de problema presenta discontinuidades debido a la liberación o absorción de calor latente durante el cambio de fase. Se requiere de elementos finitos especiales para tratar con dichas discontinuidades, a tal fin se han implementado elementos finitos tetraédricos en donde las discontinuidades son tratadas bajo el método de integración discontinua. Los resultados numéricos obtenidos fueron validados contra una solución analítica; de esta forma se verificó que la formulación propuesta ha sido correctamente implementada.

Modelo de fuente móvil de calor

El calor externo aportado puede provenir de distintos modos, a través de un arco eléctrico o el aportado por la energía laser o la de un haz de electrones. La distribución, penetración y la movilidad de estas fuentes es tenida en cuenta ya sea modelando el fenómeno, o mediante modelos matemáticos adecuados que sean capaces de representar de forma acertada la distribución de la densidad de potencia disipada en las piezas a unir. Existen varios modelos propuestos por diferentes autores desde los años 30 (Rosenthal, Myers, Pavelic, Paley y Westbay); finalmente el más utilizado es el propuesto por Goldak et al. [GCB84] basado en una distribución espacial gaussiana de la densidad de potencia y que a la vez permite ser ajustado para los distintos tipos de fuentes de calor utilizadas en soldadura por fusión. Se ha implementado y validado el modelo utilizando los resultados experimentales publicados en [GCB84].

C.5.2 Modelo Metalúrgico

Las propiedades termo-físicas de las aleaciones metálicas dependen en gran medida de las distintas configuraciones alotrópicas que adopte la estructura cristalina y su composición química. Estas propiedades dependen también de la historia de las transformaciones. La composición química del material, el tamaño de grano y la velocidad de enfriamiento, determinan la cinética y el tipo de estructura final de la transformación: formación de ferrita (fase α), perlita (fase $\gamma + F e3C$), bainita ó martensita. Cada una de estas fases posee características y propiedades bien marcadas. De las fracciones da cada una de estas fases presentes se podrá caracterizar microscópicamente a la aleación durante su transformación. La variable que más influencia tiene en la cinética de la transformación es la temperatura y su variación temporal. El campo de temperaturas depende de las propiedades termo-físicas (entre otras la conductividad térmica, el calor específico y el calor latente de transformación), a su vez las propiedades termo-físicas dependen de la temperatura y de su velocidad de cambio. Así pues resulta en un modelo acoplado. Resuelto ambos, permitirá establecer del campo de temperaturas en el tiempo y la distribución final de fases o microestructura. Conocida la fracción de cada fase, se podrá estimar, utilizando modelos de la metalurgia física, las propiedades mecánicas la aleación [Pic78].

El diagrama de transformación isotérmico (TTT) o el diagrama de enfriamiento continuo (CCT), proveen información para determinar la microestructura del material, y de esta manera obtener las fracciones de cada componente (austenita, perlita, martensita, etc.) cuando la temperatura del material evoluciona en el tiempo. Algunos de los modelos clásicos referenciados en la bibliografía son: Johnson amd Mehl (1939), regla de aditividad (Scheil, 1935; Avrami, 1940; Cahn, 1956); modelo de Koistinen and Marburger (1959), modelo de Leblond y Devaux (1984). Buena parte de las estrategias utilizadas están basadas en la ecuación de Kolmogorov-Johnson-Mehl-Avrami (KJMA), que describe la cinética de transformación. El presentado en esta tesis, modela el enfriamiento de aceros desde la temperatura de equilibrio Ae3 hasta la temperatura ambiente, y se limita a aquellos materiales cuya cinética de transformación ha sido previamente ajustada. El Modelo Termo-Metalúrgico describe la evolución de la temperatura, y la descomposición de la austenita en ferrita, perlita, bainita ó martensita, según sea la transformación. No se modela redisolución de fases causadas por un recalentamiento.

En el primer lugar se propuso un modelo simplificado [RCAC06, ACCR04] para la representación de las variaciones de las propiedades termomecánicas de materiales que presentan un cambio significativo en su estructura cristalina durante su enfriamiento. Utilizando los diagramas de transformación isotérmico (TTT) y de enfriamiento continuo (CTT) del material, se crean tablas con las variaciones de las propiedades como función de la temperatura y del tiempo, variables que pueden ser manejadas en la mayoría de los códigos no lineales de elementos finitos. Como ejemplo de aplicación el procedimiento descripto fue utilizado para simular al tratamiento térmico de un rolo de laminación para determinar la evolución de tensiones y deformaciones plásticas en el mismo. Este tipo de análisis permitirá evaluar la susceptibilidad a fisuración para distintas alternativas tanto de diseño como de parámetros de proceso.

Seguidamente se desarrolló un segundo modelo [FCA05] que describe las transformaciones utilizando el concepto de variables de estado, en el cual permite determinar las fracciones de cada componente (austenita, perlita, martensita, etc.) cuando la temperatura del material sigue una evolución temporal. Conocidas las fracciones de cada componerte, se determina el valor de las propiedades termomecánicas utilizando la teoría lineal de mezcla. Luego de la codificación, esta formulación ha sido utilizada para la predicción de propiedades en procesos de soldadura de aceros.

C.5.3 Modelo Mecánico

La determinación del estado de tensiones y deformaciones se efectúa realizando un análisis mecánico. Estas tensiones son producidas, en ausencia de cargas externas, a causa de los cambios de volumen debido a las transformaciones microestructurales y dilatación térmica. Si estos cambios volumétricos son de magnitud suficiente pueden originar deformaciones plásticas y consecuentemente originar tensiones residuales y distorsiones permanentes. En el análisis se utilizará hipótesis de pequeñas deformaciones y un modelo de plasticidad de von Mises con endurecimiento isotrópico. Este último está ampliamente aceptado como modelo constitutivo en aplicaciones sobre metales a alta temperatura. Los fenómenos viscoplásticos no son considerados debido al relativamente corto lapso de tiempo que el material se encuentra a elevada temperatura [Lin01, AB03].

Problema mecánico en metales que involucran fusión y solidificación. El método de los Elementos Finitos (MEF) es usado con resultados satisfactorios para el análisis de tensiones producidas por efectos térmicos a temperaturas cercanas a las de solidificación utilizando modelos constitutivos estándares. Sin embargo cuando se presentan fenómenos de fusión y solidificación en el problema que se intenta analizar, se deben introducir cambios respecto de las formulaciones utilizadas habitualmente. Estos cambios están relacionados con la configuración de referencia adoptada para hacer la medición de deformaciones, deformaciones que luego son empleadas para el cálculo de tensiones. Si por ejemplo el material supera la temperatura de mínima resistencia [NUM95b] (Zero Strength Temperature, ZST) se considera que no posee capacidad para soportar carga, y por lo tanto no es considerado en el cálculo de fuerzas internas; en cambio, cuando la temperatura baja de ZST, el material comienza a comportarse como un sólido deformable capaz de soportar cargas externas. Es a partir de esta configuración, en la cual las tensiones y variables internas son nulas (material virgen), que deben ser medidas las deformaciones. Esta es llamada "configuración natural", para diferenciarla de la configuración actual y de la configuración inicial. La configuración inicial es la que coincide con la malla de elementos finitos y es la que comúnmente se utiliza para la el cálculo de deformaciones. La estrategia utilizada para tener en cuenta lo anteriormente descrito consiste en hacer un cálculo único de la deformación en la configuración natural para cada punto material y en los sucesivos cálculos de tensión restar esta deformación a la deformación respecto de la deformación inicial. De esta manera las tensiones calculadas se corresponden con la deformación que realmente se produce en los primeros instantes luego que el material comienza a comportarse como un sólido resistente.

Otra particularidad que tiene el problema mecánico en los primeros estadios de solidificación, es que debido a los bajos valores de la tensión de fluencia, las deformaciones son predominantemente pláticas, lo cual trae problemas numéricos debido a la incompresibilidad-plástica. Para evitar el comportamiento oscilante de las tensiones se utilizan formulaciones mixtas estabilizadas en las cuales se resuelve el problema utilizando los desplazamientos y presiones como variables del problema.

Validación del problema termo-mecánico. La formulación desarrollada [ACR05] ha sido validada exitosamente contra la solución semi-analítica de Weiner y Boley [WB63]. Esta misma estrategia de validación es utilizada por otros autores en el estudio de colada continua [Tho95]. Weiner et. al., asumiendo hipótesis ideales, resolvieron analíticamente el problema termo-mecánico obteniendo la distribución de tensiones en la cáscara sólida durante el proceso de solidificación de metales. Este problema se usó como referencia para determinar la exactitud de los cálculos realizados.

Nuevos algoritmos para la solución del problema mecánico. Se implementaron algoritmos especiales para el tratamiento de los elementos mecánicos durante el cambio de fase líquido/sólido y sólido/líquido. Mientras la temperatura se encuentra por encima de la temperatura de mínima resistencia (ZST) los elementos no son incluidos en el sistema de ecuaciones que resuelven las incógnitas del problema mecánico. Esta metodología incorpora una ventaja en comparación a otras técnicas encontradas en la literatura, como ser el asignarle una rigidez muy baja a los elementos que se encuentran en estado liquido/pastoso, lo cual trae aparejados problemas de mal condicionamiento del sistema a resolver.

C.5.4 Acoplamiento

El análisis térmico se encuentra fuertemente acoplado con el modelo que describe las transformaciones microestructurales. La liberación de calor latente y las propiedades térmicas dependen de la microestructura y la temperatura; esta última, es a su vez la variable que gobierna las transformaciones microestructurales. La energía disipada por deformación mecánica y la influencia de la deformación en las transformaciones tienen efectos despreciables. Con lo cual el modelo térmico y el modelo metalúrgico quedan desacoplados del modelo mecánico.

Acoplamiento térmico metalúrgico. Las propiedades materiales en la ecuación de balance de energía son dependientes de la temperatura y a su vez dependientes de la fracción microestructural presente. Esta última depende de la velocidad de enfriamiento que sigue cada punto material. También se debe tener en cuenta la liberación de calor latente debido al cambio de fase líquido / sólido como así también la del cambio de fase producido en estado sólido. Los efectos antes mencionados hacen que el problema térmico se encuentre fuertemente acoplado con el problema metalúrgico. La estrategia adoptada para resolverlos es similar a la utilizada en el cálculo de tensiones en un problema mecánico. Las ecuaciones de evolución de las variables internas forman un sistema de ecuaciones diferenciales ordinarias de tipo dinámico, dependientes solamente del tiempo y no del espacio. Por lo cual son resueltas a nivel elemental para cada punto espacial donde se requiere conocer el valor de una propiedad determinada.

Integración temporal y resolución del acoplamiento termo-metalúrgico-mecánico. Los conocimientos, modelos y técnicas de simulación descriptas en el presente trabajo se acoplan para simular las uniones soldadas entre componentes metálicos. La integración temporal del sistema de ecuaciones diferenciales ordinarias que resulta luego de la discretización espacial se resuelve utilizando diferencias finitas hacia atrás o backward-Euler. El sistema no lineal de ecuaciones algebraico resultante es resuelto luego por el método de newton. Se utiliza una técnica de resolución escalonada o staggered, que consiste en resolver para cada paso de tiempo el problema térmico-metalúrgico y luego con el campo de temperaturas son evaluadas las propiedades mecánicas para resolver el problema mecánico.

C.5.5 Resultados

Se presentan resultados de simulación de soldadura por fusión a tope y de un modelo simplificado de tratamiento térmico aplicado a rolos de laminación.

Bibliography

[AB03] H. Alberg and D. Berglund. Comparison of plastic, viscoplastic, and creep models when modelling welding and stress relief heat treatment. *Comput. Methods Appl. Mech. Engrg.*, 192:5189–5208, 2003.

[ACCR04] A. Anca, A. Cardona, V. Colpachi, and J. Risso. Numerical simulation of stress and strain evolution during heat treatment of work rolls. In *15th IAS Rolling Conference and 2nd IAS Conference on Uses of Steel*, pages 641–650, 2004.

[ACR04] A. Anca, A. Cardona, and J. Risso. 3d thermo-mechanical simulation of welding processes. In G. Buscaglia, E. Dari, and O. Zamonsky, editors, *Mecánica Computacional, XIV Congreso de Métodos Numéricos y sus Aplicaciones (Enief 2004)*, volume XXIII, pages 2301–2318, 2004.

[ACR05] A. Anca, A. Cardona, and J. Risso. Welding process simulation with simultaneous computation of material properties. In A. Larreteguy, editor, *Mecánica Computacional, VIII Congreso Argentino de Mecánica Computacional (MECOM 2005)*, volume XXIV, pages 915–932, 2005.

[Alb03] H. Alberg. Material modeling for simulation of heat treatment. *Licentiate Thesis, Lulea University of Technology, Sweden*, 2003.

[AM98] C. Aliaga and E. Massoni. 3d numerical simulation of thermo-elasto-visco-plastic behavior using a stabilized mixed f.e. formulation: Application to heat treatment. *Proc.NumiformŠ98, Huétink and Baaijens, eds., Balkema, Rotterdam, The Netherlands*, pages 263–269, 1998.

[Ame77] American Society for Metals. *Atlas of isothermal transformation and cooling transformation diagrams*, 1977.

[AS05] M. Abid and M. Siddique. Numerical simulation to study the effect of tack welds and root gap on welding deformations and residual stresses of a pipe-flange joint. *International Journal of Pressure Vessels and Piping*, 82:860–871, 2005.

[Avr39] M. Avrami. Kinetics of phase change i. general theory. *J. Chem. Phys.*, 7:1103–1112, 1939.

[Avr40] M. Avrami. Kinetics of phase change. ii transformation-time relations for random distribution of nuclei. *J. Chem. Phys*, 8:212, 1940.

[BDF$^+$04] T. Branza, A. Duchosal, G. Fras, F. Deschaux-Beaume, and P. Lours. Experimental and numerical investigation of the weld repair of superplastic forming dies. *Journal of Materials Processing Technology*, 155:1673–1680, 2004.

[Bel75] P.E Belyakova. Thermophysical properties of wear-resisting cast irons. *Metallovediene I Termicheskaya Obrabotka Metallov.*, 12:45–48, 1975.

[Ber01] D Berglund. Simulation of welding and stress relief heat treatment in development of aerospace components. *Licentiate Thesis, Lulea University of Technology, Sweden*, 2001.

[Bet04] W. Betts. Personal communication. 2004.

[BGB98] J.M. Bergheau, G.Mangialenti, and F. Boitout. Contribution of numerical simulation to the analysis of heat treatment and surface hardening processes. *Proc.of 18th ASM Heat Treating Conference and Exposition, Wallis and Walton, eds., Rosemont, IL*, page 152, 1998.

[Boy77] H. Boyer. Atlas of isothermal transformations and cooling transformations diagrams. *ASM International, Materials Park, OH*, pages II–68, 1977.

[BPK$^+$96] D. Bammann, V. Prantil, A. Kumar, T. Lowe, H.-J. Jou, M. Lusk, G. Krauss, B. Dowling, B. Elliott, Jr, G. Ludtka, D. Shick, and D. Nikkel. Development of a carburizing and quenching simulation tool: A material model for carburizing steels undergoing phase transformations. In G. Totten, M. Howes, S. Sjöstrom, and K. Funatani, editors, *Proceedings of the Second International Conference on Quenching and the Control of Distortion*, pages 367–375, Cleveland, Ohio, November 1996.

[BPM$^+$95] S. Benzley, E. Perry, K. Merkely, B. Clark, and G. Sjaardama. A comparison of all hexagonal and all tetrahedral finite element meshes for elastic and elasto-plastic analysis. *Proc. 14th Ann. Int. Meshing Roundtable, Albuquerque, USA*, 1995.

[BS92] S. Brown and H. Song. Finite element simulation of welding of large structures. *ASME Journal of Engineering for Industry*, 114:441–451., 1992.

[CCT04] J. Che, S. L. Ceccio, and G. Tryggvason. Computations of structures formed by the solidification of impinging molten metal drops. *Applied Mathematical Modelling*, 28:127–144, 2004.

[CDG65] N. Christensen, V. de L. Davies, and K. Gjermundsen. Distribution of temperatures in arc welding. *British Welding Journal*, 12:54–75, 1965.

[Cha85] U. Chandra. Determination of residual stresses due to girth-butt welds in pipes. *ASME J. Pressure Vessel Technology*, 107:178–184, 1985.

[CK92] A. Cifuentes and A. Kalbag. A performance study of tetrahedral and hexahedral elements in 3-d finite element structural analysis. *Fin. Elem. Anal*, 12:313–318, 1992.

[CKG94] A. Cardona, I. Klapka, and M. Gerardin. Design of a new finite element programming environment. *Engineering Computation*, 11(4):365–381, aug 1994.

[CT04] P. Chang and T. Teng. Numerical and experimental investigations on the residual stresses of the butt-welded joints. *Computational Materials Science*, 29(4):511–522, 2004.

[CZKK04] C. Cho, G. Zhao, S. Y. Kwak, and C. B. Kim. Computational mechanics of laser cladding process. *Journal of Materials Processing Technology*, pages 153–154:494–500, 2004.

[DD06] A. De and T. DebRoy. Improving reliability of heat and fluid flow calculation during conduction mode laser spot welding by multivariable optimisation. *Science and Technology of Welding and Joining*, pages 11(2):143–153, 2006.

[DDR$^+$04] P. Duranton, J. Devaux, V. Robin, P. Gilles, and J. M. Bergheau. 3d modelling of multipass welding of a 316l stainless steel pipe. *Journal of Materials Processing Technology*, pages 153–154:457–463, 2004.

[Dex91] R. Dexter. Residual stress analysis in reactor pressure vessel attachments - review of available software. *Electric Power Research Institute, EPRI NP-7469s*, 1991.

[DM06a] D. Deng and H. Murakawa. Numerical simulation of temperature field and residual stress in multi-pass welds in stainless steel pipe and comparison with experimental measurements. *Computational Materials Science*, pages 37:269–277, 2006.

[DM06b] D. Deng and H. Murakawa. Prediction of welding residual stress in multi-pass butt-welded modified 9Cr 1Mo steel pipe considering phase transformation effects. *Computational Materials Science*, 37:209–219, 2006.

[DPA$^+$05] L. Dalcín, R. Paz, A. Anca, M. Storti, and J. D Elía. Parallel fem application development in python. In A. Larreteguy, editor, *Mecánica Computacional ,VIII Congreso Argentino de Mecánica Computacional (MECOM 2005)*, volume XXIV, pages 1823–1838, 2005.

[Fac08] V. D. Fachinotti. Revisions to the nguyen's semi-analytical solution for the goldak's heat source model. *CIMEC Internal Report*, 2008.

[FC03] V. Fachinotti and A. Cardona. Constitutive models of steel under continuous casting conditions. *Journal of Material Processing Technology*, 135:30–43, 2003.

[FCA05] V. D. Fachinotti, A. Cardona, and A. A. Anca. Solid-state microstructure evolution in steels. *Mecánica Computacional, VIII Congreso Argentino de Mecánica Computacional (MECOM 2005)*, XXIV:901–914, 2005.

[FCH99] V. Fachinotti, A. Cardona, and A. Huespe. A fast convergent and accurate temperature model for phase-change heat conduction. *Int. J. Numer. Meth. Engng.*, 44:1863–1884, 1999.

[FCH01] V. Fachinotti, A. Cardona, and A. Huespe. Numerical simulation of conduction-advection problems with phase change. *Latin Am. Applied Research*, 31:31–36, 2001.

[FK04] H. G. Fan and R. Kovacevic. A unified model of transport phenomena in gas metal arc welding including electrode, arc plasma and molten pool. *J. Phys. D: Appl. Phys.*, 37:2531–2544, 2004.

[FPTB06] P. Ferro, H. Porzner, A. Tiziani, and F. Bonollo. The influence of phase transformations on residual stresses induced by the welding process - 3d and 2d numerical models. *Modelling Simul. Mater. Sci. Eng.*, 14:117–136, 2006.

[FR00] M. Francis and S. Rahman. Probabilistic analysis of weld cracks in center-cracked tension specimens. *Computers and Structures*, 76:483–506, 2000.

[GCB84] J. Goldak, A. Chakravarti, and M. Bibby. A new finite element model for welding heat sources. *Metallurgical Transactions B*, 15:299–305, 1984.

[GD03] R. Gundlach, , and D. Doane. Alloy cast irons. *ASM Metals Handbook Vol.1, ASM International, Materials Park, OH*, pages 85–104, 2003.

[GLM05] D. Gery, H. Long, and P. Maropoulos. Effects of welding speed, energy input and heat source distribution on temperature variations in butt joint welding. *Journal of Materials Processing Technology*, 167:393–401, 2005.

[GOG$^+$92] J. Goldak, A. Oddy, M. Gu, , W. Ma, A. Mashaie, and E. Hughes. Coupling heat transfer, microstructure evolution and thermal stress analysis in weld mechanics. *IUTAM Symposium on the Mechanical Effects of Welding, Springer Verlag*, pages 1–30, 1992.

[HBSS06] T. H. Hyde, A. A. Becker, Y. Song, and W. Sun. Failure estimation of tig butt-welded inco718 sheets at 620žc under creep and plasticity conditions. *Computational Materials Science*, 35:35–41, 2006.

[HKW$^+$06] Z. Hou, I.S. Kim, Y. Wang, C. Li, and C. Chen. Finite element analysis for the mechanical features of resistance spot welding process. *Journal of Materials Processing Technology, DOI:10.1016/j.jmatprotec.2006.03.143 (in press)*, 2006.

[HNFD06] X. He, J. T. Norris, P. W. Fuerschbach, and T. DebRoy. Liquid metal expulsion during laser spot welding of 304 stainless steel. *J. Phys. D: Appl. Phys.*, 39:525–534, 2006.

[Höm96] D. Hömberg. A numerical simulation of the jominy end-quench test. *Acta Materialia*, 44(11):4375–4385, 1996.

[HR06] B. Hu and I. M. Richardson. Mechanism and possible solution for transverse solidification cracking in laser welding of high strength aluminium alloys. *Materials Science and Engineering A*, 429:287–294, 2006.

[Hug87] T. Hughes. *The Finite Element Method. Linear Static and Dynamic Finite Element Analysis.* Prentice-Hall, 1987.

[IW84] T. Inoue and Z.G. Wang. High-temperature behaviour of steels with phase transformation and the simulation of quenching and welding processes. *Proceedings of 4th International Conference on Mechanical Behaviour of Materials*, 283:1015Ũ1021, 1984.

[JB97] S. J. Jones and H. K. D. H. Bhadeshia. Kinetics of the simultaneous decomposition of asutenite into several transfomation products. *Acta mater.*, 45(7):2911–2920, 1997.

[JM39] W. Johnson and R. Mehl. Reaction kinetics in processes of nucleation and growth. *Trans. Amer. Inst. Min. Metall. Eng.*, 135:416–458, 1939.

[Kar86] L. Karlsson. Thermal stresses in welding. *in R.B. Hetnarski (ed.), Thermal Stresses, vol. I, Elsevier Science Publishers*, page 300, 1986.

[Kar93] L. Karlsson. Thermomechanical fnite element models for calculation of residual stresses due to welding. *in Hauk et al. (eds), Residual Stresses, DGMInformationsgesellschaft Verlag*, page 33, 1993.

[Kar97] L. Karlsson. Modeling in welding, hot powder forming, and casting. *ASM International*, 1997.

[KBJ90] R.I Karlsson, B.L., and Josefson. Three-dimensional finite element analysis of temperatures and stresses in a single-pass butt-welded pipe. *ASME Journal of Pressure Vessel Technology*, 112:76–84., 1990.

[KM59] D.P. Koistinen and R. E. Marburger. A general equation prescribing the extent of the austenite-martensite transformation in pure iron-carbon alloys and plain carbon steels. *Acta Metal.*, 7:59–60, 1959.

[KTB78] J. Kirkaldy, B. Thomson, and E. Baganis. Hardenability concepts with applications to steel. *AIME Transactions, J.Kirkaldy and D.Doane, eds., Warrendale, PA*, page 82, 1978.

[LC94] J. Lemaître and J. Chaboche. *Mechanics of Solid Materials.* Cambridge University Press, 1994.

[LDD89] J. B. Leblond, J. Devaux, and J. C. Devaux. Mathematical modelling of transformation plasticity in steels. i: Case of ideal-plastic phases. *Int. J. of Plasticity*, 5:551–572, 1989.

[Leb89] J. B. Leblond. Mathematical modelling of transformation plasticity in steels. ii: Coupling with strain hardening phenomena. *Int. J. of Plasticity*, 5:573–591, 1989.

[Lem59] B. S. Lement. Distortion in tool steels. *American Society for Metals, Ohio*, 1959.

[LGR96] G. Laird, R. Gundlach, and K. Rörig. Heat treatment of high-alloy ar cast irons. *Abrasion Ũ Resistant Cast Iron Handbook, American Foundry Society, Schaumburg, IL, Chap. 3*, 1996.

[Lin01] L.-E. Lindgren. Finite element modeling and simulation of welding. part 2: Improved material modeling. *J. Thermal Stresses*, 24(3):195–231, 2001.

[LJ97] M. Lusk and H.-J. Jou. On the rule of additivity in phase transformations kinetics. *Metallurgical and Materials Transactions A*, 28:287–291, 1997.

[LJR^{+}01] M. T. Lusk, R. Jaramillo, A. Roche, C. Mgbokwere, and S. Deshpande. Microstructural evolution in sprayformed steel: Phase transitions, inelasticity, residual stress and distortion. In R. Srinivasan, S. Semiatin, A. Beaudoin, S. Fox, and Z. Jin, editors, *Microstructural Modeling and Prediction During Thermomechanical Processing*, pages 75–84, Warrendale, PA, 2001. The Minerals, Metals and Materials Society.

[LL99] M. T. Lusk and Y.-K. Lee. A global material model for simulating the transformation kinetics of low alloy steels. In J. Lendvai and T.Reti, editors, *Proceedings of the 7th. International Seminar of IFHT on Heat Treatment and Surface Enginnering of Light Alloys*, pages 273–282, Budapest, September 1999. Hungarian Scientific Society of Mechanical Engineering (GTE).

[LT02] C. Li and B. Thomas. Thermo-mechanical finite element model of shell behavior in the continuous casting of steel. *Proc.6th Asia-Pacific symp.on engineering plasticity and its applications*, 1:827–834, 2002.

[LTYY06] F. Lu, X. Tang, H. Yu, and S. Yao. Numerical simulation on interaction between tig welding arc and weld pool. *Computational Materials Science*, 35:458–465, 2006.

[LWSL03] M. T. Lusk, W. Wang, X. Sun, and Y.-K. Lee. On the role of kinematics in constructing predictive models of austenite decomposition. In E. B. Damm and M. J. Merwin, editors, *Austenite Formation and Decomposition*, pages 311–332, Warrendale, PA, 2003. The Minerals, Metals and Materials Society.

[Lyn75] C. T. Lynch. *CRC Handbook of Materials Science*, volume 2, Metals, Composites and Refractory Materials. CRC Press,Boca Raton, FL, 1975.

[Mar74] P. Marcal. Weld problems, structural mechanics programs. *Charlottesville, University Press*, pages 191–206, 1974.

[MCGC06] P. Mollicone, D. Camilleri, T. G. F. Gray, and T. Comlekci. Simple thermo-elastic-plastic models for welding distortion simulation. *Journal of Materials Processing Technology*, 172:77–86, 2006.

[MDPM06] M. M. Mahapatra, G. L. Datta, B. Pradhan, and N. R. Mandal. Three-dimensional finite element analysis to predict the effects of saw process parameters on temperature distribution and angular distortions in single-pass butt joints with top and bottom reinforcements. *International Journal of Pressure Vessels and Piping, DOI:10.1016/j.ijpvp.2006.07.011 (in press)*, 2006.

[MGOB87] J. McDill, J. Goldak, A. Oddy, and M. Bibby. Isoparametric quadrilaterals and hexahedrons for mesh grading algorithms. *Comm. Appl. Numer. Methods*, 3:155–163, 1987.

[MLA^{+}02] L. Masson, T. Loulou, E. Artioukhine, Rogeon, D. Carron, and J. J. Quemener. A numerical study for the estimation of a convection heat transfer coefficient during a metallurgical "Jominy end-quench" test. *Int. J. Therm. Sci.*, 41:517–527, 2002.

[Moc06] M. Mochizuki. Control of welding residual stress for ensuring integrity against fatigue and stress-corrosion cracking. *Nuclear Engineering and Design, DOI:10.1016/j.nucengdes.2006.05.006 (in press)*, 2006.

[MS79] H. Matthies and G. Strang. The solution of nonlinear finite element equations. *Int. J. Numer. Meth. Engng.*, 14:1613–1626, 1979.

[MTZ93] A. Moitra, B. Thomas, and H. Zhu. Application of a thermo-mechanical finite element model of steel shell behavior in the continuous slab casting mold. *Proc.76th Steelmaking Conf. ISS*, 76:657–667, 1993.

[NMSO04] N. T. Nguyen, Y.-W. Mai, S. Simpson, and A. Ohta. Analytical approximate solution for double ellipsoidal heat source in finite thick plate. *Welding Journal*, pages 82–93, march 2004.

[NOM+99] N. T. Nguyen, A. Ohta, K. Matsuoka, N. Suzuki, and Y. Maeda. Analytical solutions for transient temperature of semi-infinite body subjected to 3-d moving heat sources. *Welding Research Supplement*, pages 265–274, august 1999.

[NRLD06] R. Nandan, G. G. Roy, T. J. Lienert, and T. DebRoy. Numerical modelling of 3d plastic flow and heat transfer during friction stir welding of stainless steel. *Science and Technology of Welding and Joining*, 1:526–537, 2006.

[NUM+95a] T. Nakagawa, T. Umeda, J. Murata, Y. Kamimura, and N. Niwa. Deformation behavior during solification of steels. *ISIJ Int.*, 35(6):723–729, 1995.

[NUM95b] T. Nakagawa, T. Umeda, and T. Murate. Strength and ductility of solidifying shell during casting. *Trans. Iron Steel Inst. Jap.*, 35:723Ű728, 1995.

[OG93] J. M. J. McDill A. S Oddy and J. A. Goldak. Comparing 2-d plane strain and 3-d analyses of residual stresses in welds. *International Trends in Welding Science and Technology, Proceedings of the 3rd International Conference on Trends in Welding Research, ASM International Materials*, pages 105–108., 1993.

[OGM89] A. S. Oddy, J.A Goldak, and J. M. J. McDill. Transformation plasticity and residual stresses in single-pass repair welds. *ASME PVP- Weld Residual Stresses and Plastic Deformation*, 173:13–18, 1989.

[Ope04] Open Engineering. OOFELIE toolkit, 2004. `http://www.open-engineering.com/`.

[OU79] M. Özisik and J. Uzzell. Exact solution for freezing in cylindrical symmetry with extended freezing temperature range. *Journal of Heat Transfer*, 101:331–334, May 1979.

[Pic78] F.B. Pickering. The optimisation of microstructure in steel and their relationship to mechanical properties. *Hardenability Concepts with Apllications to Steels, Ed.: AIME*, 1978.

[Rad88] R. Radaj. Finite element analysis of welding residual stresses. *Proc. of 2nd Int. Conf. on Residual Stresses (ICRS-2)*, page 510, 1988.

[RCA04] J. Risso, A. Cardona, and A. Anca. A simplified model for heat treatment simulation. In G. Buscaglia, E. Dari, and O. Zamonsky, editors, *Mecánica Computacional, XIV Congreso de Métodos Numéricos y sus Aplicaciones (Enief 2004)*, volume XXIII, pages 2443–2460, 2004.

[RCAC06] J. Risso, A. Cardona, A. Anca, and V. Colpachi. Computation of stress and strain evolution during heat treatment of work rolls. *Journal of Applied Mechanics - Transactions of the ASME*, 73:1045–1053, 2006.

[RED06] G. G. Roy, J. W. Elmer, and T. DebRoy. Mathematical modeling of heat transfer, fluid flow, and solidification during linear welding with a pulsed laser beam. *Journal of Applied Physics*, 100:1–5, 2006.

[RF99] T. Réti and I. Felde. A non-linear extension of the additivity rule. *Computational Materials Science*, 15:466–482, 1999.

[RFF01] T. Reti, Z. Fried, and I. Felde. Computer simulation of steel quenching process using a multi-phase transformation model. *Computational Materials Science*, 22:261–278, 2001.

[RRGK97] G. Ravichandran, V. P. Raghupathy, N. Ganesan, and R. Krishnakumar. Prediction of axis shift distortion during circumferential welding of thin pipes using the ćnite element method. *Welding Journal*, pages 39s–55, 1997.

[S.A04] Samtech S.A. Samcef / mecano v10.1 user manual. *Liege, Belgium*, 2004.

[Sat72] K. Satoh. Transient thermal stresses of weld heat-affected zone by both-ends-fixed bar analogy. *Trans. Jpn. Weld. Soc.*, 3:125–134, 1972.

[Sch35] E. Scheil. Finite element modelling and simulation of welding. part 3: Efficiency and integration. *Archiv für Eisenhüttenwessen*, 8:565–567, 1935.

[SGV98] G. Sanchez Sarmiento, A. Gastón, and J. Vega. Inverse heat conduction coupled with phase transformations problems in heat treating processes. *Computational Mechanics Ũ New trends and applications, Oñate and Idelsohn, eds., CIMNE, Barcelona, Spain, CD-Book Part VI, section 1, paper 16*, 1998.

[SH98] J. Simo and T. Hughes. *Computational Inelasticity.* Springer-Verlag, New York, 1998.

[Smi92] S. D. Smith. A review of weld modelling for the prediction of residual stresses and distortions due to fusion welding. *Proc. of the ćfth Int. Conf. on Computer Technology in Welding*, 4, 1992.

[SPNM03] J. Song, J. Peters, A. Noor, and P. Michaleris. Sensitivity analysis of the thermomechanical response of welded joints. *International Journal of Solids and Structures*, 40:4167–4180, 2003.

[Ste95] D. Stefanescue. Physical properties of cast iron. *Iron Castings Engineering Handbook, Blair et al., eds., ASM International, Materials Park, OH*, Chap. 8:223–244, 1995.

[SZGMS03] N. Saunders, X. Li Z. Guo, A. P. Miodownik, and J. P. Schillé. Using jmatpro to model materials properties and behavior. *JOM*, 55(12):60–65, 2003.

[Tal02] L. Taleb. Thermal, metallurgical and mechanical interactions in the 16mnd5 steel. *Proc. of 1er Colloque interdisciplinaire sur les materiaux Ũ Materiaux 2002, Tours, France*, 2002.

[Tho95] B.G. Thomas. Issues in thermal-mechanical modeling of casting processes. *ISIJ Int.*, 35(6):737–743, 1995.

[TM91] P. Tekriwal and J. Mazumder. Transient and residual thermal strain-stress analysis of gmaw. *ASME J. of Engineering Materials and Technology*, 113(336-343), 1991.

[TT83] Hughes T. and Belytschko T.(eds.). *Computational Methods for Transient Analysis.* NORTH-HOLLAND, 1983.

[VJC$^+$99] Y. Vincent, JF Jullien, N. Cavallo, L. Taleb, V. Cano, S. Taheri, and Gilles. On the validation of the models related to the prevision of the haz behaviour. *ASME PVPFracture, Fatigue and Weld Residual Stress*, 393:193–200., 1999.

[Wan01] D. Wang. Thermophysical property data. *Auburn Solidification Design Center* `http://metalcasting.auburn.edu/data/data.html`, 2001.

[WB63] J.H. Weiner and B.A. Boley. Elasto-plastic thermal stresses in a solidifying body. *J. Mech. Phys. Solids*, 11:145–154, 1963.

[WKYO98] Y.M Won, K.H. Kim, T. Yeo, and K.H. Oh. Effect of cooling rate on ZST, LIT and ZDT of carbon steels near melting point. *ISIJ Int.*, 38(10):1093–1099, 1998.

[WSLT05] W. Wang, Y. Shi, Y. Lei, and Z. Tian. Fem simulation on microstructure of dc flash butt welding for an ultra-fine grain steel. *Journal of Materials Processing Technology*, 161:497–503, 2005.

[YJMX04] Li Yajiang, Wang Juan, Chen Maoai, and Shen Xiaoqin. Finite element analysis of residual stress in the welded zone of a high strength steel. *Bull. Mater. Sci.*, 27(2):127–132, 2004.

[YNO95] A. Yamanaka, K. Nakajima, and K. Okamura. Critical strain for internal crack formation in continuous casting. *Ironmaking and Steelmaking*, 22(6):508–512, 1995.

[Yu77] H. J. Yu. *Berechnung von Abkühlungs-, Umwandlungs-, Schweiss-, sowie Verformung-seigenspannungen mit Hilfe der Methode der finiten Elemente.* PhD thesis, Universität Karlsruhe, Germany, 1977.

[ZT00] O. Zienkiewicz and R. Taylor. *The Finite Element Method*, volume 1: The Basis. Butterworth-Heinemann, 5th. edition, 2000.

Doctorado en Ingeniería
mención mecánica computacional

Título de la obra:

COMPUTER SIMULATION OF STEEL THERMOMECHANICAL PROCESSES AT HIGH TEMPERATURES

Autor: Ing. Andrés A. Anca

Lugar: Santa Fe, Argentina

Palabras Claves: Soldadura, Tratamiento Térmico, Tensiones Térmicas, Simulación Numérica.

Keywords: Welding, Heat Treatment, Thermal Stresses, Numerical Simulation.